TEM STUDIES OF EPITAXIAL IRON OXIDE THIN FILMS

TEM STUDIES OF EPITAXIAL IRON OXIDE THIN FILMS

By

JESÚS ALFREDO CARRANCO-RODRÍGUEZ, B. ENG.

A Thesis Submitted to the School of Graduate Studies in Partial Fulfillment of the Requirements for the Degree of Master of Applied Science

McMaster University MASTER OF APPLIED SICENCE (2018) Hamilton, Ontario, (Materials Science and Engineering).

TITLE: TEM Studies of Epitaxial Iron Oxide Thin Films.

AUTHOR: Jesús Alfredo Carranco-Rodríguez, B. Eng. (Universidad Autónoma de Ciudad Juárez, México)

SUPERVISOR: Dr. Gianluigi A. Botton

PAGES: xiv, 97

Lay Abstract

A wide variety of iron oxide-based materials are subject of study for an extensive range of magnetic applications in the daily life. A specific case of these materials is the called epsilon ferrite, a compound that exhibits interesting magnetic properties that can be used for different data storage applications. However, for integration of this material into electronic devices, high-quality thin films are needed. With the help of a detailed nanoscale characterization, a suitable structure of these thin films can be achieved. Therefore, an extensive characterization study of iron oxide thin films has been carried out with the purpose to understand the microstructure-functionality relationship of these samples and provide understanding that can be used to improve the quality of these films for a further real-world application.

Abstract

The discovery of the exotic magnetic properties of epsilon ferrite (ε-Fe_2O_3) has motivated several studies regarding the synthesis and device integration of this nanomaterial. However, due to the metastable nature of this phase, its application has been limited to nanoparticles or nanorods where the size confinement helped its stabilization. Recently the deposition as thin films was achieved on complex oxide substrates. However, in order to favor its integration into electronic devices, high-quality thin films are necessary. Distinct challenges are present in the growth of epitaxial films, the search for single domain and defect-free thin films with a unique magnetic easy axis is desired to obtain a good microstructure and achieve the exotic reported magnetic properties for the other nanocompounds.

In this work, a series of Scanning Transmission Electron Microscopy (STEM) investigations are presented with the purpose to gain insight about the microstructure and chemical state of epsilon ferrite thin films grown on vicinal strontium titanite (STO) and yttrium-stabilized zirconia (YSZ). Detailed analysis of high-resolution STEM images and electron diffraction patterns highlighted the, growth of misoriented in-plane domains with its easy magnetic axis pointing in opposite directions and edge dislocations in the grain boundaries. In specific cases, different mechanisms of partial strain relaxation are observed. For the samples grown on STO substrates, a set of misfit dislocations at the interface are visible while in the samples grown on YSZ the growth of a secondary phase at the film/substrate interface was identified. Electron Energy-Loss Spectroscopy (EELS) was used for chemical characterization of the sample helping the identification of the localization of a secondary phase growing at the interface, identified as magnetite. Further EELS analysis showed changes in the bonding conditions of the iron cations allowing to stablish a correlation between the strain effects (such as plastic deformations, the presence of dislocations, lattice distortion and secondary phases) and the magnetic moment of the sample. The presence of these types of defects and their relationship with the reduced magnetic response of the sample and is discussed in the following thesis.

Acknowledgements

Throughout my stay at McMaster University I was so lucky to find wonderful people that just one page wouldn't be enough to express my gratitude. First, I would like to thank my supervisor Dr. Gianluigi Botton for giving me the opportunity to be part of his research group, his support and guidance throughout my stay at McMaster. Dr. Alain Pignolet and Luca Corbellini from INRS Centre Énergie, Matériaux et Télécommunications for providing interesting samples to analyze. Dr. Nabil Bassim and Dr. Adrian Kitai for being part of my committee. Thanks to the Canadian Centre for Electron Microscopy staff: Dr. Carmen Andrei, Dr. Shaobo Cheng, Andy Duft and Travis Casagrande for all their help regarding any situation in the lab.

One of the persons I am truly thankful is my dear friend Alexandre Pofelski. Thank you, Alex, for all your help and endless discussions including microscopy, materials science, soccer and daily life issues. Of course, all the members from the JHE A406 thank you for all the memories: Viktor Kapetanovic, Isobel Bicket, Eric Daigle and everybody for the last two years in this wonderful office, including the visitor students Catalina Coll and Ramon Manzorro more than colleagues, thanks for your friendship, because every day of work was also a day to enjoy.

None of this would be possible without the love and support from my family; my parents Elsa and Alfredo and my brother Carlos. For all the help and sacrifices they have done for me throughout my whole life. SÍ SE PUDO.

The financial support from the National Council of Science and Technology from Mexico (CONACYT) is extremely appreciated.

Contents

List of Figures

List of Tables

List of Abbreviations

- Transmission Electron Microscope (TEM)
- Scanning Transmission Electron Microscope (STEM)
- High Resolution Transmission Electron Microscopy (HRTEM)
- Atomic number (Z)
- Pulsed Laser Desposition (PLD)
- Strontium Titanate (STO)
- Yttrium-stabilized Zirconia (YSZ)
- Annular Dark-Field (ADF)
- Nano-Beam Electron Diffraction (NBED)
- Electron Energy-Loss Spectroscopy (EELS)
- Magnetic moment (μ)
- Saturation magnetization (Ms)
- Coercive Field (Hc)
- Remanence (MR)
- Lanthanum hexaboride (LaB_6)
- Field Emission Gun (FEG)
- Energy-Dispersive Spectroscopy (EDS)
- Bright-Field (BF)
- Dark-Field (DF)
- Fast Fourier Transform (FFT)
- High-Angle Annular Dark Field (HAADF)
- Zero-loss Peak (ZLP)
- Full-Width Half Maximum (FWHM)
- energy loss near-edge structure (ELNES)
- extended energy loss fine structures (EXELFS).
- Transition Metal (TM)
- Geometrical Phase Analysis (GPA)
- Focused Ion Beam (FIB)
- Scanning Electron Microscope (SEM)
- Selected Area Electron Diffraction (SAED)
- Out-of-phase Boundaries (OPB)
- Anti-phase boundaries (APB)
- Zone Axis (ZA)
- Canadian Centre for Electron Microscopy (CCEM)

1 Introduction

Over the last years, the exotic ferroelectric properties exhibit by complex oxide-based materials have attracted the attention of several researchers. Examples of these interesting properties are: electric transport (Ohtomo & Hwang, 2004), magnetic phenomena at interfaces (Yamada et al., 2004), stabilization of unusual phases (Zeches et al., 2009), construction of phase boundaries and creation of magnetic and polarization orderings (Chu et al., 2008). Surfaces and interfaces properties usually differ from the same phases in bulk form since the presence of different ion arrangements can induce electron compensation leading to oxidation processes. Moreover, when the material is in thin film form, phenomena like antiphase boundaries can generate distortions in the bonding conditions that generate presence of exotic electronic and magnetic properties (Jang et al., 2015).

In the context of the nanoscale characterization of materials, the Transmission Electron Microscope (TEM) has become a powerful analytical tool going from defect characterization at micro scale until atomic resolution imaging and spectroscopy. Back in the 30s, the first electron microscope was developed by Knoll and Ruska (1931) and started to be used for the analysis of micro and nanoscale properties of several types of samples. The main advantage of this device relies in the power to magnify features that were out of the conventional microscopes' range. By using electrons, it is possible to achieve images with a high spatial resolution approximately in the picometer scale. The recent advances of energy-filtered and aberration-corrected STEM filter have allowed the achievement of atomic-resolution imaging and spectroscopy that help us to get more information about nanoscale defects, interfaces and atomic-resolved chemistry of multiple samples and even allowing in-situ studies about real-time transformations in materials(Gázquez et al., 2017; MacLaren & Ramasse, 2014; Schlom et al., 2014).

1.1Iron oxides.

Among the diverse types of complex oxides, iron oxides (ferrites) have always been subject of study due to their low cost and abundant presence on Earth as varied polymorphs with three main valence states; iron II, a mixed valence (II, III) and iron III. As a first example,

the iron II oxide can be found in mineral form called *wustite* containing only divalent Fe ions. Going further, iron (II, III) oxide possess a mixed valence state consisting in both Fe^{+2} and Fe^{+3} arranged in a cubic system generating the so-called *magnetite* (Fe_3O_4). Regarding the iron (III) oxides, with a chemical formula Fe_2O_3, they consist of Fe^{+3} ions that can be found in several atomic arrangements giving rise to a variety of polymorphs. Hematite can be described as a mineral having a rhombohedral lattice being the most common of all the mentioned ones due to its character as stable phase (Sakurai, Namai, Hashimoto, & Ohkoshi, 2009), showing an antiferromagnetic behavior. In addition, maghemite is represented by a cubic symmetry showing ferrimagnetism and can be also found as a stable phase in nature. In recent years, two metastable phases have also been studied for several applications: the beta phase (β-Fe_2O_3) which possess a BCC cubic lattice and suffers a phase transition to hematite at temperatures above 773 K, and the epsilon ferrite (ε -Fe_2O_3), a dark brown mineral with an orthorhombic crystal structure with interesting ferrimagnetism. The idea of producing ferrite materials launched a search of high quality nanostructures using chemical precipitation, sol-gel methods, chemical vapor deposition, atomic layer deposition, sputtering techniques and pulsed laser deposition (Teja & Koh, 2009).

A special case is the ε-Fe_2O_3, an intermediate phase between hematite and maghemite. The preferred way of obtaining this compound was as nanoparticles through chemical methods, Tronc et al in 1998 fully described ε-Fe_2O_3 crystal structure in addition to Mossbauer spectroscopy studies provoking a huge interest in the synthesis and magnetic properties of this oxide (Tronc, Chanéac, & Jolivet, 1998). It has been also obtained through nanoparticles embedded in silica matrices because size confinement mechanism helps to the stabilization at higher ranges of temperature (Ohkoshi & Tokoro, 2013).

After the successful synthesis of epsilon ferrite nanoparticles, Ohkoshi et al reported in 2004 a coercive field of 20 kOe in silica matrix-based nanoparticles, a higher value than any commercially available magnetic sample, including rare-earth magnets and Co-ferrites (Coey, 2012) was achieved. After this discovery, several attempts to fabricate nanoscale permanent magnets taking the advantage of its huge coercivity, single magnetic domain

nanostructures for data storage including distinct shapes like nanorods and nanowires were carried out (Sakurai, Shimoyama, Hashimoto, & Ohkoshi, 2008). Nevertheless, the success obtained for nanoparticles could not be reproduced for other structures, in the case of nanorods Carraro et al in 2013 reported that a mixture of epsilon and betta ferrite produced on silicon wafers by chemical vapor deposition did not exhibit a proper magnetic ordering moreover, these samples had a lower coercivity making them improper to the previously mentioned applications (Carraro et al., 2013).

Looking for its implementation in device technologies, thin films fabrication has been targeted as the best way of integration to obtain a suitable ε-Fe_2O_3 material keeping its interesting properties. The growth of epitaxial thin films of ε- Fe_2O_3 on perovskite substrates by pulsed laser deposition (PLD) has been recently reported (M. Gich et al., 2010), where the phase stabilization was accomplished through the epitaxial strain induced by the substrate, in this case being strontium titanate (STO), to achieve this purpose. An alternative substrate for such epitaxial films, more appropriate for devices than perovskites substrates since it can be grown on silicon (Jun, Kim, Lee, & Kim, 2001), is yttrium stabilized zirconia (YSZ). Initially, it has been shown that the growth of ε- Fe_2O_3 can be achieved through the deposition of a $GaFeO_3$ 50 nm thick buffer layer on top of YSZ for promoting the ε-Fe_2O_3 growth (Thai et al., 2016). Recently, ε- Fe_2O_3 epitaxial films have also been obtained on top of YSZ films, without buffer layer (Luca Corbellini et al., 2017). For a improved microstructure, it is necessary to ensure a single-phase ε-Fe_2O_3 and epitaxial films with a unique easy axis; multiple in-plane domain growth where dislocations and grain boundaries modify the magnetic behavior of this material, thus severely affecting the distinctive properties of interest.

1.2 Research objectives and overview.

The emerging generation of functional nanomaterials with exotic physical properties has motivated an in-depth analysis to understand the structure-property relationships at the nano and atomic level. In addition, the development of atomic-resolution imaging and spectroscopy techniques has allowed more precise studies about diverse and localized

phenomena that can take place in bulk, surfaces and interfaces. By understanding the origin of interesting properties due to these localized phenomena, further device technology applications can be made. In our specific case, the interesting magnetic properties of epsilon ferrite (ε-Fe_2O_3) have motivated several approaches for the synthesis as thin films in order to take advantage of the unique functional properties that make it a viable candidate for permanent magnet and high-density magnetic recording applications. However, to ensure solid-state device integration, high-quality thin films need to be achieved.

A series of electron microscopy studies of ε-Fe_2O_3 epitaxial thin films on yttrium stabilized zirconia (YSZ) and strontium titanite (STO) grown by pulsed laser deposition (PLD) were carried out. Crystalline growth was analyzed using scanning transmission electron microscopy (STEM), annular dark-field (ADF) imaging, as well as Nano-Beam Electron Diffraction (NBED). Furthermore, electron energy loss spectroscopy (EELS) measurements, were used to explore at the distribution and chemical composition of the films, these with the purpose of:

- Characterize the atomic arrangement and electronic structure of iron oxide thin films. Knowing the difference between the reported behavior of nanoparticles, nanorods and thin films by probing the electronic environment, it becomes possible to explain the origins of the multiferroic properties of thin films considering their quantum origin.

- Understand growth mechanisms and epitaxial relationships between film and substrate. The structural similarities between film and substrates lead to the formation of interfaces and promote domain orientation that can affect the distinctive properties of interest.

In the following chapters the characterization of iron oxide epitaxial thin films will be shown and discussed. Starting with a theoretical background including a quick review of ferromagnetic properties in iron oxide, transmission electron microscopy and spectroscopy, epitaxial thin films; growth mechanisms, strain effects and phase stabilization will be given.

In the next chapter, the experimental techniques used during this research process will be listed: a summary of the pulsed laser deposition synthesis methods, the sample preparation for TEM analysis as well as the distinct TEM techniques and equipment used at the Canadian Center for Electron Microscopy for this characterization work. The experimental results and discussion of the analysis will be split in two sections: first, a structural characterization of iron oxide grown on perovskite materials, a comparison between two distinct substrates, and, second, the ion distribution and electronic environment for epitaxial thin films. Finally, a summary and general conclusions about the study of these epitaxial films will be given.

2. Literature Review

2.1 Magnetic behavior of materials

The origin of the magnetic behavior in materials lies on the orbital and spin motion of the electrons and their interaction with others, generating a magnetic moment known as *Bohr magneton*, with an associated magnetic moment that can be described as a magnetic dipole. From a classic point of view, an electron rotating around an axis with angular moment **L** is described in Eq. 2.1.

$$\mu = \frac{-e}{2m}\boldsymbol{L} \tag{2.1}$$

Where *e* represents the elemental charge, m is the mass of the electron and **L** can be described as orbital, spin or total angular momentum (Fig. 2.1). According to this statement, every material on Earth should exhibit a magnetic behavior since all of them possess electrons. However, in most elements, these magnetic moments cancel each other generating a weak or null reaction to applied magnetic fields. Among the causes of the cancelation of the electron's magnetic moments, Pauli exclusion principle states that two electrons with the same spin cannot occupy the same energetic level making the spin magnetic moment equal to zero, also at molecular level, the net magnetic moments of orbitals tend to cancel each other.

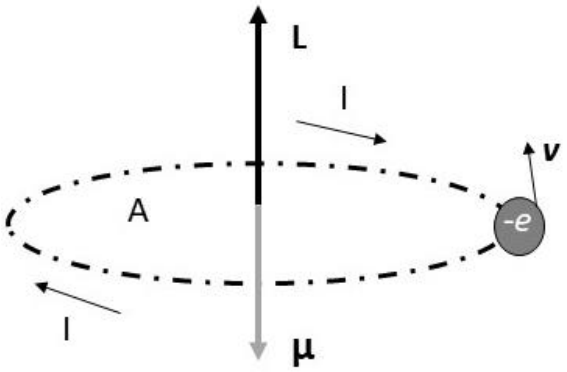

Fig. 2.1 Graphical representation of an electron orbital; indicating the direction of the resulting magnetic and angular moments.

However, in specific cases, such as transition metals, these atoms exhibit partially occupied electron orbitals; electron without paring that lead to a net magnetic moment.

Considering that any electric charge in movement can generate a magnetic field H, the amount of magnetic field flux or inductance B as the total magnetic field lines relates to the permeability of the medium as constant of proportionality:

$$\boldsymbol{B} = \mu_0 \boldsymbol{H} \tag{2.2}$$

When a magnetic field is produced by the electrons from certain material, the density of magnetic moments per unit volume is defined as:

$$\boldsymbol{M} = \frac{\boldsymbol{\mu_T}}{V} \tag{2.3}$$

These concepts are related by the so-called magnetic susceptibility, a dimensionless quantity that describes how much sensitive is the response to an external magnetic field:

$$\chi = \frac{d\boldsymbol{M}}{d\boldsymbol{H}} \tag{2.4}$$

As introduced before, in presence of an applied magnetic field, every material will respond in certain manner according to the reaction of its internal magnetic moments. Four distinct types of behavior will be introduced as follows (Fig. 2.2):

- Diamagnetism: Since all the electron are paired, the atoms only possess a net orbital moment and no spin moment, all the internal magnetic dipoles are aligned in an opposite way from the applied field.
- Paramagnetism: Unlike the previous case, here atoms have unpaired electrons resulting in a net magnetic moment. Applying an external field will align the internal magnetic dipoles however, this effect will be lost as soon as the field is removed.
- Ferrigmagnetism: Here, the magnetic moments from all cations will align in a preferential direction meanwhile the anion sites will follow an opposite direction,

since the intensity or number of dipoles is not equal, this will result in a net magnetic moment.

- Ferromagnetism: Magnetic dipoles are easily aligned with the applied magnetic field since the orientation of one dipole influences the orientation of the remain dipoles. This behavior is typical from elements that have a partially occupied 3d orbital.

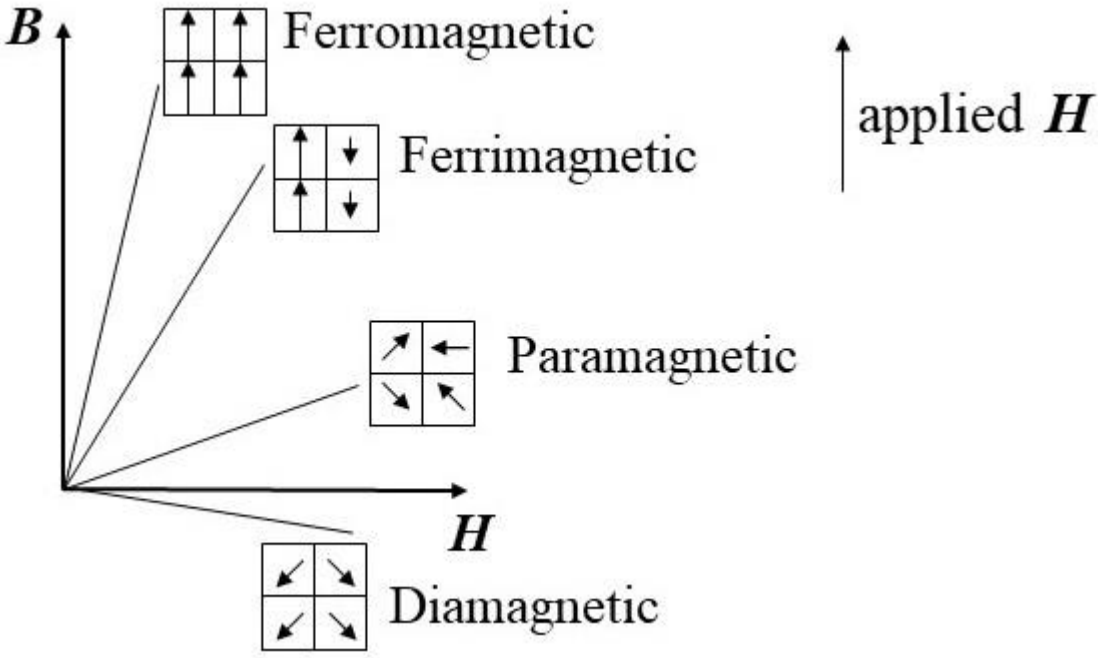

Fig. 2.2 Schematic diagram of possible magnetic moment alignments in ferromagnetic, ferrimagnetic, paramagnetic and diamagnetic materials. Drawing inspired from (Askeland, Fulay, & Wright, 2011)

According to the previous list, we can divide the magnetic response of materials in two groups; one where each magnetic moment acts independently and there is no interaction with the rest of the dipole (diamagnetism and paramagnetism). On the other hand, ferrimagnetic and ferromagnetic materials are characterized by the strong coupling between their internal magnetic moments. With the purpose of describing this magnetic interaction between neighbors, Dirac and Heisenberg (1926) formulated the exchange interactions as fundamental effects that direct the magnetic ordering of close atoms, based on the

overlapping of localized electrons (Coey, 2009). The exchange interaction will result in different sets of alignment represented by the spin state (S_i, S_j) and an exchange constant *J* whose sign, positive or negative will result in parallel (ferromagnetic) or antiparallel (antiferromagnetic) interaction, respectively.

$$-2J(S_i \cdot S_j) \tag{2.5}$$

In certain ionic compounds, the interaction between magnetic cations will be carried out by an intermediary ion. In the case of metals, a magnetic ion will induce certain spin change in the conduction electrons that will lead to an indirect coupling between the other magnetic ions. A further case is called *superexchange*, where ions can be coupled through a non-magnetic material despite a large separation distance. This behavior mainly corresponds to transition metal oxides. As an example of this, a metallic ion M^+ which has a partially filled d shell with a spherical symmetry while another non-symmetric metallic. The coupling happens through the interaction of the oxygen ion which would lead to a coupling between cations depending on the orientation of the magnetic moment, type and angle of the orbitals. Superexchange is the main magnetic interaction in oxide materials, in most cases the ferrigmagnetic behavior observed in these compounds is the result of an antiparallel alignment of not-equal sized ions, generating a net magnetic moment determined by orbital's features such as energetic level or angle (Fig. 2.3).

Fig. 2.3 Representation of a superexchange interaction in an oxide system.

Once the magnetic response of material has been explained, a further description of the internal magnetization will be extended. Small regions called *domains* where the magnetic dipoles are aligned in certain directions, these regions are enclosed by the so-called *Bloch walls* where the dipole direction can switch gradually. The application of an external field will produce a domain alignment until all of them reach a parallel orientation with respect to the external field, this situation is called *saturation* (M_S). When removing the applied field, magnetic domains will keep certain orientation resulting non-zero magnetization called *remanence* (M_R). The total magnetic field needed to demagnetize a material is called *coercive field* (H_c). If the external field is now applied in the opposite direction, the domains will reach an inverse orientation and now the process will take place in an analogous manner until the original configuration is reached; this entire process is known as hysteresis loop (Fig. 2.4).

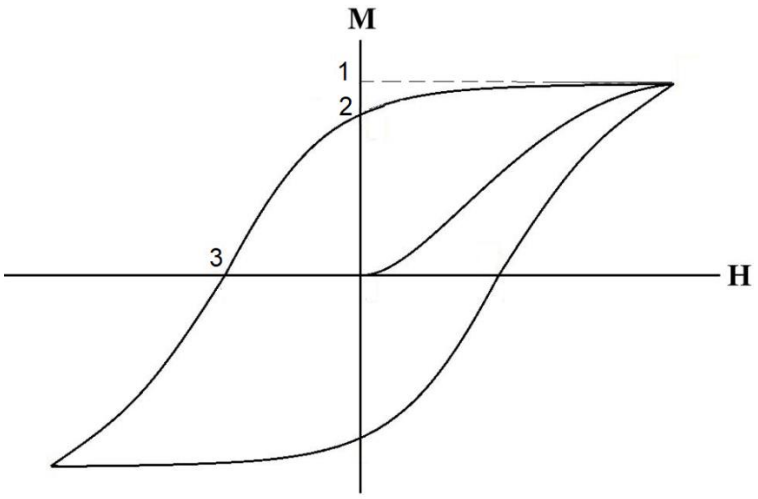

Fig. 2.4 Model of hysteresis loop showing the interesting points M_S (1), M_R (2) and H_C (3).

Depending on the shape of the described curve, some properties of the material can be inferred and be classified in two main categories:

- Hard magnets: Once magnetized, these materials will retain most of their configuration, almost same values of M_S and M_R and require a large applied field to demagnetized (large H_C); these materials show a broad squared hysteresis loop.

- Soft magnets: As an opposite case, these materials will present a narrow curve with small values of M_R and H_C. Resulting in an easy magnetization-demagnetization process.

The ferromagnetic response of a materials tends to lie along a determined axis, this property is commonly named *anisotropy* and is typical of hard magnetic materials. If the magnetization is different when the applied field lies along another direction reflecting the crystal symmetry, this is an example of *magnetocrystalline anisotropy* (Fig. 2.5), whose origins could be the crystal-field interaction, spin-orbit coupling or dipole interactions (Coey, 2009). Two main sources of magnetocrystalline anisotropy can be mentioned:

- Single-ion: As consequence of electrostatic interaction, crystal-field and spin-orbit interactions will align the magnetic moment in a particular direction.
- Two-ion: Magnetic ions, each with a given magnetic moment will tend to align head-to-tail over the entire lattice, where the sum will vanish to certain positions.

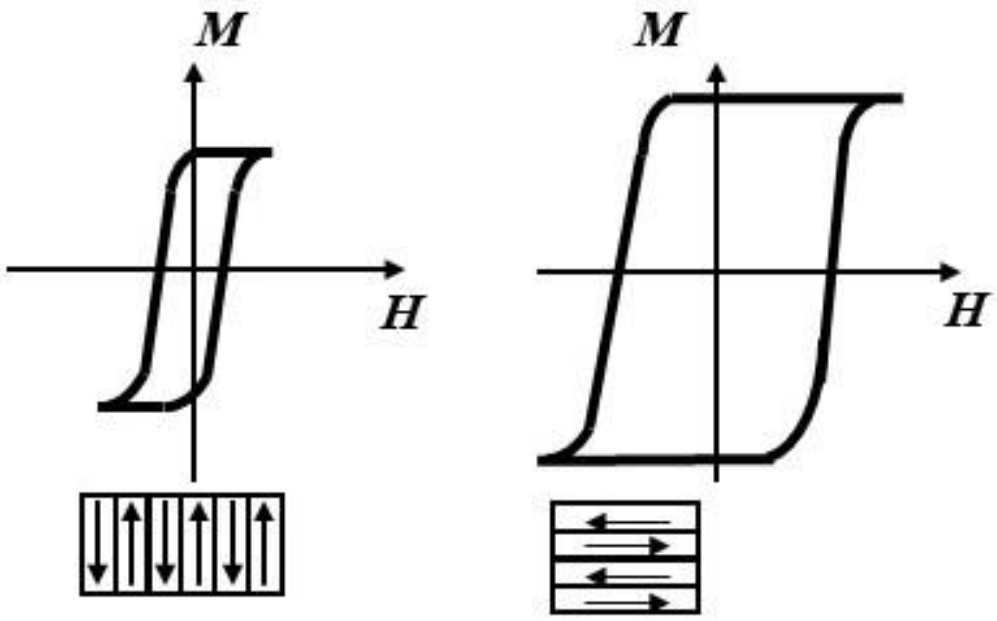

Fig. 2.5 Magnetization of an anisotropic material showing the hysteresis loops according to the magnetic dipole alignment. When dipoles are aligned (left) and parallel (right) perpendicular to the applied field. Drawing inspired from Coey, 2009.

2.2 Transmission Electron Microscopy

2.2.1 Basics of TEM

The importance of using a TEM in the nanoscale characterization of materials lies in its high power to magnify and resolve localized features at the sub nanometer scale, what is known as spatial resolution. The biggest advantage of the electron microscope over the conventional optical microscope to magnify objects is the limiting factor of light's wavelength in comparison with electrons, the small wavelength from the latter makes possible to resolve smaller features. The wave-like behavior of electrons was described by Louis de Broglie (1925), stablishing the wavelength of an electron as the ratio of the Planck's constant and electron's momentum as follows:

$$\lambda = \frac{h}{\sqrt{2meV}} \tag{2.6}$$

Where the product of the mass (m) and elemental charge of the electron (e) and certain accelerating voltage (V) can achieve a wavelength on the sub nanometer order. The practical resolution (r) of a TEM, including aberration correction C_s, is given by the following approximation:

$$r = 0.91(C_s\lambda^3)^{1/4} \tag{2.7}$$

Typical values of r vary between 0.25-0.3 nm. However, the best resolution devices can achieve a resolution of 0.07 nm (Williams and Carter, 2009).

The typical TEM design consists on a column that contains a filament gun, accelerator and series of electromagnetic lenses mounted on top of each other (Fig. 2.6), distinct electron sources can be used as filament being the two most popular thermionic and field emission guns (FEG); the first type are usually tungsten or LaB_6 are materials with low work functions, allowing an easy electron extraction and generating larger diameter probes than FEGs. Once the electrons are extracted from the gun they experiment an acceleration voltage that can varies from 80 to 300 keV (for a FEI Titan 80-300) and make electrons reach a speed close to the speed of light, reaching a condenser area where a set of lenses

and apertures guide the electron beam. Those condenser lenses, a setup of copper coils that generates an electromagnetic force strong enough to bend the electrons towards an optic axis, acting as focusing mechanism, before interacting with a specimen, the electron beam experiences the strong influence of the objective lens that defines the image focus.

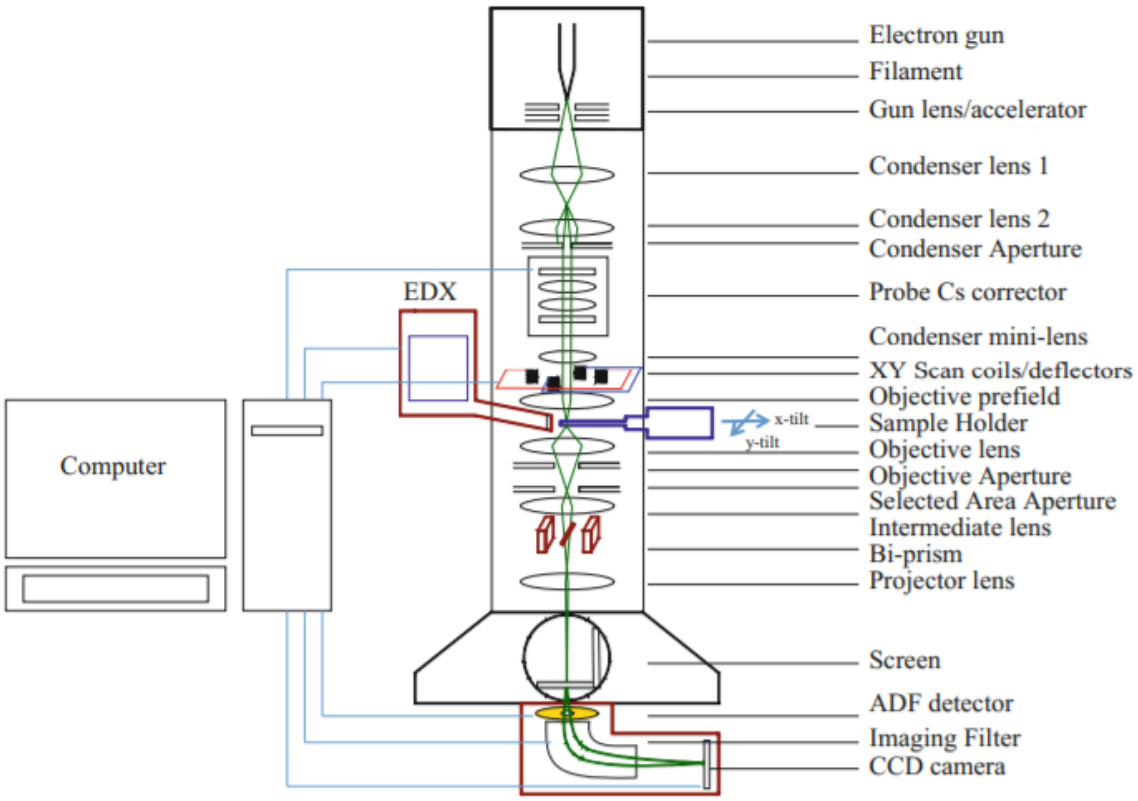

Fig. 2.6 Modern TEM column schematic including optical components and attachments. Republished with permission from (Jian Min Zuo & Spence, 2015); permission conveyed through Copyright Clearance Center, Inc.

2.2.2 Electron-matter interaction

When a high-energy beam interacts with matter, the Coulomb interaction between atomic nuclei and incident beam generates a series of scattering events for the coming electrons. Some of the electrons might suffer elastic scattering where almost no energy is lost and can be used to create images and diffraction patterns, while another portion will experiment inelastic scattering transferring part of their kinetic energy to electrons from the atoms in the sample. Once the electron-specimen interaction occurs, several signals are produced,

and devices are used to detect and process them; transmitted electrons from the sample generate dark-field and bright-field images, diffraction patterns, even x-ray (X-ray energy dispersive spectroscopy, EDS) and inelastically scattered electrons (EELS) can be collected to obtain information about chemical state of the sample (Fig. 2.7).

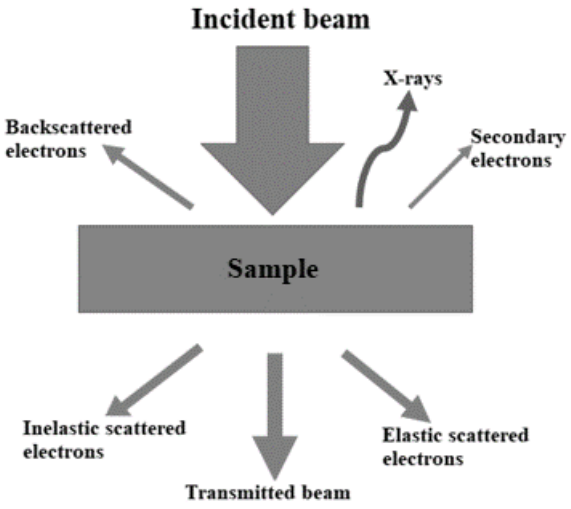

Fig. 2.7 Electron-matter interaction schematic.

Elastic scattered electrons may come from single or multiple atoms, in the first case as incident electrons approach the atomic nucleus and will suffer a high angle scatter due to the strong electrostatic repulsion. The differential cross section for the scattered electrons was described by Ernest Rutherford (1911) and will be discussed in the next section. On the other hand, collective scattering requires the assumption of wave behavior (instead of particle as in Rutherford scattering), the incident beam is treated as plane waves that will be diffracted when it interacts with the atomic arrangement of the sample making the scattering of electrons occur at low angles. The angles of scattering, also known as diffraction angles is described by the Bragg's law (equation 2.8), where the angle of diffraction (θ) is related to the spacing of the atomic planes (d) of the sample and the wavelength of electrons λ. The scattering process is coherent, leading to the possibility of a constructive interference between the scattered electrons and diffracted beams, allowing the production of diffraction patterns.

$$n\lambda = 2d \sin\theta \tag{2.8}$$

In the inelastic scattering process incident electrons interact with free electrons from the conduction or valence band of the specimen. However, high-energy electrons can also interact with inner shells producing the transfer of inner electrons to the unfilled states above the Fermi level, provoking atom ionization. The required energy for this process has to be enough to excite an electron from the valence band into the conduction band or to eject it from the sample. The inner K shell electrons require a higher energy that outer L or M shell electrons. Once the atom is ionized, it goes back to its ground state by filling the empty vacancy in the inner shell by the transition of an outer shell electron, this process is typically accompanied with energy emission in the form of X-rays (Williams & Carter, 2009). The energy of this emission is totally atomic number dependent, therefore it makes it possible the identification of chemical information.

2.2.3 TEM imaging

When speaking about a magnified picture of a sample, the two most common imaging modalities in TEM are bright field (BF) imaging, where a transmitted beam (**0**) is used, while the second, dark field (DF) where a diffracted beam (**g**), which possesses phase differences due to scattering from the sample, can be selected through the placement of an objective aperture. For BF imaging the usage of an aperture in the back focal plane of the objective lens allows only the direct beam to pass resulting in the formation of an image from the sample-electron interaction, while, in DF imaging the aperture is used to block the direct beam and a diffracted beam is used to obtain information about the crystal structure of the film (Fig. 2.8). The interference between multiple transmitted and diffracted beams leads to the formation of image contrast, depending on the number of diffracted beam interfering with a transmitted beam, a certain number of lattice fringes appear in the image each correlated with an atomic plane. The electron scattering from a thin sample generates the mentioned contrast in TEM which turns out to be extremely sensitive, allowing the possibility to explore the atomic ordering of a specimen. However, this sensitivity is also affected by sample dependent factors such as thickness, orientation or instrument settings like perturbations in the objective lens. There is a strong dependence between the resolution of the phase contrast and the number of beams selected that are allowed to form the image

based on the objective aperture. Moreover, the usage of aberration corrector allows an increase of the objective aperture size, leading to improved spatial resolution and compensating the spherical aberration generated by higher-angle diffracted beams.

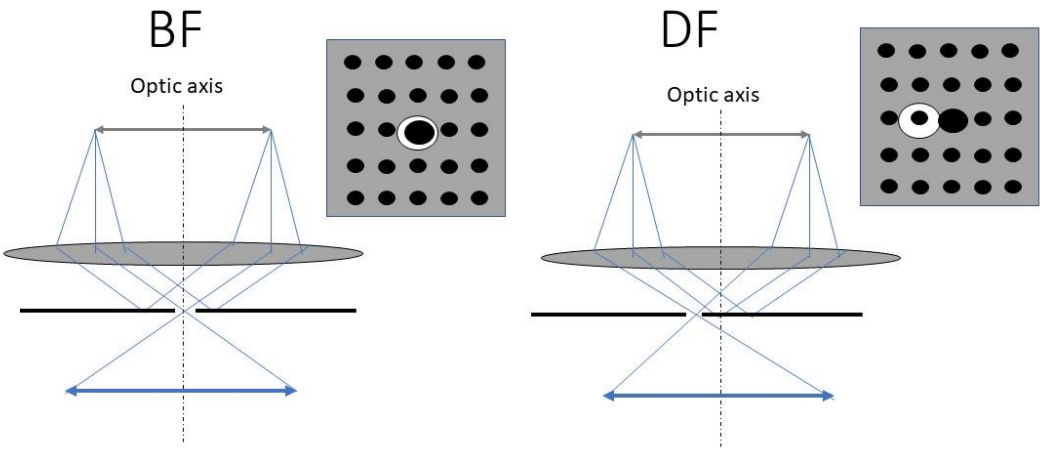

Fig. 2.8 Conditions for Bright Field and Dark Field imaging respectively.

The illumination system used in the TEM can be operated in two modes (Fig. 2.9), one is called parallel and was basically described in the previous paragraphs and used for BF/DF imaging, while the second uses a convergent beam and is also known as scanning transmission electron microscopy. We can identify distinct set of lenses in the STEM configuration, a first set called condenser lenses takes the electron beam to form an atomic-size probe. Then, scan coils are used to raster the probe around the sample generating a variety of signals that can be collected; depending on the angle of the trajectory described by the transmitted electrons with respect to the optic axis these can generated bright field images (low angles), annular dark field (high angles) and transmitted electrons that lost certain amount of energy when they leave the sample.

Right before the sample, the objective lens contributes to the final demagnification of the focused probe and where aberrations can generate significant blurring of the image. The usage of an aperture helps to limit the probe convergence and the amount of current available. An annular detector is now used to collect scattered electrons within an angular

range meanwhile the total incident beam is collected by the bright field detector right below the sample centered in the optical axis of the beam.

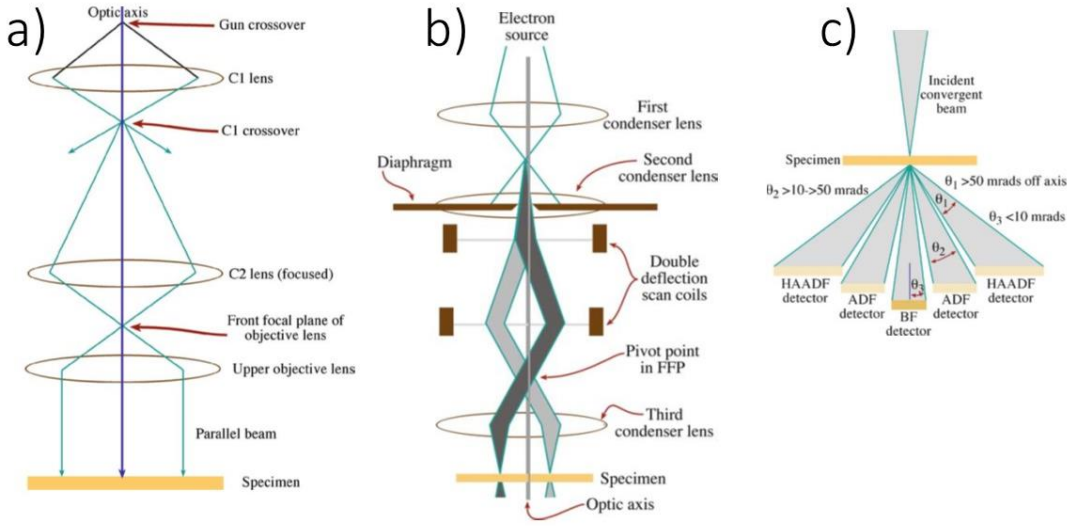

Fig. 2. 9 Schematic diagrams showing the illumination system for TEM (a) and STEM (b) modes and the HAADF detector setup (c). Image adapted and republished with permission from Williams and Carter, 2009; permission conveyed through Copyright Clearance Center, Inc.

When a specimen is exposed to an electron beam, the probability of any electron-matter interaction is defined as cross section which can vary depending of the incident beam's energy and the type of interactions and is described by the Rutherford scattering. Since the incident electrons travel at speeds close to light's, some relativistic corrections are incorporated to get the following expression:

$$\sigma_R = \frac{Z^2\lambda^4}{64\pi^4 a_0^2} \frac{d\Omega}{\left(\sin\left(\frac{\theta}{2}\right)^2 + \frac{\theta_0}{4}^2\right)^2} \tag{2.9}$$

Where Z is the atomic number and a_0 is the Bohr radius, θ is the scattering angle with a correction of θ_0 noticeable when incident electrons are far from the nucleus and for small scattering angles. The images obtained in STEM mode are strongly influenced by the atomic number (Z) of the sample and the scattering angle of the transmitted electrons. The collection of scattered electrons (which are mostly Rutherford scattered electrons from the

nucleus of the atoms) for STEM imaging is done by a high-angle annular dark field (HAADF) detector making the image sensitive to variations in the atomic number (Z-contrast) and much easier to interpret. The annular detector consists of a region in the scattering plane with an inner radius up to 100 mrad and an outer radius of hundred milliradians, where high angle scattering processes, at about 100 mrad would enhance the contrast from the sample (Pennycook & Nellist, 2011) making this type of imaging one of the most popular STEM techniques (Fig. 2.9c). A disadvantage of this imaging mode is the low sensitivity for small-Z elements.

In practice, several factors do not allow to obtain the theoretical resolution based on calculations based on the wavelength as equation 2.7. These situations are limited by aberrations produced in the electromagnetic lenses which can be present in two ways: spherical aberration, when the field effect of the lens changes for off-axis and on-axis electrons generating disk projections for point objects making the formed image blurred. On the other hand, chromatic aberration occurs when the electron beam possesses different ranges of energies modifying the focusing process for each set of energies. Notwithstanding, recent advances is aberration correction designs have improved the resolution of modern microscopes making them perfect for more accurate and higher resolution activities.

2.2.4 Electron Energy-Loss Spectroscopy

Among all the possible signals that can be collected in the TEM, inelastic transmitted electrons that pass through the sample are directed into a magnetic prism and an energy filter to generate a spectrum that displays the electron distribution as function of the energy-loss in the scattering process (Fig. 2.10). By measuring the kinetic energy of the electrons, it is possible to analyze their energy distribution and obtain information about the chemical state of the sample. To increase the power of the EELS techniques, measurements can be carried out in STEM mode and this improves the spatially-resolved acquisition in order to obtain atomic-resolution spectroscopy. Using a focused probe we scan at each pixel of a

predetermined area over the specimen and, by collecting an EELS spectrum, we form a 3D data array called spectrum image.

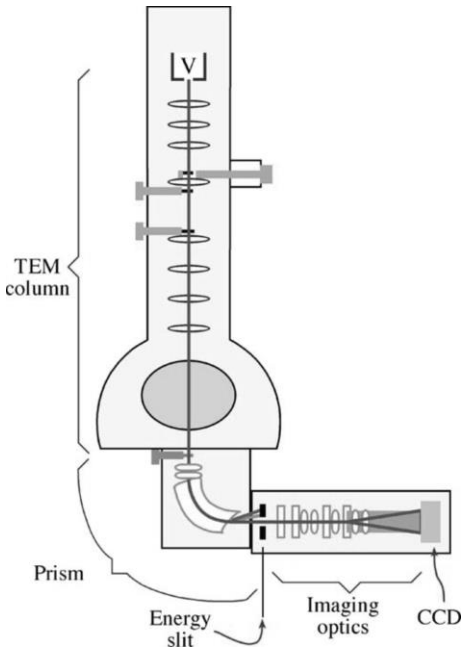

Fig. 2.10 Schematic of the EELS detector system attached to the TEM. Republished with permission from Williams and Carter, 2009; permission conveyed through Copyright Clearance Center, Inc.

An EELS spectrum consists in three main regions (Fig. 2.11), starting for the called zero-loss peak (ZLP) containing the elastic scattered electrons from the sample, which suffer a small or none energy lose and generally the majority of the signal collected during the acquisition; the importance of the ZLP lies in its use as parameter for calibration since it is the only fixed reference meanwhile the width of the peak, called full-width half-maximum (FWHM) can be used to know the energy resolution of the performed experiment (Browning, Arslan, & Erni, 2011). Up to 100 eV, the region known as low-loss region presents information on interactions with valence band electrons such as oscillations of electrons in the conduction band, called plasmon excitations generally useful to retrieve optical properties.

Beyond this region, the signal intensity decays abruptly and we observe the start of the core-loss region that contains information from core-shell electrons; when an incident

electron hits at atom, the imparted kinetic energy can be sufficient for a core electron to leave its ground level and be promoted into the unoccupied states, conduction band or even to be ionized; the ionization energy is a precise amount for individual atoms or simple molecules but, for crystal arrangements or large molecules, this energy might be slightly different. In this case, the excitations are displayed as edges instead of peaks and are named after each shell (K, L, M, etc.) equivalent to the main quantum numbers n = 1, 2, 3, …, representing where the electrons come from (Fig. 2.12) while the sub index (1,2,3,…,) indicates the orbital angular momentum s, p, d, f to label the peaks from high to lower energy within an electron shell (Radtke & Botton, 2011).

According to Radtke and Botton (2011) a single-electron process is needed for the description of inelastic scattering events; a mathematical description of the ground and valence states is carried out by writing their wave functions as delocalized single electrons, in order to interpret K and some L_{23} edges. For transition metal L_{23} or M_{23}, rare earth M_{45} and N_{45} edges, the overlap of ground and valence orbitals generate an asset of atomic multiplet effects, characterized by the coupling of spin-orbit momenta of the excited atom that are represented as features in the fine structure that cannot be explained by using a single-electron model (Radtke & Botton, 2011).

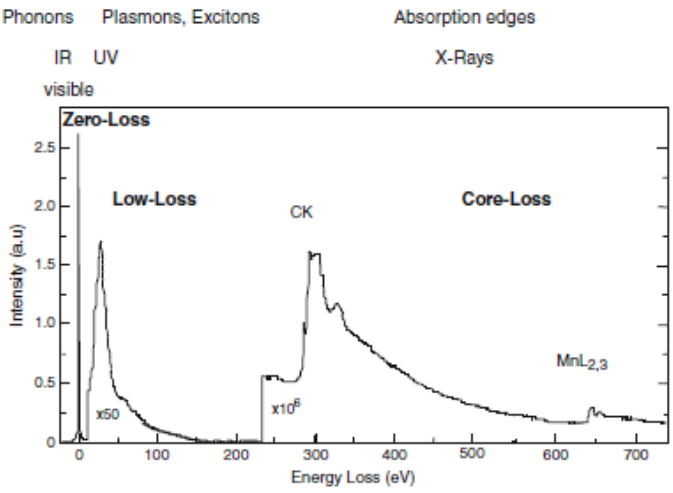

Fig. 2.11. Typical EELS spectrum showing the ZLP, low-loss and core-loss region. Republished with permission from (Kociak, Stéphan, Walls, Tencé, & Colliex, 2011); permission conveyed through Copyright Clearance Center, Inc.

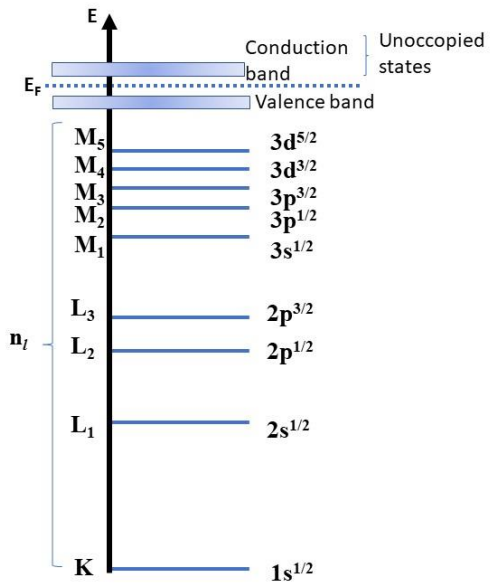

Fig. 2.12 Schematic representation of electron energy levels.

Based on theoretical calculations (Leapman, Grunes, & Fejes, 1982) L_{23} edge of fourth-period elements tend to be sharp and exhibit a peak in the ionization threshold because of the favored transitions to d-states where a strong overlapping with 2p electrons (core level) is present, these sharp peaks have been called *white lines*, which are generated by a high amount of empty d-states generates in solid materials. In general, two peaks are observed separated by certain amount of binding energy which is caused by spin-orbit effects (Egerton, 2011). The electron transitions that are prominent in the EELS spectra are constrained by the dipole selection rule: $\Delta l = \pm 1$, which dominant presence can be noticed in transition metal L_{23} edge (2p to 3d transitions) and M_{45} (*3d to 4f).*

The energy resolution of the TEM is seen as a limiting factor about the precision of the obtained information from spectroscopy. This can be either consequence of the energy spread of the incident beam or spectrometer issues. In the first case, electron sources can provide energy resolutions of 3 eV for tungsten, 1.5 eV for LaB6 meanwhile FEG and Schottky can provide sub eV resolution (Williams and Carter, 2009), to improve this, the use of a Wien filter (monochromator) to apply electromagnetic fields that allow certain energies of electrons to travel to the sample, an energy-selecting slit is used in the image

plane to make a small spread beam which will acquire finer details. In the spectrometer, a set of optical elements (magnetic quadrupole, sextupole, octupole, etc.) are placed to correct optical aberrations.

2.2.4.1 Energy Loss Near-Edge Structure

As mentioned in the previous section, the interaction between the focused electron beam and the specimen can generate the scattering or ejection of core and valence electrons from their ground energy level and occupy a higher energy state or leave the current atom. A ground electron will receive enough energy from the incident beam to either leave the atom or in some cases, when there is any unoccupied state and the transition is allowed, the electron can be promoted to that higher-energy orbital. The total amount of loss energy is proportional to the needed energy for certain transition to happen, by measuring these transition energies the electronic structure of the material can be studied.

The final state and energy level of the affected electron can reveal distinct information regarding to electronic, structural and chemical environment such as bonding conditions or oxidation state; this situation is represented by the amount of lost energy measured and embodied in the electron energy loss near-edge structure (ELNES) within the first electron volts of the edge. At higher energies, features can reveal information about the crystalline environment including interatomic distances and ligancy forming the called extended energy loss fine structures (EXELFS). These described parts show the bonding condition features of excited electrons and receive the name of fine structure.

The pronounced features observed before the ionization threshold can tell information about the density of unoccupied states, where the initial and final state must be different following the mentioned dipole selection rule, i. e. for the case of a K-edge, an initial s-state will occupy a final p-state while in a L-edge, the initial p-state tend to end up being a d-like state. Due to an extreme localization of ground-states, visible differences in the fine structure can be present even in the same element if the symmetry conditions vary.

According to the type of scattering suffered by the ejected inner electron, the ELNES fine structure can indicate a coordination fingerprint determined by the surrounding atoms that

impedes the trajectory of the excited electron (Tafto, J.; Krivanek, 1982). Depending on the type of coordination distinctive features can be observed in the ionization edges;

- For some trigonal cases, antibonding peaks are separated by 10-11 eV (Egerton, 2011).
- Tetrahedral coordination: In some cases, a small prepeak is observed around 1.9 eV before the first sharp feature, followed by a second peak around 7 eV and a third broad peak (Garvie, Craven, & Brydson, 1994).
- In octahedral sites, a sharp peak plus two broader features in K-edges (Brydson, Sauer, Engel, Thomas, & Zeitler, 1989).

Distortions in the symmetry of the sites can either broad or split the near-edge peaks (Buffat & Tuilier, 1987). Core hole effects and crystal-field splitting can make L_3 and L_2 edges look like two components at high energy resolution. The kind of electron source is being demonstrated to also affect the ability to resolve peak splitting if the energy width is around 1-2 eV. If FEG is used, the asymmetry of the emission profile might also affect. Using a small collection angle (<15 mrad) simplifies ELNES since nondipole transitions are excluded (Auerhammer & Rez, 1989). Many factors are responsible for the changes observed in the ionization edges of the core-loss region in the EELS spectrum, a variety of explanations are used to describe these situations, being the most relevant listed as follows:

- Multiplet theory and crystal field effects

The limitations of the one-electron approximation for atoms with partially filled 3d and 4f shells lie in the high degree of hybridization between 2p and 3d orbitals for the L_{23} edge (Anderson, 1966; Egerton, 2011). A good possibility to incorporate the influence of the electron environment is adding an extra term considering a Coulomb potential that introduces the electrostatic influence of the neighbor atoms. For transition metals (TM), the main effect of symmetry is the split of the 3d orbitals of the TM into three low energy states (t_{2g}) and two at higher energy (e_g) (Egerton, 2011). The main transitions observed in the spectrum can be described using the one-electron approximation, the split between the two white lines still generated by spin-orbit coupling. Effects of distorted bonding conditions,

like elongation of the axes and angles, can be represented as systematic splits in the L_3 peak into two sub-peaks (Radtke and Botton, 2011). For transition metal compounds, the splitting of 3d states is sensitive to its chemical environment; the d_{xy}, d_{xz} and d_{yz} and the two other d-orbitals lie along the axes, therefore the degenerate d-states split into t_{2g} and e_g levels separated by a parameter dependent on the symmetry of the anion sites (Fig. 2.13), making a splitting of both white line peaks (Egerton, 2011).

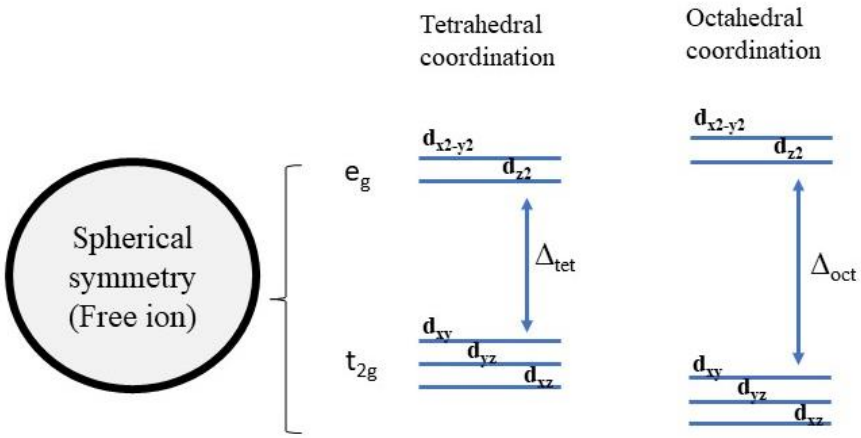

Fig. 2.13 Orbital splitting in transition metal oxides.

- Core-hole effects

When the incident beam knocks any inner electron from the sample and transmits its energy to it, a core hole is produced, generating a perturbation in the final state of the transition. In this case, the typical one-electron approximation used for the transition description fails since it is not considering the secondary effects from surrounding interactions. A two-particle approximation is then employed to include the interaction between the excited electron and the generated vacancy, for ionic compounds, this interaction (called exciton) is bounded stronger to the cation than the anion (Pantelides, 1975) seen as further features in the ionization edge; for s-states it will give a rounded shape meanwhile for p-states might be sharp (Mahan, 1975).

- Multiple-scattering

Multiple elastic scattering occurring when an electron is ejected from the core region plays a significant role in the near-edge region of the spectrum, distinct features can be originated

by the action of single and multiple scattering from nearest and second nearest neighbors (Wang, Egerton, & Malac, 2006).

2.2.4.2 White lines intensity

As mentioned earlier in the text, the ELNES structure of several transition metal oxides is characterized by the presence of two transitions called white lines, since their origin lies in the d-electrons transitions, a variety of information can be obtained related to the occupancy of the d-states such as charge transfer (Pearson, Fultz, & Ahn, 1988) and degeneracy of the initial state. Transition metals with partially occupied 3d states exhibit octahedral coordination can be found in two spin states; a high-spin state where the spin alignment corresponds to an arrangement in the e_g orbitals meanwhile a low-spin state is obtained by occupying t_{2g} orbitals with opposite spin (Radtke & Botton, 2011). The occupancy of the d orbital is also used to determine the ferromagnetic conditions present in amorphous alloys; changes in the white line intensity ratio relate the redistribution of electrons in the d-orbital with different spin states which lead to a magnetic moment modification (Morrison, Brodsky, Zaluzec, & Sill, 1985). In addition, the L_{23} ionization edge has been proven to relate to the branching ratio with high spin states in transition metal compounds (Koshino, Kurata, Isoda, & Kobayashi, 2000).

- *Oxidation State*

The energy level information of molecular orbitals in several compounds is mostly determined by the chemical and crystallographic structure of it, differences in energies between the ground and final states might give rise to chemical shifts. Muller (1999) stated that the core-level shifts in metals are determined by changes in the valence band; related to changes in type number and separation of atoms, being able to tell information about the occupied states (Muller, 1999). Positive and negative shifting in L_3 edges for transition metal oxides can be observed from1 to 2 eV (Leapman 1982) meanwhile K-edges are generally positive with higher range (from 0.7 to 10.8 eV) (Grunes, 1983). In the case of mixed-valence oxides, considering that the chemical shift increases with increasing the oxidation state, multiple edges can be observed with distinct separations of the white lines.

Transition metals have the possibility to present different oxidation states, depending on the number of electrons they lost when bonding to some other elements. Generally, when performing an EELS experiment, the incident beam will give certain amount of energy that can promote the core-electrons to unoccupied states, measuring the lost energy which is proportional to the electron transition can give an idea of the oxidation state by looking at features in the fine structure generated by the change in the number of electrons. The L_{23} edge has been used to check the valence state of transition metal ions like Mn and Fe, the differences in the near-edge are mostly ruled by the oxidation state and the dominant ligand environment contribution (Garvie et al, 1994). The intensity ratio of the two white line peaks should reflect the degeneracy of the initial state ($2p_{3/2}$ and $2p_{1/2}$) electrons (Thole, van der Laan, & Butler, 1988).

The energy-loss spectrum can suffer modifications generated by changes in the oxidation state (Radtke and Botton, 2011):

- Changes in the white-line ratio due to electron-hole interactions.
- Shifting to higher energies of the edge onset because of the oxidation of the ion; when the atom experiences the departure of a 3d electron, the nucleus attractive potential is reduced increasing the 2p binding energy.

Several methods can be performed to validate the oxidation state of a sample, being the white line intensity, also called the L_{23} ratio, one of the most popular (Tan, Verbeeck, Abakumov, & Van Tendeloo, 2012). The method consists in taking the integral intensity and calculate the peak ratio between the L_3 and L_2 edges that represents the transitions from $2p_{3/2}$ to 3d and $2p_{1/2}$ to 3d respectively. However, iron oxides present an ambiguous behavior besides oxidation state, such as coordination geometry and spin state also affect the white-line ratio making a non-monotonic relation between valence state and white-lines intensities, forcing the implementation of quantification methods (P. a. van Aken, Liebscher, & Styrsa, 1998). An alternative method to determine the valence state of iron oxide were described by (P. A. Van Aken & Liebscher, 2002), through the implementation of a double arctan function for background subtraction and two integration windows of 2 eV centered around the maxima of each white line; L_3 for Fe^{3+} and L_2 for Fe^{2+} giving results

with an absolute error around $\pm$ 0.04 which is considered a better alternative than other methods like the total intensity ratios. This method has been confirmed to exhibit better results than the conventional white line intensity ratio and has been implemented for further EELS analysis of this thesis.

2.3 Basics of thin film growth

In the beginning of the growth process, a single crystal substrate acts as seed for deposited thin film which once the crystallization started becomes a self-seed for the following deposited material (G. Cao, 2004). Nucleation and growth processes are usually limited to a simple situation where the size and shape of the initial nuclei depends only on the Gibbs free energy however, other interactions between the film and the substrate must be considered since they determine several feature in the film growth process. In a thermodynamic context, ferroelectric materials can be described is the following way:

$$dG = -SdT + x_i dX_i - D_i dE_i \tag{2.10}$$

Where G is the Gibbs energy, S is entropy, T is temperature, x and X are strain and stress components, E and D are electric field and electric displacement, it can be noticed the relation of electric properties with temperature and mechanical strain. Thin film growth of this materials can be done by various deposition methods, for purpose of this thesis, PLD will be used as an example to explain some features of epitaxial growth.

The formation of individual clusters from a vapor phase on any substrate is considered a typical process for thin film formation (Fig. 2.14). At the beginning, individual atoms form small nuclei and will acquire some thickness. During the process, some atoms can travel on the substrate and join stable nucleus. The thin film growth will be conditioned by some substrate's features. When faces' orientation differs one from each other they will present distinct structures, their surface energy will be determined by the crystallographic orientation and is extremely important when the epitaxial growth is carried out (Markov, 2003; Cao, 2004).

The general theory of thin film growth involves three modes of nucleation and growth, listed as follows:

- Island growth
- Layer-by-layer
- Layer-island

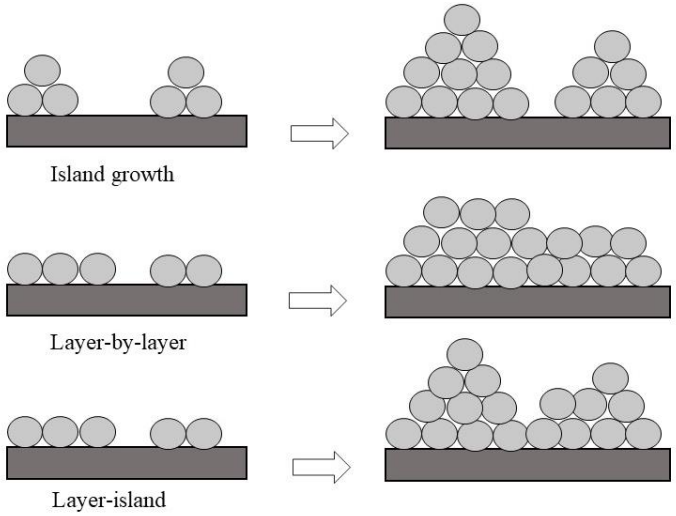

Fig. 2.14 Nucleation and growth process.

The selection of the type of growth depends on the surface energies of both film and substrate as well as the film-substrate interface energy. In island growth process, species are strongly bonded between themselves more than to the substrate. The deposited atoms can arrive directly to the substrate or to preexisting clusters, they can also move around the surface until they reach their final destination or even can suffer a reevaporating process (Cao, 2004). By inducing impurities or defects a reduction on the binding energy will stop the epitaxy and avoid the growth of amorphous layers. In the island mechanism, epitaxy can be described as a post nucleation of clusters. The Gibbs energy of atomic clusters can be described:

$$\Delta G = a_1 r^2 \Gamma_{c-v} + a_2 r^2 \Gamma_{s-c} - a_2 r^2 \Gamma_{s-v} + a_3 r^3 \Delta G_v \qquad (2.11)$$

Where the first term includes the radius and the film-vapor interface energy, the second is substrate-film, the third substrate vapor and finally the change in volume free energy. Due

to its direct dependence of r, clusters' Gibbs energy can decrease by growing when its radius is larger than a critical value ($\frac{\partial G}{\partial r}$), meanwhile at smaller radius they just dissolve as its Gibbs energy increases.

In layer-layer growth, there is a stronger bonding between the growth species and the substrate; once a first monolayer is completed, the deposition of the second begins. A strong film-substrate bonding, low film surface energy and high substrate surface energy will generate a full monolayer growth that can still involve island formation but with one-layer thickness. Layer-island growth can be described as a combination of the previous two mechanisms; first, atoms form a complete monolayer on the substrate to be followed by the nucleation of atomic clusters on top of these monolayers.

One of the parameters influencing the nucleation and growth is the supersaturation which is the ratio of the actual deposition and the equilibrium deposition value at temperature. Small values of saturation generate large nuclei (island growth) while a high saturation value leads to shrinking nucleus and atoms will be accommodate as layers (layer-by-layer mode) (Metev & Meteva, 1989). Substrate temperature can also play a significant role in thin film growth process, typically high temperature contributes to a higher surface mobility and crystallization rate, however if it is too high, can lead to distortion in the crystallinity. Therefore, this is a key factor for crystal structure, orientation, composition and morphology (Ohring, 1995). A relation between these factors and the chemical potential (μ) can be stablished by:

$$\mu = k_B T \ln s \tag{2.12}$$

Nucleation models and growth mechanisms described before are applicable either to the formation of single crystal, polycrystal and amorphous films, where the conditions of the growth method and substrate will determine the nature of the product. Especially the growth rate and deposition temperature will have a higher impact in the resultant material. To summarize, the growth of single crystals turns to be the most difficult due to the need of an extremely clean surface to avoid secondary nucleation, high temperatures to ensure good mobility and low rate growth to enhance surface diffusion of deposited atoms.

Amorphous deposition requires a low growth temperature or a high flux of species that generate a quick adhesion of deposited atoms. Finally, polycrystalline growth would lay in between these two conditions using a moderate temperature generating a reasonable surface mobility of species. When the substrate presents certain features like miscuts; atomic steps with terraces and edges, in case of optimal conditions, nucleation may occur on the terraces. In real growth process, point defects, atomic steps and dislocations will act as nucleation preferential sites (Cao, 2004).

The most part of complex oxide deposition process look to produce thin films in specific or conventional substrates to obtain cheap, high quality and multifunctional products but most important to favor its integration in device applications. The growth of epitaxial thin films on single crystal substrates is crucial to the stabilization of the metastable epsilon phase of iron oxide. The term epitaxy can be defined as a particular crystallographic arrangement upon something with a crystallographic orientation. Depending on the nature of the deposited film compared with the substrate, two types of epitaxy can be found: homoepitaxy if both film and substrate have the same composition and structure, otherwise is called heteroepitaxy. When a crystalline material starts to grow on a single crystal with a preferred orientation, the difference in lattice parameter (a) between the deposited oxide and the chosen substrate will lead to a heteroepitaxy growth where the main difference will be the lattice mismatch between these two, which is given by the expression:

$$f = \frac{a_{film} - a_{substrate}}{a_{substrate}} \tag{2.13}$$

Where the present mismatch can be compressive ($f < 0$) or tensile ($f > 0$). The influence of the mismatch can be noticed in different epitaxy features such as the growth and nucleation process, presence of dislocations and quality of crystallinity. Generally, low mismatch systems (1-2%) follow a layer-by-layer growth and produce a film with similar crystal structure as the substrate, while, larger mismatch can present island growth. Once the film presents certain thickness, the formation of defects will relax the epitaxial strain (Fig. 2.15)

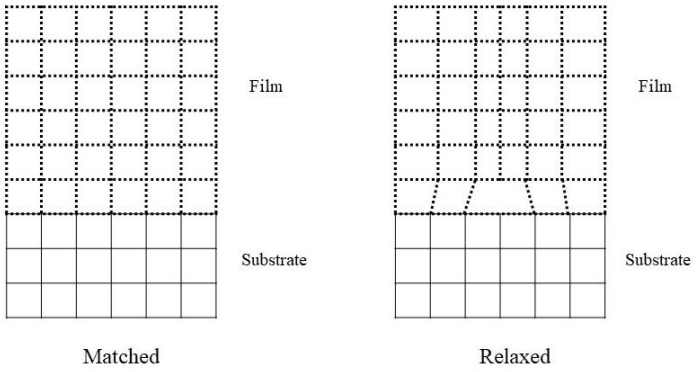

Fig. 2.15 Lattice representation of matched and relaxed epitaxial films.

As mentioned in previous growth reports; for the specific case of epsilon ferrite that exhibits a non-symmetric complex crystal structure and its phase stabilization is achieved through size-confinement mechanisms, the definition of lattice mismatch tends to be more complicated than the usual due to the lack of relaxed lattice parameter references (Corbellini, 2017).

When a material grows on top of a single crystal substrate which differs from its crystalline structure, lattice parameters or bonding conditions the process is called hard heteroepitaxy (Griesche, Enderlein, & Schikora, 1988). For this process, the nature of the chemical bonds will play a major role for epitaxial growth rather than the conventional definition of lattice mismatch (Zur & Mcgill, 1984). Moreover, changes in the thickness of a film is a factor to induce novel properties for thin films complex oxides, it can lead to a variety of effects: a decrease in coordination number, an increase grain size, grain boundaries, effective disorder and increase strain between substrate and film (Biswas & Jeong, 2017).

2.3.1 Strain and dislocations

Interfaces are defined as the limit region between two bulk phases where an epitaxial orientation exists between a substrate and an overgrowth crystal and the two crystals features can differ from what they usually exhibit in bulk as consequence of the nature of the chemical bonds or crystal lattice parameters. Boundaries can be found as layers where the difference in lattice parameters is accommodated by misfit dislocations or where a

homogeneous strain along the layer is used to match the periodicity of the substrate (Markov, 2003). When two adjacent crystals have a distinct periodicity of their lattices, their interface suffers a vernier of misfit. A specific case of this type of misfit accommodation is when the two crystal lattices are multiples of each other (Fig. 2.16). Misfit dislocations can be visualized as extra atomic planes where certain material presents a smaller atomic spacing (Fig. 2.16d). The effect of these dislocations in the local strain environment is the presence of opposite sign of strain at the core of the dislocation and its surroundings. Generally, when the lattice spacing of the epitaxially grown crystal is larger than the substrate, the core of the dislocation will be stretched out but the bonding conditions in between the dislocations will be compressed, and vice versa (Markov, 2003).

As introduced before, in the interface between two crystal structures, the presence of misfit dislocations arises to accommodate the lattice mismatch and it is important to distinguish between large and small mismatches. The nucleation of dislocations as a strain relaxation

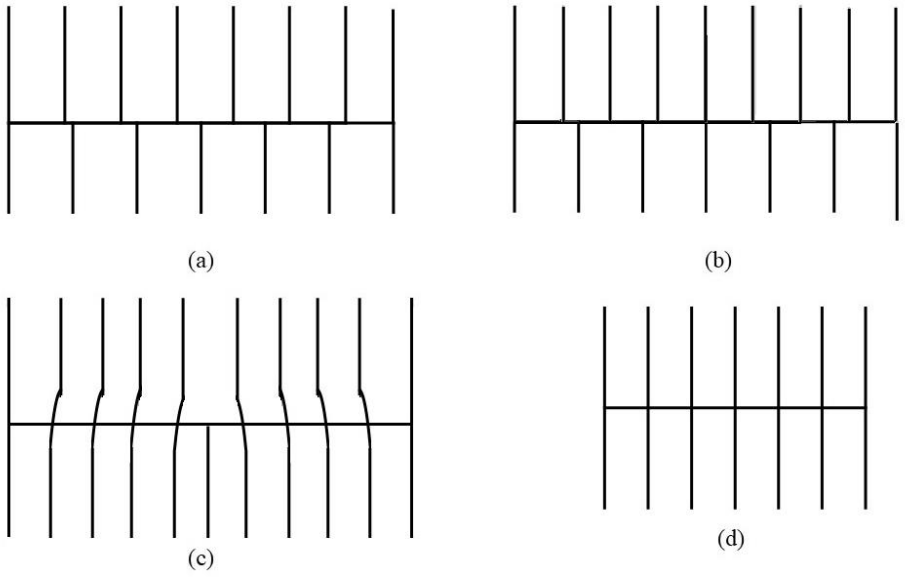

Fig. 2.16 (a) Representation of a vernier of misfit and periodicity of one lattice parameter as multiple of the other (b). A misfit dislocation arrangement (c) and homogeneous strained structure (d).

mechanism for thin films with large lattice mismatches generally occurs at surface steps and propagates towards the interface (Zhu et al., 2013), therefore the nucleation and later propagation of dislocations is extremely dependent of surface step conditions. Misfit accommodations have been catalogued as a complex phenomena for complex oxide interfaces and more diverse than the typical observed in semiconductors, mostly because of the presence of vacancies and variations in substructures and orbital hybridization, which are also responsible for the exotic electromagnetic properties exhibited (Pennycook et al., 2013). On the other hand, in the epitaxial growth of slightly lattice mismatch between a film and the substrate occurs in a coherent way, resulting in a homogeneous strained structure in comparison with the substrate (Van Der Merwe, 1950). The strain energy of a system is now defined as the sum of total energies of the dislocations and increases the total energy of the film compared with the relaxed unstrained structure, the mentioned strain energy tends to increase with the thickness of the film. In this type of strained pseudo morphic film, strain is described as array of coherent dislocations separated by one lattice spacing, also known as vernier of misfit (Ikuhara, 2001).

At certain critical value of thickness (h_c), the accommodations of lattice mismatch via misfit dislocations becomes energetically favorable generating a set of dislocations at the interface of epitaxial films, this has been interpreted as the action of coherent dislocations cancelling the strain field of anticoherent dislocations (Olson & Cohen, 1979). As discussed by Ikuhara and Shibata (2011), for intermediate thickness values, strain is accommodated by both coherent and anticoherent dislocations, where the later help to relax only a fraction of the total strain. When all the strain is accommodated by misfit dislocations, the coherent dislocations are canceled out and the film is fully relaxed with a semicoherent interface with constant spacing of dislocations. Typically, the formation of semicoherent interfaces occurs when the lattice mismatch is around 4-5% while in the case of larger mismatch values, the interface is expected to be incoherent involving a total lack of interfacial matching resulting in the appearance of the mentioned misfit dislocations (Ikuhara & Shibata, 2011).

2.3.1.1 GPA analysis

In order to clarify the effects of strain relaxation mechanisms, it is important to study the effect of the local strain fields and the generation of residual strain in the film. Geometrical Phase Analysis, (GPA) a method for quantification of high resolution electron microscopy images has been applied to numerous oxides, metal and semiconductor materials taking advantage of the spatial resolution that can be obtained (Kiguchi et al., 2011).

This mentioned technique was developed by M. Hytch (1998) (Hytch, Snoeck, & Kilaas, 1998) as an image processing routine that is sensitive to small changes in the lattice fringes with respect to a relative lattice reference in high resolution micrographs. Basically, the procedure consists in taking the Fourier transform from the selected image, that will exhibit strong Bragg reflections. Each component of the Fourier transform represents a lattice vector **g** which is related to the crystalline structure of the material. Followed by the application of a Fourier filter on the two main non-colinear reflections, an image is formed using these lattice reflections and its corresponding frequencies and it is possible to measure local variations in it. Even though the position of the fringes does not necessary tell the exact localization of atomic planes, the GPA analysis only considers the variation of the lattice positions and not absolute values. For zones where abrupt changes in the crystalline structure are present, certain amount of error can be induced, especially in interfaces where the effect of the objective lens can generate shifts in the lattice fringes and induce changes in contrast. The spatial resolution of the analysis will be directly dependent on the size of the used mask for the Fourier filtering.

The image from a crystal structure can be represented in a Fourier series as:

$$I(r) = \sum_{g} A_{g,P} e^{2\pi i(\boldsymbol{g}\cdot\boldsymbol{r})} \tag{2.14}$$

For the intensity *I(r)* at each position *r* with while the coefficient of the series depends on the amplitude *A* and phase *P* of the lattice fringes *g*.

The phase image obtained will describe the position of the lattice fringes by the following formula:

$$P(r) = -2\pi \boldsymbol{g} \cdot \boldsymbol{u}(\boldsymbol{r}) \tag{2.15}$$

For a determined displacement *u(r)* with respect to the selected reference lattice. Since there are two selected reflections to calculate a 2D displacement, the total displacement can be written as:

$$u(r) = \frac{-1}{2\pi}\left[P_1(r)a_1 + P_2(r)a_2\right] \tag{2.16}$$

For two basis vectors corresponding to each lattice reflection (a_1, a_2). Once the total displacement is known, the strain (ε_{ij}) and in-plane rotation tensors can be determined:

$$\varepsilon_{ij} = \frac{1}{2}\left(\frac{\partial u_i}{\partial x_j} + \frac{\partial u_j}{\partial x_i}\right) \tag{2.17}$$

$$\omega_{xy} = \frac{1}{2}\left(\frac{\partial u_y}{\partial x} - \frac{\partial u_x}{\partial y}\right) \tag{2.18}$$

For further reading and a fully understanding of the mathematical derivation please refer to Hytch et al 1998.

The work done by Li et al 2016, compares the behavior of strain maps when a dislocation is present at the interface of the film and substrate. Showing that dislocations possess a high value of compressive strain while across them the local environment can reach maximum values of tensile strain (Fig. 2.17).

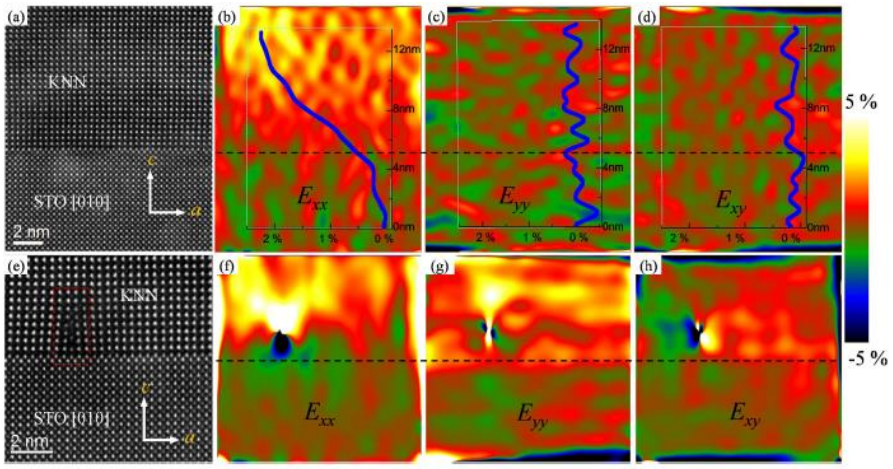

Fig. 2.17 HAADF image of an interface region without and with dislocation (a, e) showing its respective in-plane (b, f), out-of-plane (c, g) and shear strain maps (d, h) respectively. Reproduced from (Li et al., 2016), open access article under Creative Commons license (CC BY 4.0).

More examples can be found in the work done by E. Popova in 2017 where the strain relaxation is represented by evolution of the in-plane lattice parameter from the interface to the top of the film and the presence of non-tilted and tilted grain generates vernier of misfit and misfit dislocations respectively (Popova et al., 2017). Even the presence of new supercell structures can be detected by applying GPA analysis to study misfit defects and biaxial strain in complex oxide thin films (Zhu et al, 2013). The role of strain in epitaxial thin films includes several mechanisms to tune a variety of physical properties (J. Cao & Wu, 2011; Schlom et al., 2014) and allows the growth of metastable phases (Gich et al, 2010). However, its influence can also be extended to modifications in crystal structure and chemical composition. By choosing a substrate with similar crystal structure but a considerable difference in lattice parameter, changes in the epitaxial strain can be induced allowing to tune multiferroic properties (Dvorak et al., 2005; Sandiumenge et al., 2013).

2.4 Overview of epsilon ferrite

As mentioned in the introduction, distinct types of iron oxides have been used for a wide range of technological applications based on their respective electromagnetic properties. Epsilon ferrite presents an orthorhombic crystal structure with a space group of $Pna2_1$ and its lattice parameters for nanoparticles have been reported as a = 5.095 Å, b = 8.789 Å, c =

9.437 Å and angles $\alpha = \beta = \gamma = 90°$ (M. Gich et al., 2006). The orthorhombic unit cell is composed by four independent sites (Fig. 2.18); three showing an octahedral coordination (denotated as A, B and C sites) and one tetrahedral site (D site) (Tuček, Zbořil, Namai, & Ohkoshi, 2010). Studies have shown that these coordination polyhedra exhibit certain degrees of distortion (Gich et al, 2006) B and C sites have distorted coordination meanwhile the A site is found in a regular coordination. These distortions play a significant role in the magnetic behavior of the material because they are responsible for the generation of a nonzero orbital component to the total magnetic moment of the Fe^{3+} (Tseng et al., 2009). Moreover, the presence of four Fe sites in the crystal structure also determinates the magnetic nature of the sample; four sublattice magnetization are defined as M_A, M_B, M_C and M_D related to each coordination site, where M_B and M_C are found to be positive while M_A and M_D are negative showing an antiparallel ordering between M_A and M_B, M_A and M_C, M_B and M_D (Ohkoshi & Tokoro, 2013). Also, the super exchange pathway values related to the Fe sites is smaller for the tetrahedral site than the rest resulting in the smaller magnetization previously mentioned.

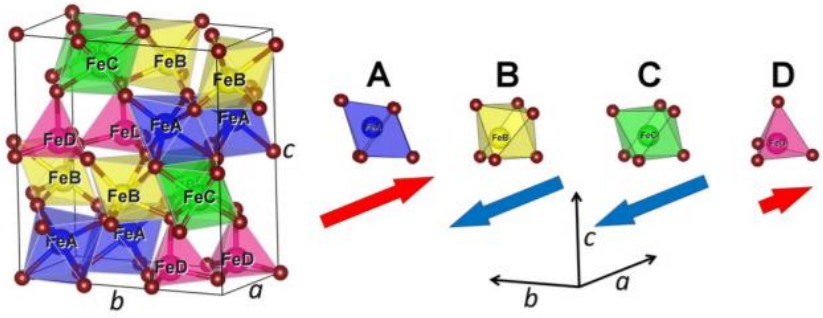

Fig. 2.18 Epsilon ferrite unit cell with four Fe coordination sites. Republished with permission from (L. Corbellini, Lacroix, Ménard, & Pignolet, 2017).

The exotic magnetic behavior described in the previous paragraphs lead to a series of interesting properties that have been studied and reported by several authors; even if they present a lower magnetization compared to other iron oxides, these materials exhibits a large coercive field that can reach 20 kOe for nanoparticles (Jin, Ohkoshi, & Hashimoto, 2004). The reported lattice distortion results in a large magnetocrystalline anisotropy.

Distortions on the B and C Fe sites will result in the mixing of the 3d orbitals from iron with the 2p orbitals from oxygen and a charge transfer from the O 2p to Fe 3d resulting in a non-zero L angular moment which in addition to spin-orbit effect will lead to a large magnetocrystalline anisotropy with the crystallographic a-axis as easy axis (Chen et al., 2009; Tseng et al., 2009).According to previous studies the exotic magnetic properties of the metastable epsilon ferrite and the simplicity of its chemical structure represent a great advantage over the known ferroelectric complex oxides (Martí Gich et al., 2014).

The emphasis on the metastable nature of the ε-Fe_2O_3 lies in the challenging character of its production. A first transformation for all four possible phases of iron (III) oxide was first reported by Sakurai et al in 2009; the coexistence of the four allotropes and their corresponding phase transformations were observed in nanoparticles of varied sizes. The synthesis of epsilon ferrite nanoparticles generally includes the impregnation of an iron precursor, named $FeSO_4$, $Fe(C_{10}H_9CHO)$ into a mesoporous silica matrix or reverse-micelle and sol-gel methods (Ohkoshi & Tokoro, 2013; Sakurai et al., 2009). From a thermodynamic point of view, the observed phase transformations occur thanks to the surface energy contribution of the nanoparticles inside the used silica matrix. Letting the Gibbs free energy (G) of each nanoparticle be described as (Sakurai et al, 2009):

$$G(i) = G_B(i) + \frac{6V_m}{d} G_S(i) \tag{2.19}$$

where the first term corresponds to the energy of the bulk and the second includes the molar volume, nanoparticle diameter and Gibbs surface energy. The G vs diameter curve (Fig. 2.19), indicates that distinct phases can be obtained based on the proper particle size; starting from the gamma phase and increasing the nanoparticle diameter to reach the next phases. However, two conditions must be satisfied (Sakurai et al, 2009):

i. $$G_B(\gamma) > G_B(\varepsilon) > G_B(\beta) > G_B(\alpha) \tag{2.20}$$

ii. $$G_S(\gamma) < G_S(\varepsilon) < G_S(\beta) < G_S(\alpha) \tag{2.21}$$

The critical size for any A to B phase transformation is given by (Tuček et al, 2010):

$$d_c^{A,B} = -6V_m \frac{G_S(A) - G_S(B)}{\mu(A) - \mu(B)} \tag{2.22}$$

Therefore, an adequate particle size of Fe_2O_3 inside the silica matrix would lead to the formation for a nanocrystalline phase (Mchale et al., 2018).

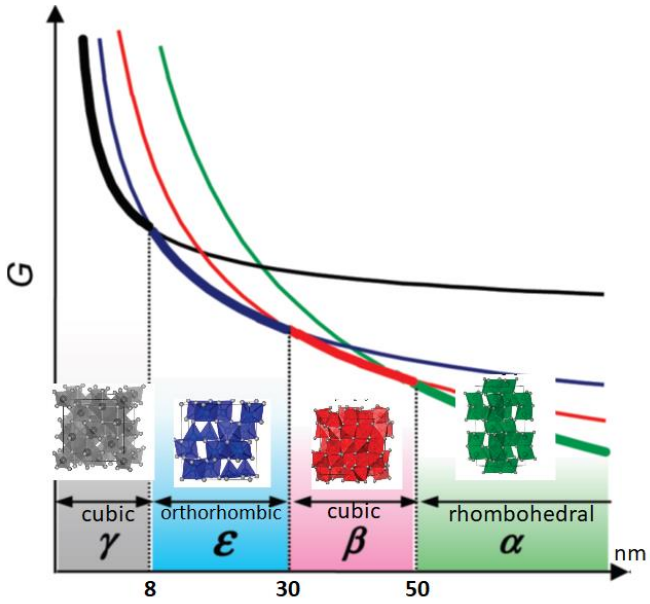

Fig. 2.19 Gibbs energy vs diameter curve for the four possible phases based on the conditions mentioned in the text. Adapted with permission from Sakurai 2009. Copyright (2009) American Chemical Society.

As mentioned in the previous sections, the growth of epitaxial thin films involves several intermediate steps that will determine the nature of the final product, in the case of epsilon ferrite, the first successful attempt of thin films was reported by Gich et al in 2010, achieving the stabilization of epsilon ferrite on STO (111) substrates. In that case, the lattice match between the film and substrate as well as the formation of multiple in-plane twins allowed the decrease of the (100) surface energies thanks to the formation of domain boundaries (Gich, 2010). STO, being characterized by a cubic crystal system with lattice parameter of 3.905 Å, the correspondence between the lattice epsilon ferrite and STO will result in an in-plane lattice parameters of a = $\sqrt{6}/_2\, a_{subs}$ and b= $\sqrt{3}/_2\, a_{subs}$ for the epsilon ferrite.

Another alternative substrate for the epitaxial growth of epsilon ferrite is YSZ with (100) orientation, another cubic crystal with lattice parameter of 5.12 Å, inspired by reports showing that isostructural compounds to epsilon ferrite and be grown on it and for its easy integration to silicon (Jun et al., 2001). Two epitaxial matches can be found between the YSZ substrate and the film grown on top of it. First, considering a parallel alignment of the a and b lattice parameters from the epsilon ferrite and the substrate; meanwhile a_ε and a_{YSZ} are relatively close, for b there is a relation achieved by a periodic translation symmetry of unit cells (tiling), $3b_\varepsilon = 5b_{YSZ}$. The second is observed in the diagonal of the epsilon ferrite unit cell where $2\,a_{YSZ} = \sqrt{a_\varepsilon^2 + b_\varepsilon^2}$ (Corbellini et al, 2017).

The relevancy of complex oxides in semiconductors, multiferroic and superconductors have motivated the recent studies of its interesting physicochemical properties mainly using HAADF imaging and spectroscopy, since the smallest change in their structure or chemical conditions can influence a huge response in their macroscopy behavior. Through improvements in resolution and aberration-correction quantitative analysis of the nanoscale structure of materials has been allowed, making possible the exact localization of atomic position and chemical states (Gázquez et al., 2016). They showed the effects of the Fe-O bonding conditions on the electronic and physical properties that oxide exhibits. Reported variations in the O K-edge are due as consequence of octahedral and tetrahedral coordination symmetries while the Fe L-edge remains the same.

3 Experimental Procedures

3.1 Pulsed Laser Deposition

Among several techniques for thin film synthesis, physical deposition methods are widely used due to their ability to produce high quality films. One of these methods is called Pulsed Laser Deposition, which basically consists in an ablation laser, precursor target and a substrate inside a chamber (Fig. 3.1) with different environment conditions (Oka & Fukumura, 2017). A typical deposition process can be described as follows:

- The excimer laser hits a ceramic pellet target for short periods of time repeatedly, the stability of is type of laser helps to the deposition of good oxide films (Singh & Narayan, 1990).
- Once the target is ablated this is heated rapidly, and a plasma plume is formed with species including electrons and ion clusters.
- The formed plasma is then propagated to the substrate where the film deposition occurs. Directional propagation contributes to a flux of almost same chemical composition from the target.

Environment conditions in PLD chambers are flexible and one can use a wide range of gas pressures, where collisions between gas molecules and growth species help to reduce their kinetic energy. The substrate can also be heated up for high temperature deposition (Oka & Fukumura,2017). The whole deposition process makes PLD a good method for oxide and complex material deposition, allowing the growth of multilayer structures and control of atomic arrangement of the films (Lowndes, Geohegan, Puretzky, & Norton, 2012).

The samples analyzed in this thesis were grown at Centre Energie, Matériaux et Télécommunications, INRS by Mr. Luca Corbellini using a Kr excimer laser with wavelength of 248 nm, pulse duration of approximately 22 ns and a frequency of 5 Hz. YSZ (100) and STO (111) miscut substrates were prepared by heating them at 800 °C in 75 mTorr Oxygen environment and placed at 5.5 cm distance from the target which contained a mixture of amorphous Fe_2O_3 polycrystalline hematite reported by Corbellini 2017

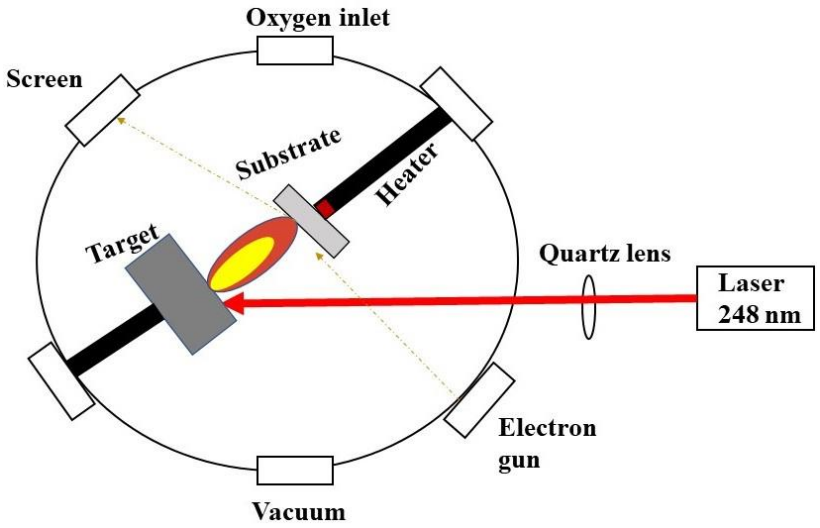

Fig. 3.1 PLD system schematic.

3.2 TEM sample preparation

The process of thinning a film until reaching electron transparency to achieve the best results in TEM analysis requires a series of complex steps and can be done by distinct methods, in the case of complex oxide thin films Focused Ion Beam (FIB) sample preparation is a very precise method and makes possible to handle with very small and thin samples, and is compatible with almost any kind of material although, it can be considered as an expensive technique.

3.2.1 Description of the instrument.

A vacuum system and chamber, a liquid metal source, an ion column and gas system are the main component of the FIB instrument (Fig. 3.2). For a dual FIB/SEM system, usually the FIB column is mounted with some angle respect to vertical (approx. 52 °). The vacuum chamber consists in three regions; the first for the ion source and column (10^{-8} torr), for the sample (10^{-6} torr) and a third for the detectors.

A FIB column typically is mounted inside a SEM. The ion beam is used for material removal and for electronic or ionic imaging to check ion milling process. The equipment also includes metal and carbon evaporation sources to deposit protective films on the specimen. Metal or carbon layer is deposited on the specimen (approx. 1 micron thick)

before the ion milling process for protection, usually helped by chemical vaporization of an organometallic gas.

The liquid metal ion source consists of a Gallium reservoir in contact with a Tungsten needle responsible to create Gallium ions that are manipulated by a set of lenses inside an ion column. These ions reach a stage where the sample is mounted, such stage has 5-axis movement to get a precise location of sites. There are detectors for collect secondary electron and secondary ion, the presence of gas sources on FIB allows the use of CVD and Electron beam-induced deposition to decompose gas molecules and deposit in the sample.

Ion emission in FIB is produced by putting in contact liquid Gallium with a Tungsten needle and applying a high field, approx. 10^8 V/cm, to create a sharp cone of Ga with a radius of 5-10 nm. Then, ions are emitted because of field ionization and they are accelerated down the column with an accelerating voltage that can vary from 5 and 50 keV (Giannuzzi & Stevie, 2005). The position of the beam is controlled by deflector plates. Ga ions penetrate the sample and create trenches on the surface generating ejection of particles and implantation of ions. Ga ions can also be implanted into the sample in a depth of approx. 20 nm (Giannuzzi & Stevie, 1999).

3.2.2 Cross-sectioning.

The purpose of using FIB for sample preparation is to create high quality cross sections in samples. Before cross-sectioning, it is necessary an initial preparation of the sample. This method is use for a wide variety of materials, including ferroic oxides (Mundy et al., 2016) a slice can be obtaining by cutting material directly from the bulk, with no pre-thinning needed (Overwijk, Heuvel, & Lieuwma, 2001).

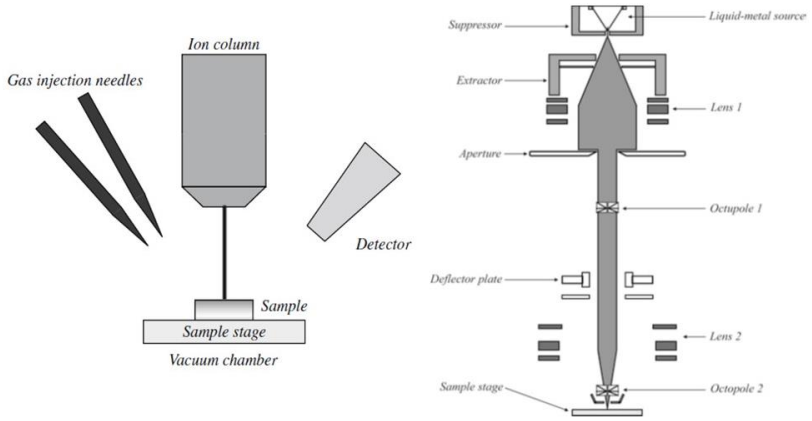

Fig. 3.2 FIB chamber layout. Republished with permission from Ayache et al, 2010; permission conveyed through Copyright Clearance Center, Inc.

Before starting any milling process, a carbon deposition is done to protect the surface of the film and also to improve the viewing in the TEM and a further Tungsten deposition is also carried out. Overwijk et al (2001), stated an accelerating voltage of 30 keV focused on a spot diameter between 0.005 and 1 microns varying the current from 13 pA to 1.2 nA. A staircase shaped ion milling is carried out on both sides of a previous selected area with different current values (45, 27, 14, 6.5) nA, then the specimen is tilted by 45° to cut the TEM specimen from the surrounding material (Fig. 3.3). Assisted for a tungsten needle with micrometer controls, the slice is removed from the bulk material and is adhered to the TEM grid for further micromachining.

After ion mill the specimen (20-30 kV) an internal extraction is carried out to create two trenches on the surface, and a low voltage (1-2 kV) thinning to minimize damage, using a

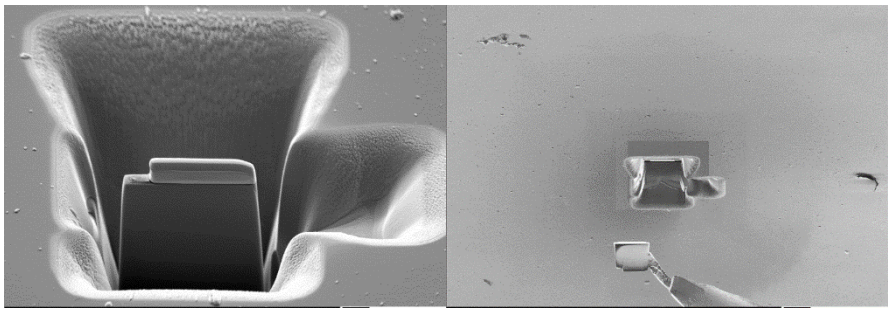

Fig. 3.3 Staircase shaped milling.

micromanipulator weld a thin slice (100 nm thick) to a TEM holder via electron beam-induced deposition (Fig. 3.4). After, tilting the sample at a 54^{o} and using a low voltage ion milling, both surfaces are cleaned. The target area is covered before the ion milling process and different steps of ion milling are carried out using (300, 150, 80) pA. Finally, a low-current milling is done using 10 kV and 80 pA (Fig. 3.5).

Lift-out sample preparation is an attractive technique for industry when TEM analysis is required because offers a quick specimen preparation with no previous treatment needed as well as limited time exposure and the ability to obtain a thin slice without damaging the rest of the material. According to the personnel from the Canadian Centre for Electron Microscopy, the traditional "lift-out" is the most used technique for TEM sample preparation in the institution. The emission of secondary electrons from the back surface of the sample can be used as reference when the lamella is thin enough for TEM analysis. If required, an Argon cold milling cleaning step can be done after.

Fig 3.4. Top: Welding process for internal method. Bottom: Final TEM lamella.

3.3 Preliminary TEM observation

Throughout the studies of these epitaxial thin films, a variety of microscopy techniques were used taking advantage of distinctive features that each one could offer. At first,

samples were looked in a Philips CM12 operated at 120 kV with a LaB_6 filament, used mainly for pre-inspecting the sample quality, low-magnification imaging and electron diffraction analysis. Once a sample was prepared by FIB and mounted in a TEM grid, a preliminary observation is this microscope was carried out; bright field imaging was helpful to visualize the growth of epsilon ferrite on both substrates, thickness and shape of the film. Also, dark-field imaging was also included to see possible grain orientations.

Fig. 3.5 Philips CM12 equipment.

The determination of the zone axis from the substrates was obtained by comparing the acquired diffraction patterns (Fig. 3.5) and a simulated diffraction pattern using the software JEMS (Stadelmann, 1987) The results from the measured and simulated g vectors are displayed in Table 3.1, showing also the estimated error for each one. Sources of error that could be mentioned are camera length calibration, drifting during acquisition or even sample related such as strained structures.

Table 3.1 Measured and simulated g vectors for the main reflections of the YSZ (100) and STO (111) substrates.

hkl	**Measured (g)**	**Simulated (g)**	**Error**
Zone axis: [010] YSZ			
200	3.83	3.87	$\pm$0.01
002	3.83	3.87	$\pm$0.01
Zone axis: [112] STO			
111	3.59	3.62	$\pm$0.008
-110	4.39	4.43	$\pm$0.009

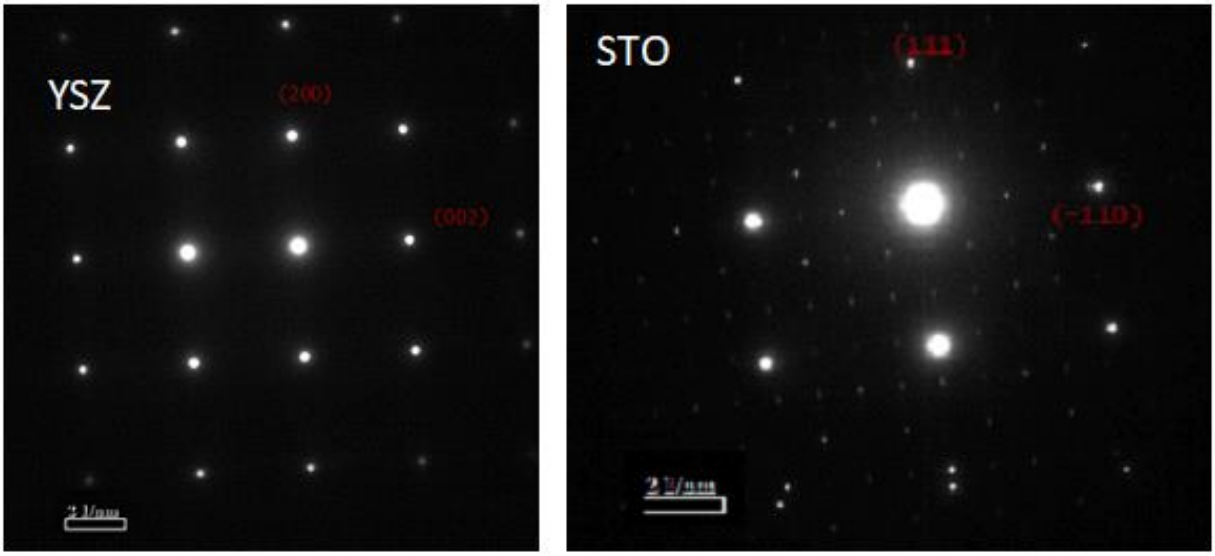

Fig 3.6 Acquired SAED patterns for YSZ and STO substrates, the latest also shows the film reflections as minor bright spots.

Moreover, low magnification images from the samples grown on YSZ substrate show an overview of the quality of the samples, the presence of columnar growth and a buffer layer in the film/substrate interface. In a similar way, for the STO samples, the presence of columnar-like growth is noticed, and a smaller buffer layer could be also considered to appear right at the interface (Fig. 3.6). Using distinct apertures, it is possible to obtain a selected area of 100 nm, SAED analysis was carried out to obtain information about the crystallographic relationships between the substrate and the film; identification and calibration of substrate zone axis and quick overview of the sample quality was performed before using higher-resolution techniques.

The limitations of conventional TEM pushed the research focus towards the usage of high-resolution techniques. The size of the apertures existing in the Philips CM12 and mechanical issues related to shifting of the beam when switching between diffraction and imaging mode motivated the implementation of higher resolution techniques.

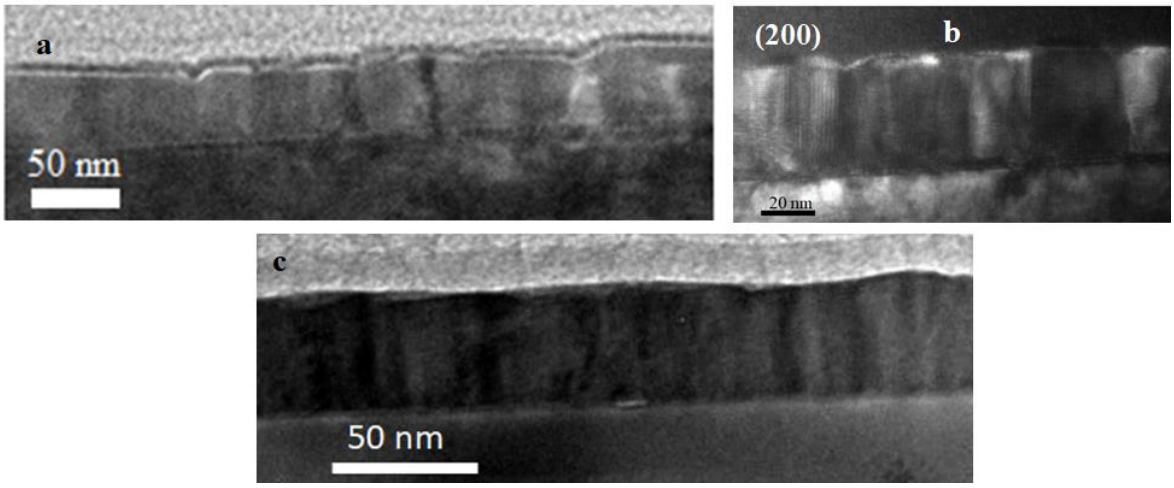

Fig. 3.7 Low magnification TEM image of epsilon ferrite deposited on YSZ (a) and DF image taken from the (200) reflection (b). Overview of epsilon ferrite on STO substrate.

3.4 STEM-EELS characterization

After the limitations previously mentioned and with the objective of obtaining a better understanding of the basic properties of the novel epsilon ferrite on perovskite substrate, most of the STEM analysis was carried out in a FEI Titan 80-300 cubed microscope equipped with a XFEG source, with the possibility to operate at 80, 200 and 300 keV, a CEOS hexapole image and probe corrector being able to obtain atomic resolution HRTEM and HAADF images as well as improved energy resolution for EELS measurement through the filtering of energy dispersed electrons by the excitation of the monochromator.

The fact that the microscope is located in an isolating and shielded enclosure reduces the effect of mechanical vibrations and electromagnetic interferences, giving a higher stability when performing experimental sessions. The usage of monochromator, a Wien filter located right below the electron gun, produces an electromagnetic field that deflects the entering electrons into a dispersed line where a selecting slit allows the selection of specific energy electrons allowing to reach an energy resolution of around 0.1 eV for EELS measurements. All these factors contributed to the simultaneous acquisition of high-resolution images and EELS spectra for unveiling the atomic structure of epitaxial iron oxide thin films.

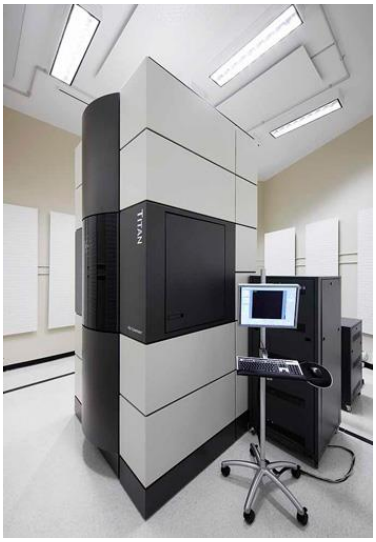

Fig. 3.8 FEI Titan 80-300 cubed used for STEM-EELS analysis.

The illumination system in the Titan microscope consists in six lenses named as follows: gun lenses, first, second and third condenser lens (C1, C2, C3), minicondenser lens (MC) and objective lens. The beam current and size of the probe are controlled by the gun lenses, C1 and C2 while the beam width and convergence angle parameters can be manipulated using C2 and C3. C3 also controls the illumination mode to use; parallel or focused beam, the minicondenser lens determines whether a micro or nanoprobe is used and finally the probe forming is carried out by the objective lens (Fig. 3.7). The main difference between setting TEM or STEM mode lies in the role of C3, for TEM the source is image on the front focal plane while in STEM the beam enters the objective lens roughly parallel.

Besides the acquisition of HAADF images, the microscope setup was used to perform NBED. The manipulation of C2 and C3 reduces the convergence angle of the beam to generate a small microprobe illumination and allows to obtain diffraction patterns from selected nanostructures and reduce the background from the surrounding material, in contrast with the conventional SAED method where the illumination spreads out over a large area of the sample ((J. M. Zuo et al., 2004)).

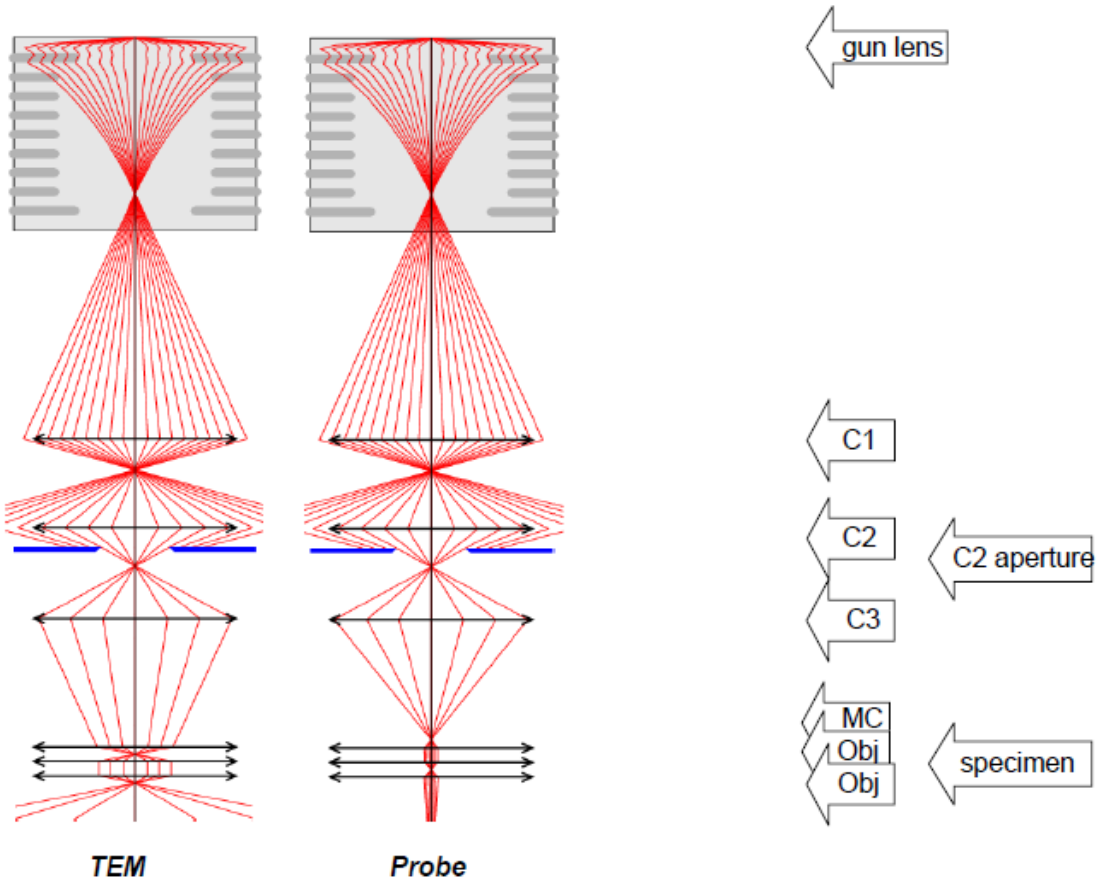

Fig. 3.9 Diagram of the two set ups of the condenser system for TEM and STEM (probe). The inset arrows indicate the position of each type of lenses. From FEI Titan Condenser manual.

3.4.1 The K2 detector

An additional feature to the described microscope setup is the direct detection K2 camera for imaging, EELS and diffraction mode electron detection. In contrast to the traditional indirect camera, where the incident electrons are converted to photons and sent to a sensitive camera by a series of fiber optic and lens arrangement, the direct counting mode has the speed to count individual high-energy incident electrons eliminating the induced noise related to gain variations and readout from the detectors. Now the acquisition of long energy ranges of EELS spectra is possible without jeopardizing the detection of sharp features in the fine structure even for low signal acquisitions.

The implementation of the direct counting mode for monochromated EELS measurements results in an energy resolution of 0.1 eV, obtained by width of the ZLP (Fig. 3.8a), reduced noise and point spread function (degree of blur from any point-like object) achieving an energy dispersion in the spectrometer of 0.1 eV/channel that ensures a spectrum with an energy range of 400 eV approximately (Longo, 2018). The improvement of the spectrum quality obtained by using the direct mode detection of the K2 allowed us to obtained a more detailed ELNES structure in the transition metal K-edge that helped to implement a better analysis of the chemical and bonding properties while for the data acquired with a CCD (indirect counting mode) certain features, such as splitting in the maximum of the peak, are not visible and such feature appears to be just as a shoulder (Fig. 3.8b) . A higher energy resolution would be needed to still use the CCD and be able to obtain the detailed information observed with the K2 detector. The implementation of these types of detectors has revolutionized the acquisition of TEM imaging and diffraction methods allowing to obtain less noisy data and the possibility to perform a STEM-based diffraction imaging.

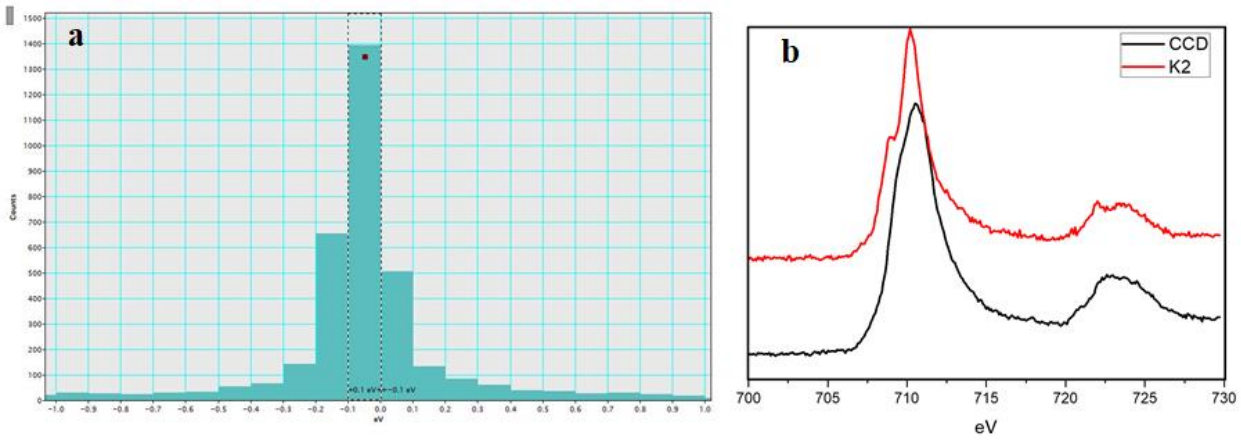

Fig. 3.10 ZLP acquired during using the K2 detector (a) and a comparison between the spectra acquired using K2 vs CCD detectors for the Fe L_{23} Edge in Fe_2O_3.

4 Structural and chemical analysis of ε-Fe_2O_3 thin films.

4.1 Introduction

The interesting magnetic properties reported for the metastable ε-Fe_2O_3 (Jin et al., 2004). have encouraged several attempts for the fabrication of this compound as thin films for its further integration into solid-state applications. This work has included the usage of some perovskite substrates (Martí Gich et al., 2014). YSZ being one of the most promising materials to produce a stable epsilon ferrite and allowing its integration into silicon-based devices (Thai et al., 2016). A direct precedent is the growth of epsilon ferrite on STO where the similar lattice parameters of the film and substrate lead to a strain stabilization of the phase, allowing the growth of this type of films (M. Gich et al., 2010). The STO crystal structure is represented by a Pm-3m space group with a lattice parameter of a_{STO} = 0.39 nm. The YSZ crystal structure is described as CaF_2-type, with Fm-3m space group and lattice parameter a_{YSZ} = 0.512 nm, meanwhile epsilon ferrite is characterized by an orthorhombic structure with space group $Pna2_1$ and a_ε = 0.519 nm, b_ε = 0.872 nm and c_ε = 0.968 nm, where the iron ions are arranged in three octahedral sites and one tetrahedral site (Fig. 4. 1).

In addition to the phase stabilization, effects of the substrate in interfacial phenomena such as misfit dislocations, segregations of dopants, strain and cation rearrangements have been suggested as consequences of the growth of thin films in YSZ (Fabbri, Pergolesi, & Traversa, 2010). The presence of ionic conductivity has been discussed in some references where the role of donor and acceptor doped oxides is improving the oxygen ion transport (Schmid et al., 2018; Song et al., 2014). Also, the strain-induced formation of oxygen vacancies in multiferroic thin films has been discussed to be concomitant with the reduction of transition metal valence state (Agrawal et al., 2016). STEM-EELS techniques have been used to explain the electronic configuration of complex oxides and correlate the findings with their outstanding properties (MacLaren & Ramasse, 2014). In this study, epitaxially grown ε-Fe_2O_3/YSZ (100) and STO (111) films with thickness of approximately 50 nm were studied using STEM to investigate the atomic structure of the interface, complemented with high spatial resolution EELS allowing the determination of oxidation states and additional bonding conditions.

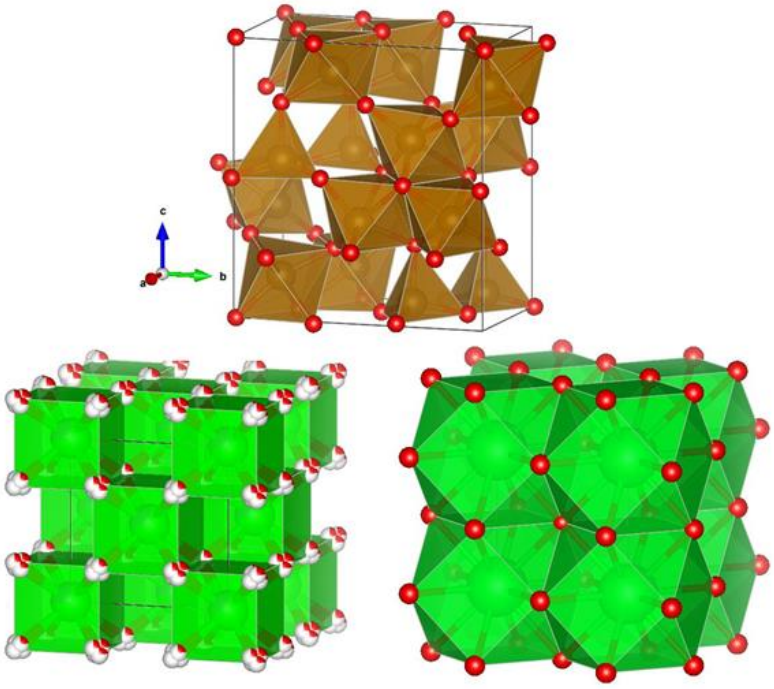

Fig. 4. 1. Atomic model of epsilon ferrite (top) and yttrium-stabilized zirconia (bottom-left) and strontium titanite (bottom-right). Image produced using VESTA (Momma & Izumi, 2011).

4.2 Experimental setup.

Epitaxial thin films with thickness between 46-50 nm were grown by PLD using a Kr excimer laser with wavelength of 248 nm, pulse duration of approximately 22 ns and a frequency of 5 Hz. The YSZ (100) and STO (111) substrates were prepared by heating them at 800 °C in 75 mTorr Oxygen environment and were placed at a 5.5 cm distance from the target which contained a mixture of amorphous Fe_2O_3 polycrystalline hematite. Cross-sectional TEM lamellas were prepared by FIB (Zeiss NVision 40) in a series of multiple milling stages until electron transparency is reached. STEM and EELS analysis was performed in a FEI Titan 80-300 HB (cubed) microscope at 200 kV equipped with a spherical aberration (Cs)- corrector and monochromator. EELS scans were acquired with a high-resolution energy-loss spectrometer (Gatan GIF model 966) with K2 direct electron detector, using a collection semi-angle of 19 mrad, GIF collection semi-angle of 20.7 mrad and camera length of 29.5 mm obtaining a 0.3 eV energy resolution and 0.1 eV/channel dispersion; the better point spread function and higher spectral quality of the K2 detector

leads to improved energy resolution conditions for better extraction of chemical state information. EELS characterization helped to obtain good chemical information of the film, including features such as elemental distribution, valence state and bonding conditions. Additional NBED patterns were acquired using microprobe STEM mode along the film in parallel and perpendicular to the film/substrate interface; a line scan of 1 micron with 200 patterns acquired generating one diffraction pattern each 8 nm.

4.3 Results

Combined STEM imaging and EELS analysis of iron oxide/YSZ and STO interfaces was used to study several interfacial configurations occurring at nanoscale level (Fig. 4. 2A). High resolution images were acquired along the [010] YSZ and [112] STO zone axis. Due to the difference in cation atomic number (Z), between the substrate (Z_{Sr} = 38, Z_{Zr} = 40) and film (Z_{Fe} = 26), HAADF images possess large differences of contrast that make the identification of features simpler.

4.3.1 STEM imaging and diffraction

The HAADF micrographs confirmed the existence of 5° miscut in the substrate surface with respect to the (100) plane, leading to steps which act as nucleation sites to promote preferential directions of epitaxial growth for out-of-plane twins corresponding to distinct epsilon ferrite projections. There are also darker regions suggesting, at the same time, possible deficiencies in density of materials in alternating position with the brighter clusters. An interfacial layer with a distinctive crystal structure within 4-5 nm from the ferrite/YSZ interface to the film is observed as a transition zone between the YSZ substrate and the film (Fig. 4. 2B). Nanobeam diffraction analysis carried out as a line scan, with the substrate oriented the [010] zone axis of YSZ, from the substrate towards the film, the reflections from the film and substrate indicate the presence of the $(200)_{\varepsilon}$|| $(200)_{YSZ}$ and $(010)_{\varepsilon}$||$(010)_{YSZ}$ orientation relationships of both diffractograms (Fig. 4. 2C), confirming a lattice matching in the lateral direction.

By applying a Fourier filter and image reconstruction of the interfacial layer; it is possible to identify a singular atomic arrangement which possess a spinel structure (Fig. 4. 2B). This

structure is commonly present in both γ-Fe_2O_3 and Fe_3O_4 phases and are difficult to differentiate just by inspection (Brundle, Chuang, & Wandelt, 1977). The Fe_3O_4, phase, also called magnetite, is known as a mixed valence compound which contains two Fe^{3+} and one Fe^{2+} ions resulting in an average oxidation state of 8/3. Its crystalline structure is characterized by a Fd-3m crystal space group; a cubic system where the oxygen atoms appear in a close-packed lattice with Fe^{2+} and Fe^{3+} occupying tetrahedral and octahedral sites respectively (Fig. 4. 3).

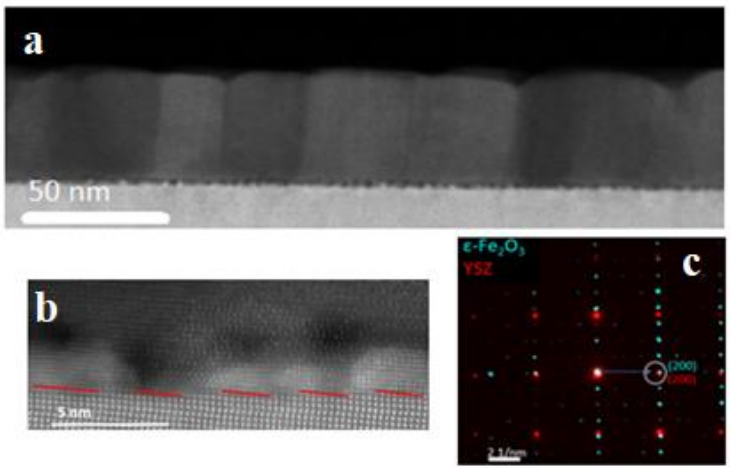

Fig. 4. 2. A) STEM image along [010] YSZ zone axis showing two main projection and film/substrate interface. B) Zoomed image of the film/substrate interface showing the presence of atomic steps and nucleation sites. C) Overlapped NBD patterns of substrate and film showing epitaxial relationships.

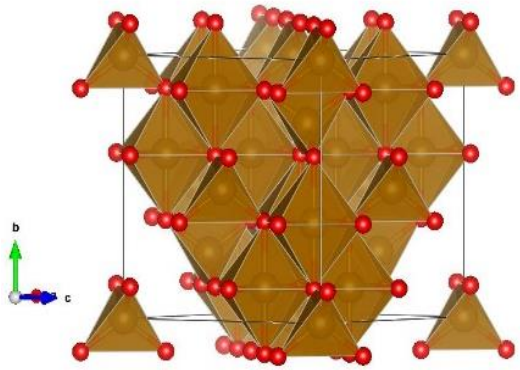

Fig. 4. 3 Atomic model for magnetite, with Fe^{2+} in tetrahedral sites in the corners and Fe^{3+} occupying octahedral sites. Image produced using VESTA (Momma & Izumi, 2011).

The polycrystalline nature of the film, revealed by the long-range contrast difference in DF and STEM images, was studied through NBD pattern acquisition, using STEM microprobe allowed the identification of specific grain orientations within a small area. Due to the small size of the observed domains, conventional diffraction techniques were not useful to identify the existing orientations. Along the lateral direction of film, the formation of domains can be found: [100], [010] rotated by 90° with respect to the b axis and both with their c-axis oriented with the growth direction of the film are shown in Fig. 4. 4. In addition, the presence of magnetite (highlighted in red) as mentioned in the previous paragraph, is noticed. A zoomed-in micrograph showing two well defined features from the [100] and [010] domain orientations was used to study the lattice matching between these two domains (Fig. 4. 5), where the presence of a boundary region between them is attributed to the difference in the atomic patterns from both orientations. The inverse FFT image obtained from the (002) reflection reveals the presence of extra planes at the interface which can be associated to dislocations possibly acting as a strain relaxation mechanism (Fig. 4. 5b).

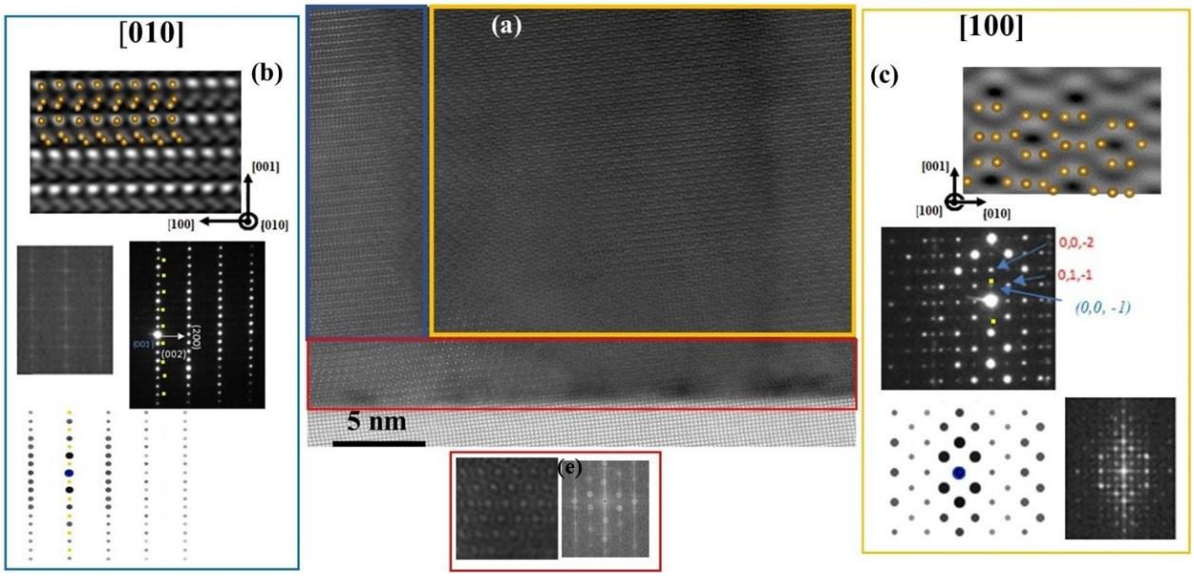

Fig. 4. 4. (a) High resolution STEM image of a the [010] (blue frame) and [100] (yellow frame) twin formation, including a spinel-like formation (red frame) in the film/substrate interface. FFT, Experimental nanobeam and simulated diffractograms for (b) [010] and (c) [100] projections confirming the mentioned orientations. FFT and image reconstruction of spinel structure (e).

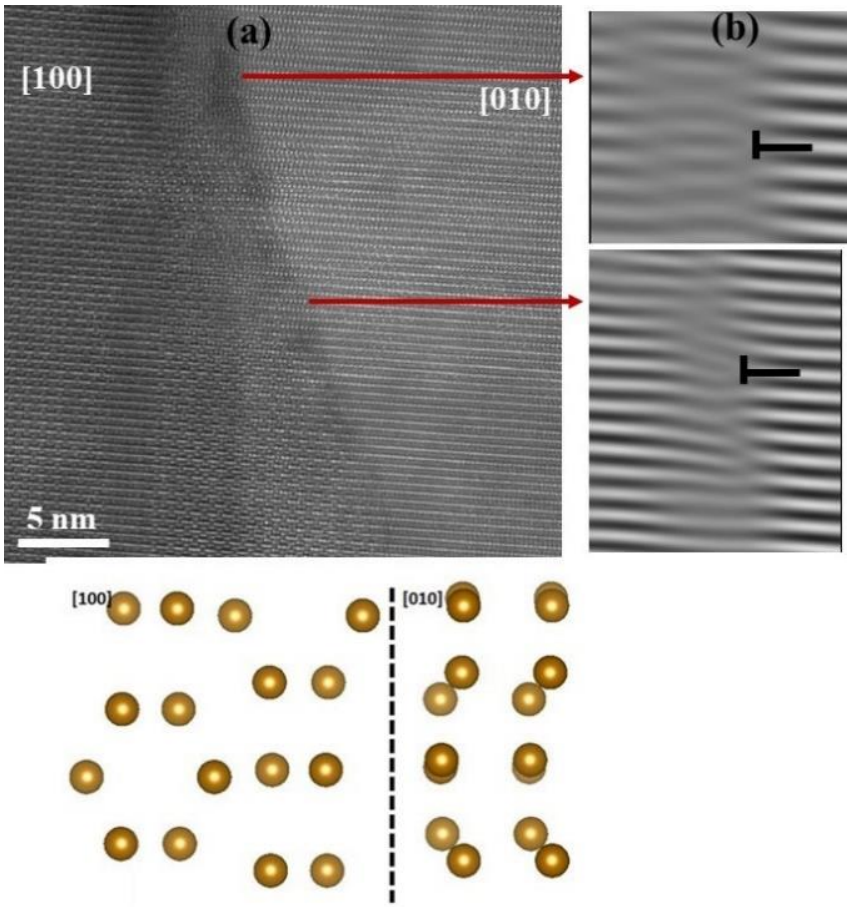

Fig. 4. 5 (a) High magnification HAADF image of the [100] and [010] boundary region. (b) Inverse FFT image acquired from the (002) reflection of (a). Bottom image: atomic models for [100] and [010].

Figure 4. 6 displays a domain boundary between the [-1-10] and [100] domain orientations, the acquired nanobeam diffraction patterns confirm that both have their [001] growth direction out of plane. In addition, the inverse FFT image shows that the lattice matching for that reflection is also reached through the generation of dislocations. However, in comparison to the boundary region observed in Fig. 4.5, a lower density of dislocations is observed, therefore the interface present in the {002} plane family of both domains could be catalogued as semicoherent.

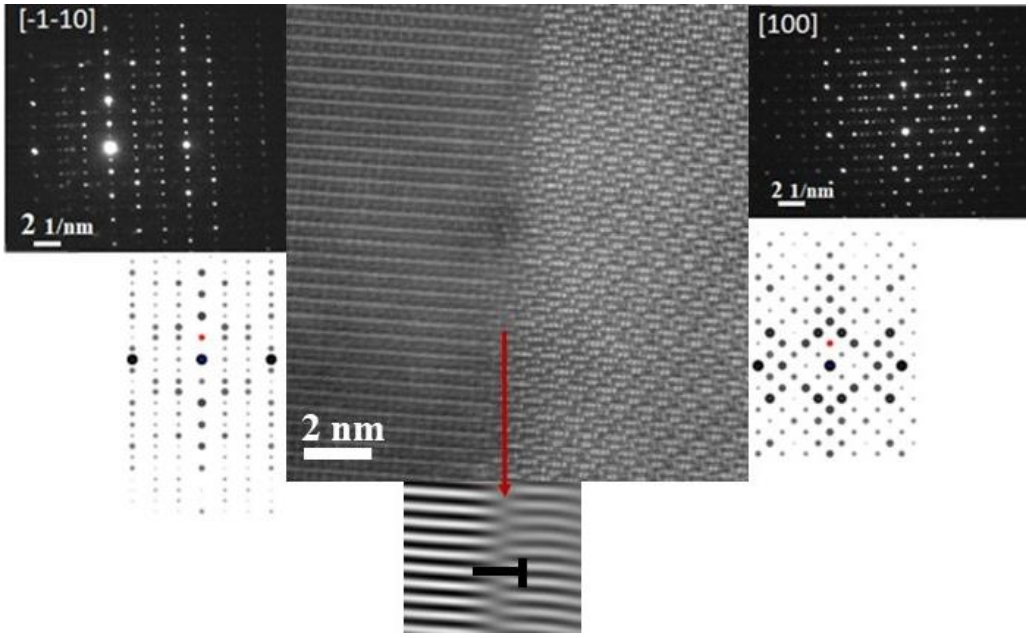

Fig. 4. 6 High resolution HAADF image of a semicoherent interface between the [-1-10] and [100] domains. The inverse FFT image was obtained from the (002) reflection from the image (red dot in simulated patterns) showing the presence of one dislocation.

Another sample, a 50 nm thick epsilon ferrite grown on STO (111) miscut substrates is displayed in Figure 4. 7a. In general terms this sample exhibits a higher crystalline quality, showing a smooth interface between the film and substrate, sharper than the films deposited on YSZ. The presence of miscuts also generates a tilting of 5° of the in-plane atomic rows with respect to the (111) growth direction of the substrate. As a consequence of the lattice mismatch between the film and substrates, some relaxation methods can be mentioned, one of these examples is the called *tilted growth.* In both cases (YSZ and STO), a tilting of 5° is present which matches with the degree of miscut present in the substrates. The mentioned mechanism can only relief a fraction from the total lattice mismatch, while the sample remain strained and can experiment peculiar phenomena as consequence of the remain strain (Popova et al, 2017) Moreover, a small dark region, one nanometer thick is noticed along the film/substrate interface. However, it is possible to determine that the present features in that region still belong to the epsilon ferrite and do not represent a secondary or parasitic phase (Fig. 4. 7b). The acquisition of diffraction patterns allowed the

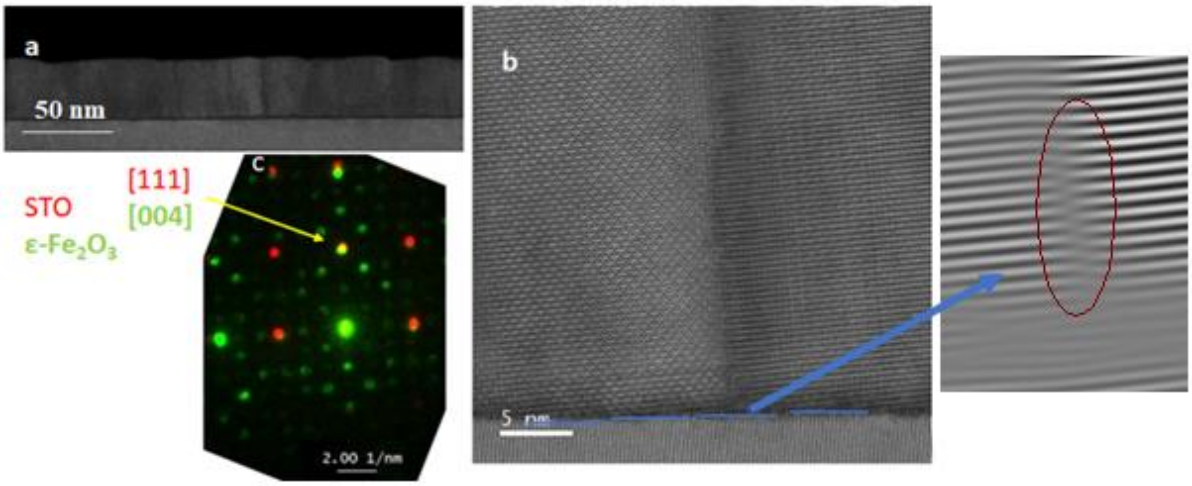

Fig. 4. 7 (a) STEM image of a 50 nm thick ferrite/STO (111) film. (b) Atomic-resolution HAADF micrograph from a two domain and substrate interface, the additional inverse FFT image shows the presence of dislocations within the domain boundary and the substrate interface. (c) Experimental diffraction patterns from the [100] ferrite and [112] STO zone axis.

identification of two in-plane twin formation which appear to correspond to the [100] and [-1-10] domain regions. In Figure 4. 7c, the superposition of acquired diffraction patterns shows the epitaxial relationships $(004)_{\varepsilon} \parallel (111)_{STO}$ and $(100)_{\varepsilon} \parallel (112)_{STO}$, where the (004) corresponds to the second order reflection of the ferrite growth direction.

Additional defects that can be found in the ferrite/YSZ sample is the presence of out-of-phase boundaries (OPB) seen as a shift of a fraction of the unit cell along the c-axis, a specific case of these defects is the called antiphase boundaries (APB), where the mentioned shifting is equal to half of the unit cell. Small translational jumps in the atomic rows of the film can be noted in Figure 4. 8, where the red and yellow insets are zoomed-in images within a 9 nm from the interface and from a grain boundary respectively, the white arrow lines are used as reference to indicate the displacement of the atomic rows. Moreover, a HAADF image from the ferrite/STO sample (Fig. 4. 9a) shows the presence of misoriented domains. Using an inverse FFT filter, applying a mask on the main reflections it was possible to reconstruct the most part of the image (Fig. 4. 9b), showing a domain growth separated by boundary regions (blue inset) along the (111) direction.

Moreover, the inset shows the translational shift highlighted by the blue and yellow arrows, showing the presence of APBs.

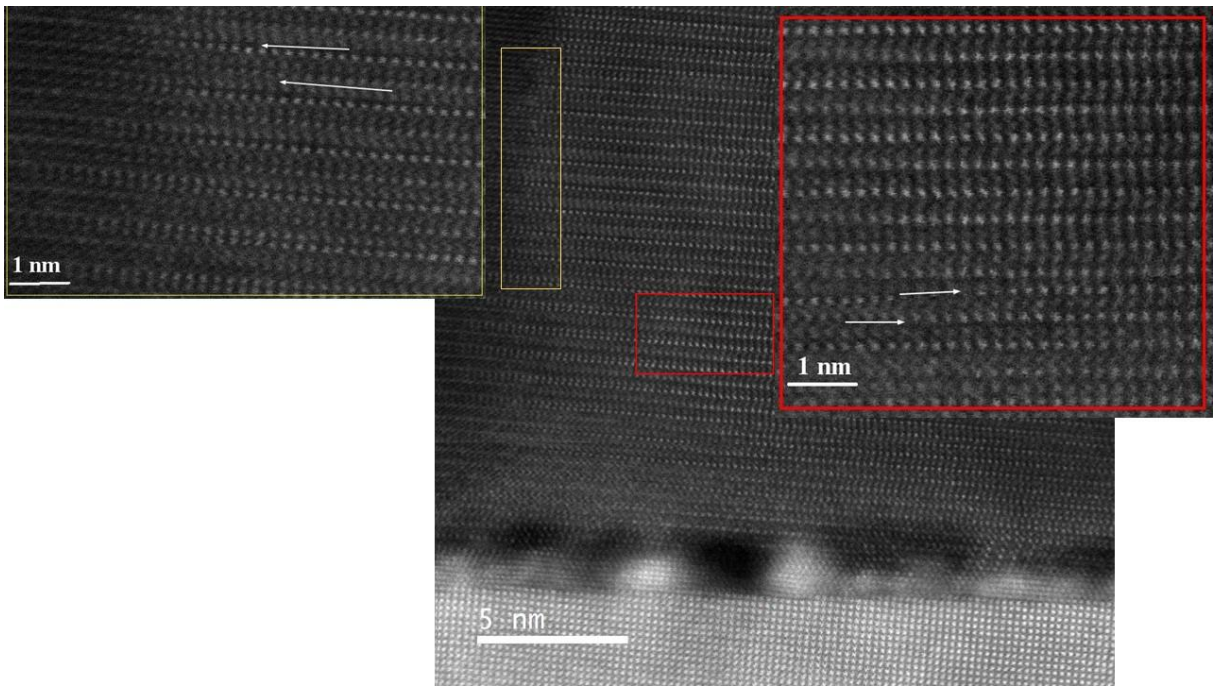

Fig. 4. 8 HAADF image of the [010] ZA of epsilon ferrite/YSZ showing the presence of OPB.

The effects of these translational anomalies in the atomic arrangement have been pointed by several authors mentioning their impact in the magnetic behavior of multiple oxide films. A high density of APBs is responsible for an observed decrease in the saturation magnetization since a modification in the bonding conditions is generated inducing a new superexchange interaction between the B-sites (Hibma et al., 1999) by inducing a high angle antiferromagnetic bond between the cation ions (Nedelkoski et al., 2017). Due to the nature of the defects and since APBs are a specific case of OPBs, their effects on the ionic magnetic interaction are expected to be similar and have a considerable impact in the final magnetic response of the sample. In addition, the presence of APBs in epsilon ferrite films is believed to be a direct consequence of the deposition on miscut substrates, whose main purpose was the reduction of twins.

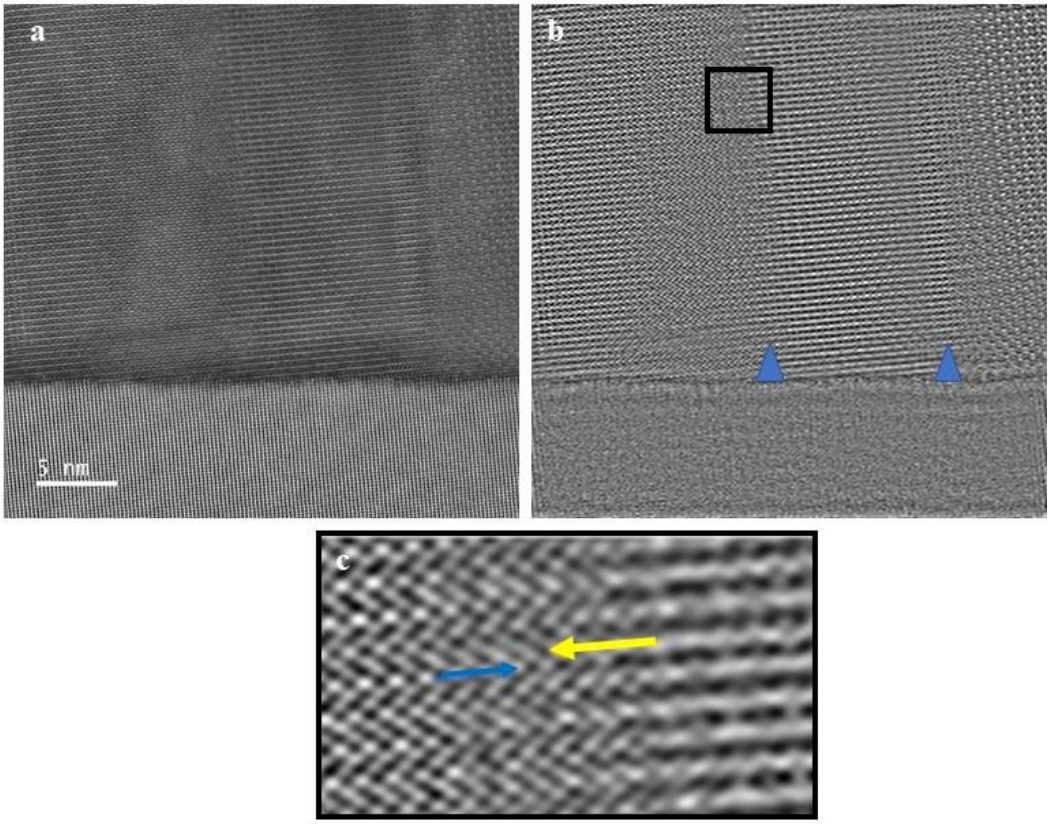

Fig. 4. 9 HAADF image of the ferrite/STO viewed from the $[112]_{STO}$ ZA (a). Inverse FFT image displaying the presence of domains separated by a boundary region (b) the inset represents a zoomed image from the domain boundary, the blue and yellow arrows represent the main atomic rows.

Nevertheless, the continued presence of in-plane twins plus OPBs are mentioned to contribute to hinder the domain wall motion and modify the anisotropy of a material (Rečnik, Nyir-Kósa, Dódony, & Pósfai, 2013). Popova et al (2017) have also found that the difference in out-of-plane lattice parameter of thin films varies with the thickness of the deposited film, having a direct implication on the saturation magnetization of magnetic films. Moreover, low dimensionality effects (J. Cao & Wu, 2011), changes in lattice parameters and bonding conditions between the metal and oxygen atoms induced by strain effects play an important role in the decrease of the expected magnetization; the main reason is due the appearance of Jahn-Teller distortion that generates a change in the ionic radius of the cation sites (Sandiumenge et al., 2013).

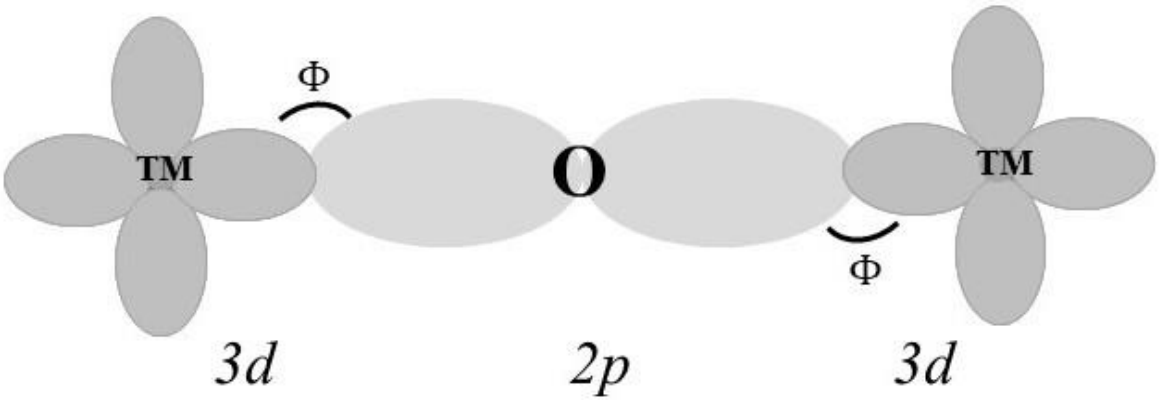

Fig. 4. 10 Superexchange bond representation. Adapted from Coey, 2009.

Changes in the bonding angle condition, as mentioned earlier in the text, could lead to a 120-180-degree angle between the 3d and 2p orbitals (Fig. 4. 10), resulting in a strong antiferromagnetic exchange.

The presence of surface steps represents a way to promote a step-flow growth of the deposited material on the selected substrates this with the purpose of reducing the formation of in-plane twin formation. Surface-step-terrace allows to tune the interfacial strain through the lattice matching between the film and substrate accommodating the film unit cells in step terraces (Yao et al., 2016). In the case of the sample deposited on YSZ (100), the three identified domain orientations [010], [100] and [-1-10] certainly represent a reduction in the twin formation as can be seen from previous reports where due to the symmetry present in the substrate, the formation of 12 twins can be possible (M. Gich et al., 2006). However, this configuration still results in three atomic arrangements with their a-axis in-plane pointing towards opposite directions, taking into account that the a-axis of the unit cell has been identified as the easy magnetic axis. The fact that there are specific domain orientations with different alignments of their magnetic easy axis hinders the achievement of the expected high magnetization value. Samples grown on STO (111) showed a better crystal quality in general terms, where a reduction of twin formation is also observed. However, various types of defect can be detected as consequence of the surface step present on the substrate. Such types of defects have been found to be edge dislocations that could act as strain-relief mechanism. The presence of edge dislocations between the in-plane

domain orientations as well as the appearance of misfit dislocations and possible secondary phases in the interface of the epsilon ferrite in both substrates, has been proposed to be strain relaxation mechanisms. For this reason, further quantification analysis will be discussed to support this idea.

4.3.2 GPA analysis.

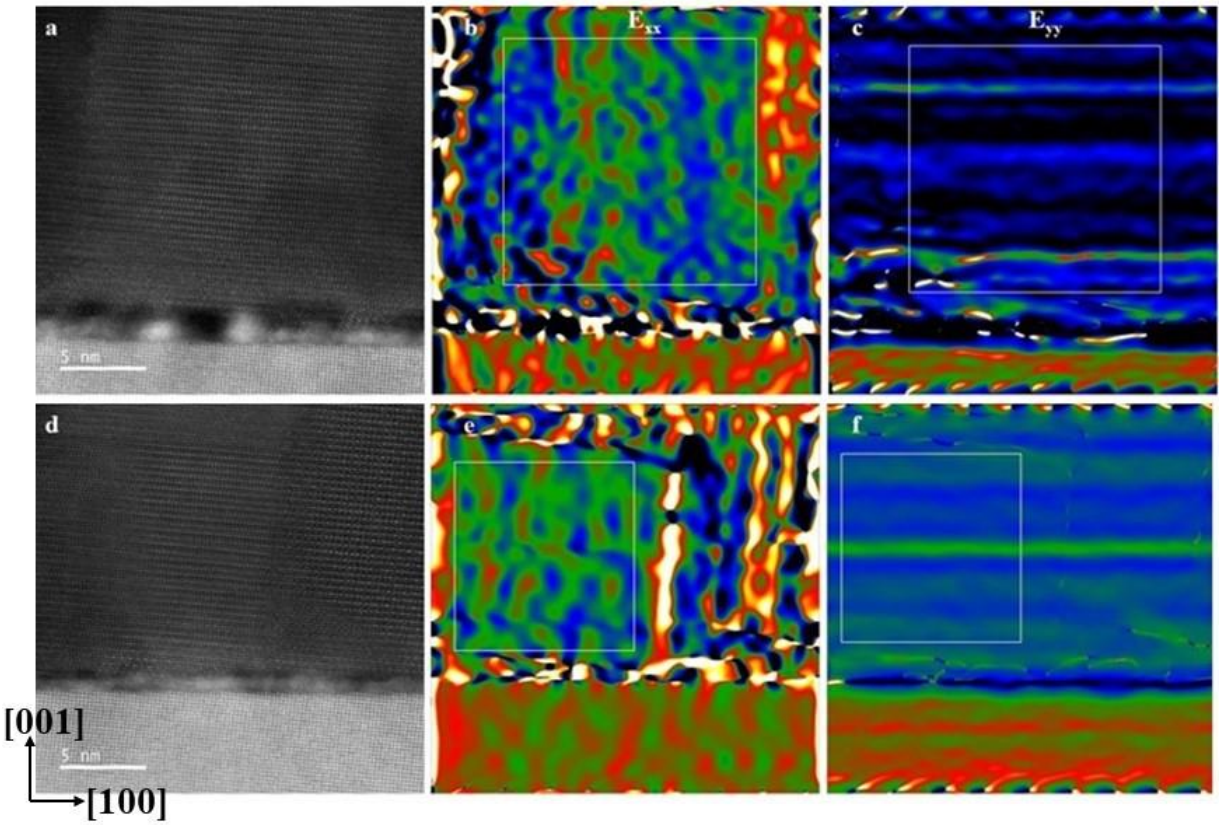

Fig. 4. 11. Atomic resolution STEM image of the ε-Fe2O3/YSZ thin film for the [010] domain (a) and [010] and [-1-10] boundary region of the film (d). (b,c) In-plane strain map and (c,d) Out-of-plane strain map calculated by GPA.

The quantification of the total amount of strain present in the epitaxial thin films was performed by geometrical phase analysis (GPA) applied to HAADF-STEM images corresponding to two distinct regions of the film: the [010] domain (Fig. 4. 11a-c) and a boundary region between [010] and [-1-10] domains (Fig. 4. 11d-f), allowing the calculation of a displacement field with respect to a reference (Hytch et al, 1998), in this

case the substrate. From the E_{xx} map, the resultant strain obtained as the statistical mean along the white square in the maps indicates a 1.1% (Standard Deviation = 0.5%) and 1.3% (Standard Deviation = 0.7%) (from Figures 4. 11b and e respectively) compressive strain compared with the substrate. Subsequently, the calculation of the expected lattice parameter of the epsilon ferrite was obtained using the strain formula:

$$E_{xx} = \frac{a_{roi} - a_{ref}}{a_{ref}} \tag{4.1}$$

Where a_{roi} represents the lattice parameter of ε-Fe2O3 film and a_{ref} the YSZ substrate. Solving for a_{roi} gives a lattice parameter of 0.5064 for pure [010] orientation and 0.5053 nm for [010] close to the boundary region. A final comparison is done with the unstrained values of the bulk phases previously mentioned, where the strain calculation results in a compressive in-plane strain of 2.42% and 2.63%. Meanwhile the out-of-plane strain map (E_{yy}), gives information about the c-parameter of the film resulting in a measured compressive strain of 8% (Standard Deviation = 1.98%) and 8.21% (Standard Deviation = 1.35%) (for 8 c and f) with respect to the substrate reference, leading to a lattice parameter of 0.942 and 0.94 nm, producing a compressed strain of 0.6 – 0.8 % compared with the reported lattice constant of 0.948 nm which can be considered as a relaxed structure. However, the large uncertainty caused by a large standard deviation suggest a large calculation error induced by scan distortions from the image acquisition. Moreover, the identified bright clusters at the interface appear to be zones with the highest compressive strain while in the dark zones the maximum of the tensile strain can be found.

Further analysis of the ε-Fe_2O_3/STO systems was carried out for a HAADF-STEM image along the [112] zone axis of the substrate and the [100] domain of the film (Fig. 4. 12). A value of 6.12% tensile strain is obtained from the in-plane map, with a Standard Deviation of 1.28%. The correspondence for the $[100]_{\varepsilon} \parallel [121]_{STO}$ epitaxial match is given by the in-plane relationships $a_{\varepsilon} = {\sqrt{6}}/{2}\, a_{STO}$ and $b_{\varepsilon} = {3\sqrt{2}}/{2}\, a_{STO}$. Therefore, the strain equation showed before is represented by:

$$E_{xx} = \frac{2a_{roi} - \sqrt{6}\, a_{ref}}{\sqrt{6}\, a_{ref}} \qquad (4.2)$$

Solving for a_{roi}, gives a new a-lattice parameter of 0.5068 nm, resulting in a final compressive strain of 2.35%. Using the established relationship for b_{ε}, the strained b-lattice parameter is estimated as 0.878 nm and therefore exhibit a tensile strain of 0.69%. A decrease in the a-lattice parameter due to compressive in-plane strain is now evident for epsilon ferrite deposited in both YSZ and STO substrates and confirms a decrease in the a-lattice parameter. The a-axis, being the easy magnetic axis of the system will have a direct implication in the reduction of the coercive field of the sample as pointed out in the literature (Coey, 2009).

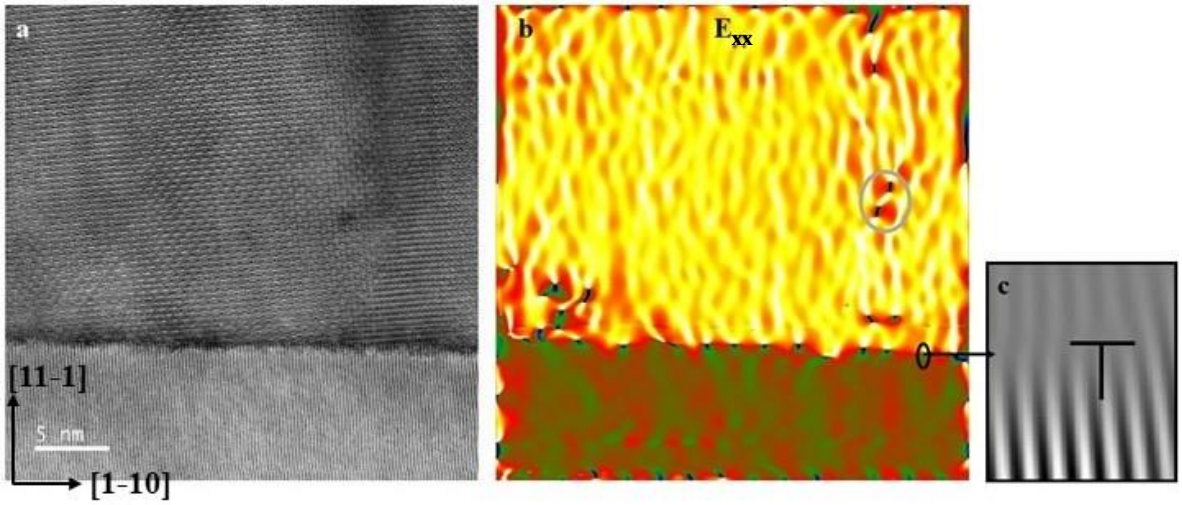

Fig. 4. 12. a) Atomic resolution STEM image of the ε-Fe2O3/STO thin film. (b) In-plane strain map. Bottom: Fourier filtered image showing the presence of extra planes in the interface of the film/STO.

Besides the quantification of in-plane strain, the obtained maps helped to visualize distinct distortions induced by the presence of defects. From the map displayed in Fig. 4. 12b, the identification of dark regions located at the interface of the ferrite/STO substrates suggest the idea of the presence of misfit dislocations, characterized as spots with high compressive strain accompanied by tensile strained zones in between them. This behavior arises from the difference in atomic spacing from the substrate and the film (Markov 2003), where STO

has larger value than the epsilon ferrite. The presence of these dislocations generates certain regions of the interface where both lattices register almost a perfect match while some regions will exhibit stripes showing the lack of registry between planes as displayed in Fig. 4. 12c, where a Fourier filter reconstruction of the HAADF image from the interface allows the visualization of an array of dislocations with the extra atomic planes with smaller atomic spacing (highlighted in black circles) whereas the region between them shows a good atomic matching. Moreover, the presence of high compressive strain in the film (marked as grey circles in Fig. 4. 12b) are attributed to the mentioned presence of edge dislocation between grains.

It is been reported that most epitaxial thin films tend to suffer compressive in-plane strain and exhibit a larger out-of-plane lattice parameter than their reported bulk value as a manner of compensation (Narayan & Larson, 2003). The presence of a periodic array of edge dislocations along the interface can be evidence of an alignment of unit cell on each terrace generated by the miscut substrate (Ma et al., 2013). However, in the case of the STO film, interfacial dislocations are not equally separated, indicating that the width of domains does not match the terrace dimensions.

In some cases, thin films with small lattice misfit can grow *pseudomorphically* and generate beside misfit dislocations, lattice distortions, buffer layers and secondary phases (Zhu et al., 2013). Also, the nucleation of misfit dislocations at surface steps has been proven to be a mechanism of strain relaxation (Pennycook et al, 2013). The influence of twin formation in iron oxides deposited on YSZ substrates (Gilks et al., 2016). has been established as one cause of the modification of the bonding condition of the Fe-O polyhedral. The formation of misfit dislocations as relaxation mechanism generates the loss of a Fe plane which is detected by EELS measurements as an increase in the valence state. The mentioned strain effects can also generate cation segregation in the interface of the film/substrate. An example of this has been studied for oxide films on alternate STO substrates, showing that depending on the preferred growth orientations, the strain relaxation will be realized through a set of mechanisms: going from the formation of defects to cation migration (Estradé et al., 2008).

In addition to the structural characterization previously described, a series of EELS measurements were carried out to study the chemistry of the interface and correlate the effects of strain with changes in the bonding conditions of the film/substrate interfaces. EELS studies were carried out across the substrate-film interface with the purpose of understanding the electronic structure behavior of the iron oxide growing on YSZ and possible origins of the interfacial layer. EELS line scans starting in the substrate continuing 20 nm into the film were acquired, showing the distribution of oxygen and iron in the film. EELS spectrum image datasets were acquired in a single range mode from 480 to 850 eV allowing us to obtain information about the O-K and Fe-L edges.

4.3.3 Iron L-edge

For analysis of the chemical state of the sample, the ELNES of the Fe L_{23} gives information that can used for the identification of valence states in certain compounds. According to the selection rules for possible transitions among quantum states, transitions from 2p to 3d and 4s orbitals are allowed for iron. However, the cross-section of both make the contribution to the L_{23} peak to be dominated by 3d orbital excitations (P. a. van Aken et al., 1998), meanwhile s-states allowed transitions only have a weak presence in the edge structure, mainly after the maximum of the L_{23} peaks (Abbate et al., 1992). On the other hand, the intensity of transitions is mostly related to unoccupied 3d states (van der Laan & Thole, 1991). Variations in oxidation state of a sample can be studied by measuring the ratio of the L_3 and L_2 portion of the L_{23} peak (the L_2/L_3) which varies with the d-band occupancy (Leapman et al, 1982).

Figure 4. 13 shows an EELS map in a selected region of interest between the substrate and the film, showing a relatively uniform distribution of iron along the film. However, close to the interface, a larger concentration of iron ions is seen. Quantification of the extracted signal from the EELS spectrum image was carried out using the method described by (Verbeeck & Van Aert, 2004) to find the corresponding Fe/O ratio. Right at the interface, where the concentration of Fe seems to be higher, the atomic composition for oxygen is estimated in 61.5% while iron is around 38.5 %. In the rest of the film, the oxygen distribution is approximated in 63% and 37% for iron. The demonstrated increase in atomic

fraction of iron can be attributed to the presence of magnetite, since it possesses more ionic iron sites in its unit cell; a higher concentration of ions in confined areas suggest the idea of a reduction in the iron valence state and rich areas of iron ions could be identified as nucleation sites. Also, the distribution of oxygen seems to be homogeneous around the film with possible deficiency sites at the interface. However, the EELS maps shown in Figure 4. 13 suggest that there are some regions at the ferrite/YSZ interface where the concentration of iron can reach values near to 85-90 % generating zones with oxygen deficiency that can be seen as black spots in the oxygen map.

For further analysis of the chemistry of the interface, a series of EELS spectra were acquired across the film as slices of the spectrum image of 10 nm width and 5 nm thick, from the ε-Fe_2O_3/YSZ interface toward the bulk, this with the purpose of covering the interfacial layer. Significant changes are observed in the $L_{2,3}$ edges at multiple distances from the film/substrate interface (Fig. 4. 13). Starting from the bulk (spectrum 1), the maximum of the L_3 transition is located at 710.2 eV showing a well resolved feature located 1.6 eV lower energy than the maximum point of the edge, this in agreement with the reported feature for the Fe^{3+} valence state due to crystal symmetry effects in octahedral sites (Chen et al, 2009). As the distance from the interface is reduced, a variation in the peak intensities is noticed, where a splitting in the L_3-edge appears, suggesting a reduction in the oxidation state of the sample. From spectra 2 to 5, a similar shape of the edge can be seen but the additional peak previously observed increases in intensity until it becomes a double -peak feature as shown in spectra 7 and 8. In these spectra, despite the mentioned double-peak feature, it can be notice that a shifting to lower energies is also occurring, while in spectra 9 and 10, the shifting is complete and now the maximum intensity is at ~ 708 eV. A shifting to lower energies in L_3 edges and the presence of more complex splitting is directly related to a transition from trivalent to divalent state (Chen et al, 2009).

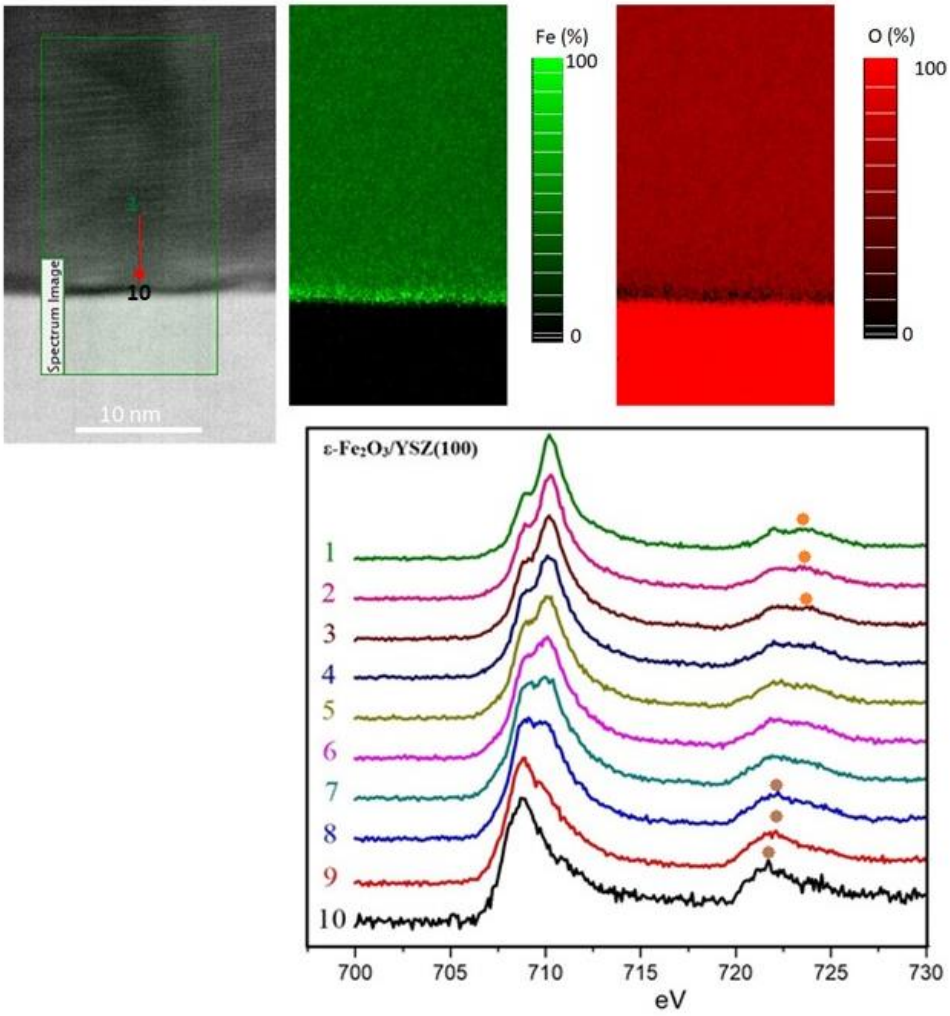

Fig. 4. 13. Top: EELS spectrum image from the region of interest showing the distribution map of iron (green) and oxygen (red) at the film/substrate interface.
Bottom: EELS spectra extracted from the spectrum image displayed in A. Starting from the interface (black) and acquiring a series across the film. Orange and brown dots represent the identified features for the L_3 edge discussed in the text

Following the procedure previously described, EELS spectra from the epsilon ferrite/STO interface toward the bulk were also acquired and are displayed in Figure 4. 14. In this case, the shape of the L_3 edge doesn't present any significant changes, suggesting a homogeneous composition of Fe^{3+} due to the shape of the edge similar to the bulk fine structure of the sample described in the previous paragraph; a large transition preceded by a prepeak feature

located at 1.6 eV lower energies. Moreover, the L_3 edge also has the similar two-peak feature located 12 eV higher energy from the L_3 ionization edge, (i.e. L_2 edge) showing the typical edge for a Fe^{3+} ionic distribution, commonly found in iron (III) oxides.

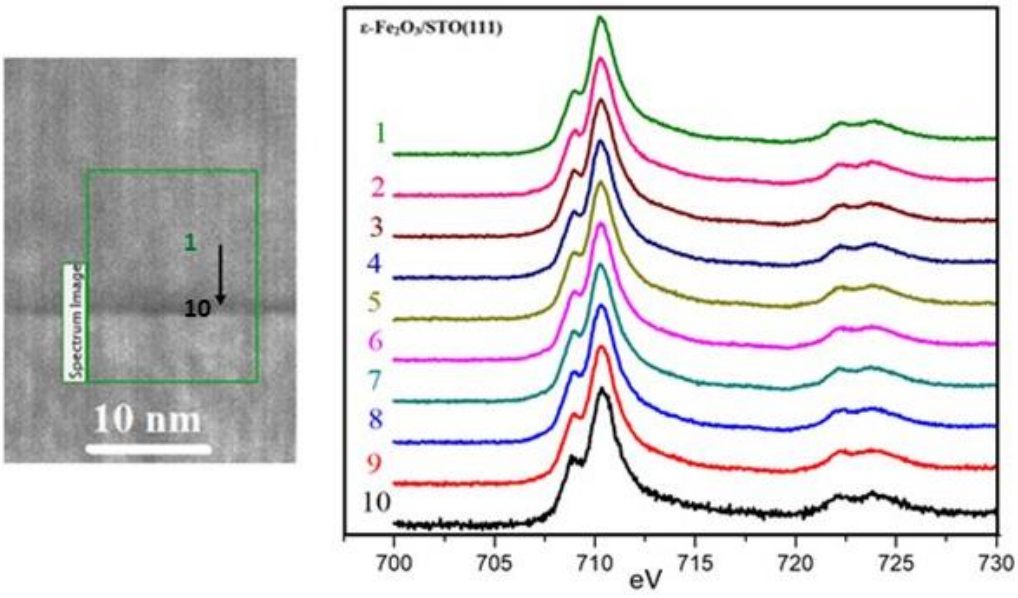

Fig. 4. 14 Left: EELS spectrum image from the ferrite/STO interface. Right: Acquired EELS spectra extracted from SI showed.

The strong changes observed in the near edge shape of the L_3 transition of the sample deposited on YSZ, represented by an evident shift towards lower energies of the maxima and the change in the shape in the EELS spectra confirm the idea of a multivalence Fe^{3+} and Fe^{2+} presence. Moreover, from the L_2 edge from spectra 1-3 a post peak can be identified (orange dots in Fig. 4. 13 bottom panel) while in spectra 7-10 this feature is totally changed to a single peak. According to quantitative studies about iron oxidation states (van Aken, 2002), Fe^{2+} EELS spectra show a sharp peak at 707.8 eV with a small shoulder at 710.5 eV meanwhile Fe^{3+} is characterized by a maximum around 709.5 eV. The existence of a tetrahedral coordination site from the epsilon ferrite, originates from the presence of a weaker signal around 1.3 eV before the maximum, which cannot be seen in the pure iron (III) oxide references since there is no tetrahedral coordination in its lattice

(Tafto et al, 1982). A mixed-valence compound, such as magnetite, presents a series of features in the L_2 edge with different intensities in addition to a simple Lorentzian L_3 edge. However, the idea of multiple valence is strongly accepted and further quantitive analysis was performed to understand in a better way the cation arrangement of the film.

With the purpose of obtaining information about localized changes in the fine structure observed for the sample deposited on YSZ, analyses of specific spots on the bulk part of the film and the interface were carried out. Besides the surface steps and dark regions at the interface, is possible to note bright features, crystallites between 1.5-2 nm in size, that are growing in the flat portions of the surface steps caused by the miscut. These islands appear to be the nucleation sites of new crystalline phases (Fig. 4. 15). From the line scan (yellow line in Figure 4. 15), one spectrum from the bulk of the film (red circle) and one from the interface (black circle) were used to compare the differences in the fine structure from the bulk and the interfacial layer of the film it is easy to identify a shifting to lower energies in the L_3 edge and changes in the resolved features from the L_2 edge. These changes also confirm the cation valence reduction phenomenon described before.

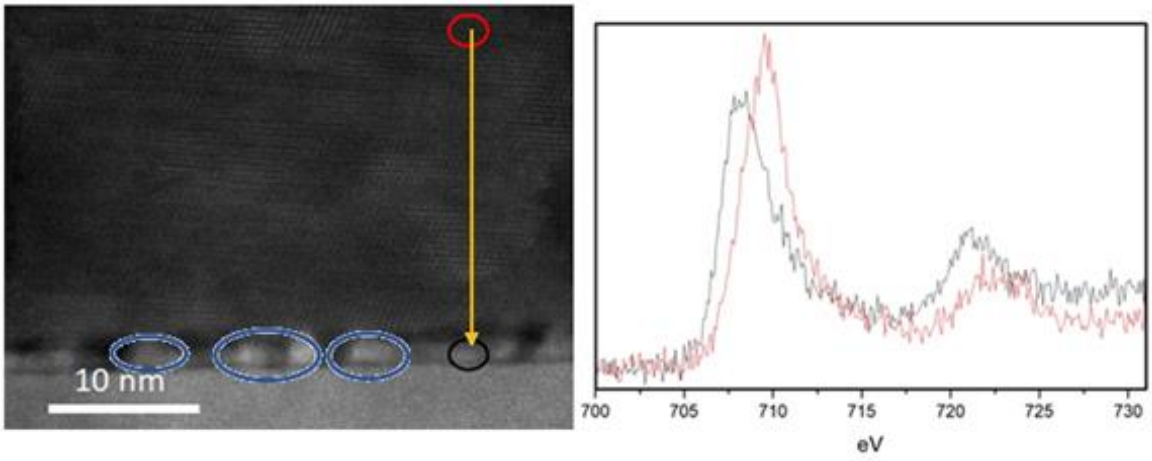

Fig. 4. 15 Left: TEM cross-section, showing the presence of a secondary crystal structure at the interface and nucleation sites (blue circles). The yellow arrow represents the EELS line scan acquired from the film to the interface. Right: EEL spectra acquired from the red and black insets.

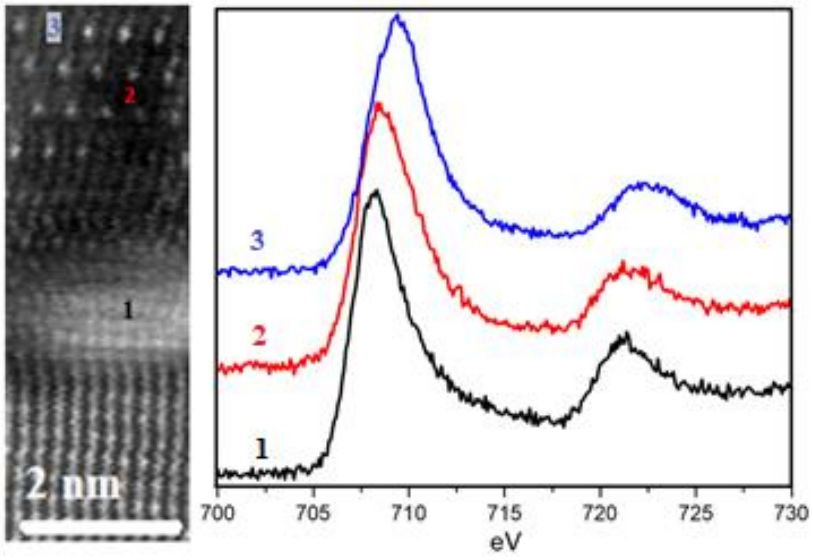

Fig. 4. 16 HAADF image of the ferrite/YSZ interface showing the presence of bright clusters, dark regions and spinel-like structure (left) and Fe L-edge of the regions marked in the HAADF micrograph (right).

A HAADF image from the interface, where the mentioned bright clusters and dark regions emerge in a 5 nm distance from the interface, is shown in Fig. 4. 16. The acquired EELS spectra for three different sites of the interface help us understand the difference between these three regions showing a similar shape for the L_{23} edge for bright and dark regions (named 1 and 2 respectively) while zone 3 (spinel-like structure) seems to have a small shift to higher energy in the maximum of the L_2 peak. This result confirms the presence of the mentioned magnetite in certain spots regions within 5 nm from the interface. However, the mentioned features in the other two spectra suggest a random presence of most likely Fe^{2+} ions with different coordination environment.

A chemical shift of 1.4 eV in the L_3 edge present in oxidation processes in addition to other features that found in the $L_{2,3}$ edge have motivated several studies with different approaches for a better understanding of the electronic transitions (Leapman et al, 1982). The single electron interpretation of spectra fails when explaining some of the features present in the Fe L-edge because of the strong hybridization of the 2p oxygen and 3d transition metal orbitals in cation sites, forcing us to consider a transition of the type $2p^6 3d^n$ to $2p^5 3d^{n+1}$,

where n = 5 for Fe^{+3} and n=6 for Fe^{+2}. Several factors should be considered as causes of the edge behavior including p-d, d-d, spin-orbit of the p-like hole, etc. The presence of spin-orbit coupling is revealed by the separation of approximately 10 eV between the two peaks of the edge (Colliex, Manoubi, & Ortiz, 1991). A charge-transfer model describes a $3d^{n+1}$ L configuration where a ground state 3d interacts with an electron from the oxygen 2p level and L is a ligand hole; the difference in energy between the ground state and the described state is called charge-transfer energy which generates different feature in the spectral shape. Spin-orbit interaction effects, with origin in the Fe 2p holes, generate a separation between the two present features in the iron L-edge with a distance between each other of approximately 13 eV (Colliex et al, 1991) which agrees with the measured distances from the maximum of the L_2 peak to the maximum of L_3. In the magnetite spectrum, the L_3 edge does not exhibit expressive features, due to non-zero density of states at the Fermi level in the 3d band and the presence of mixed valence generates a blurring spectrum (Crocombette, Pollak, Jollet, Thromat, & Gautier-Soyer, 1995).

The presence of multivalence state of transition metals in thin films has been reported for several cases; where oxygen vacancies, lattice expansion and formation of secondary phases are main sources of this phenomena (Turner et al., 2011). Moreover, a multiple linear least squares (MLLS) fitting methods was employed to identify the distribution of Fe^{2+} and Fe^{3+} along the observed areas, noticing an important increase concentration of Fe^{2+} right at the interface and a gradual decrease in the bulk part of the film while the presence of Fe^{3+} dominates the bulk part of the film and seems to be reduced at the interface.

With this method, the spectrum image was reconstructed by the weighted sum of two reference spectra from the sample (namely spectra 1 and 10 from Fig. 4. 13 bottom panel) and a reference background. The maps displayed in Fig. 4. 17 agree with the acquired EEL spectra from Fig. 4. 13 where the mixed valence polymorphs are represented by the double peak feature present in the L_3 edge which has been related to the present of multivalence iron ions within 7 nm from the interface in different coordination sites; mostly Fe^{3+} and Fe^{2+} in octahedral coordination and Fe^{3+} with tetrahedral symmetry (Garvie et al,1994).

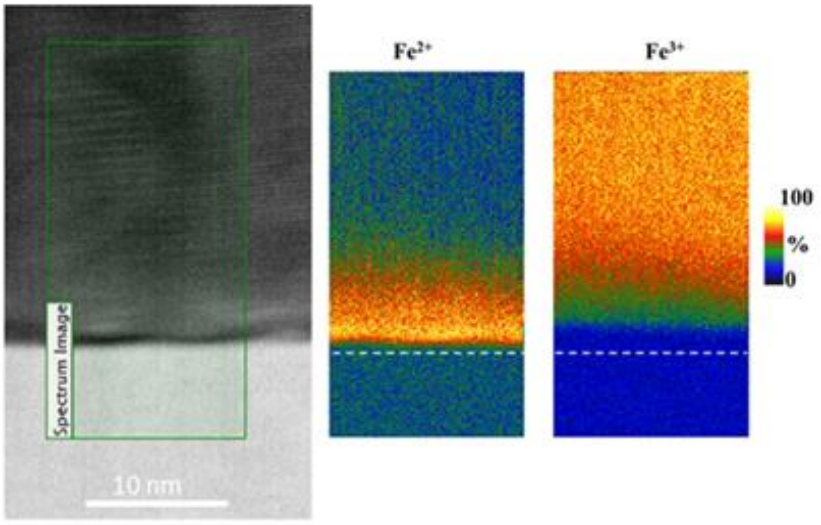

Fig. 4. 17. Distribution of Fe^{2+} and Fe^{3+} ions obtained by MLLS methods, the white dashed line represents the film/YSZ interface.

For a quantitative analysis of the present valence states in iron compounds, integral intensity ratios were calculated (L_3/L_2), using a double arctan function for background subtraction[i] and 2 eV windows for peak intensity integration, in agreement with different oxidation state determination (van Aken 1998, Yanget al, 2016). This was done with the purpose of determining the presence of multivalence state in different zones of the film, starting from the film/substrate interface and taking parallel scans towards the film. Considering the position "0 nm" as the ferrite/YSZ interface, the trend of an increasing ratio is obviously visible, this leads to the idea of a lower valence state (reduction) of the Fe ions close to the interface while, towards the bulk part of the film the presence of ferric ions (Fe^{3+}) dominates the spectrum. In the first 4 nm from the interface, a higher concentration of 2+ ion was detected, with a transition zone between 4 and 6 nm where both valences coexist almost in the same ratio, 6 nm further from the interface, the expected valence state (Fe^{3+}) for the film in present (Fig. 4. 18). For further quantification of ferric ions in the sample, an additional measurement of the branching ratio ($Fe^{3+}/\Sigma Fe$) is plotted in Figure 4. 19, where the concentration of Fe^{3+} starts at 0.8 and increases within the

[i] Double Arctangent function EELS Background fitting tool, D. R. G. Mitchell, www.dmscripting.com.

distance from the interface, until a constant value around 0.9 is reached at approximately 8 nm from the interface. All of these agrees with the universal curve described in Figure 4. 18, where divalent and mixed compounds, such as magnetite, present an intensity ratio between 2 and 6, meanwhile a ratio above 6 is typically indicating a dominant contribution from trivalent iron. According to some references (Yang et al., 2016) for a 100% concentration of ferric ions, the corresponding ratio is approximately 9.58 found in pure Fe_2O_3 (Fig. 4. 18). The difference in intensity ratios observed across the interface confirms the presence of a secondary valence state arising from the formation of magnetite (Fe_3O_4) mostly localized at the interface, this being consistent with the observed spinel-like atomic structure in the STEM images (Fig. 4. 3). In the experimental procedure reported by our collaborators, a controlled oxygen environment for sample growth is used and this would help to avoid the formation of secondary phases. However, according to our results related to the corresponding iron L-edge, magnetite is present in the first 5 nm of the film, while the increase in the white lines ratio is directly consistent with the shifting of the peak maxima to higher energies and the presence of an additional peak as previously discussed.

The results from the L_{23} edge analysis confirm the distribution of distinct Fe ions with different coordination complex. At first insight, the EELS maps, and later the spectra obtained from the sample show a multivalence behavior dominated by the presence of Fe^{3+} in octahedral sites and a small contribution of tetrahedral complexes in the bulk part of the film. In addition, a reduction in the valence state is proven by the splitting of the L_2 edge and a shift of 1.5 eV to lower energies in the L_2 maximum. In addition, a change in resolved features of the L_3 edge. Analysis from specific zones mentioned in the text, i. e. bright and dark spots as well as a spinel-like structure suggests the presence of the mixed valence polymorph, magnetite, accompanied by the formation of lower valence regions showing a decrease of 1.1 eV in the L_3 energy position. Further analysis of the oxygen K-edge will help to understand the bonding conditions and possible distortions on the coordination complexes present in the specimen.

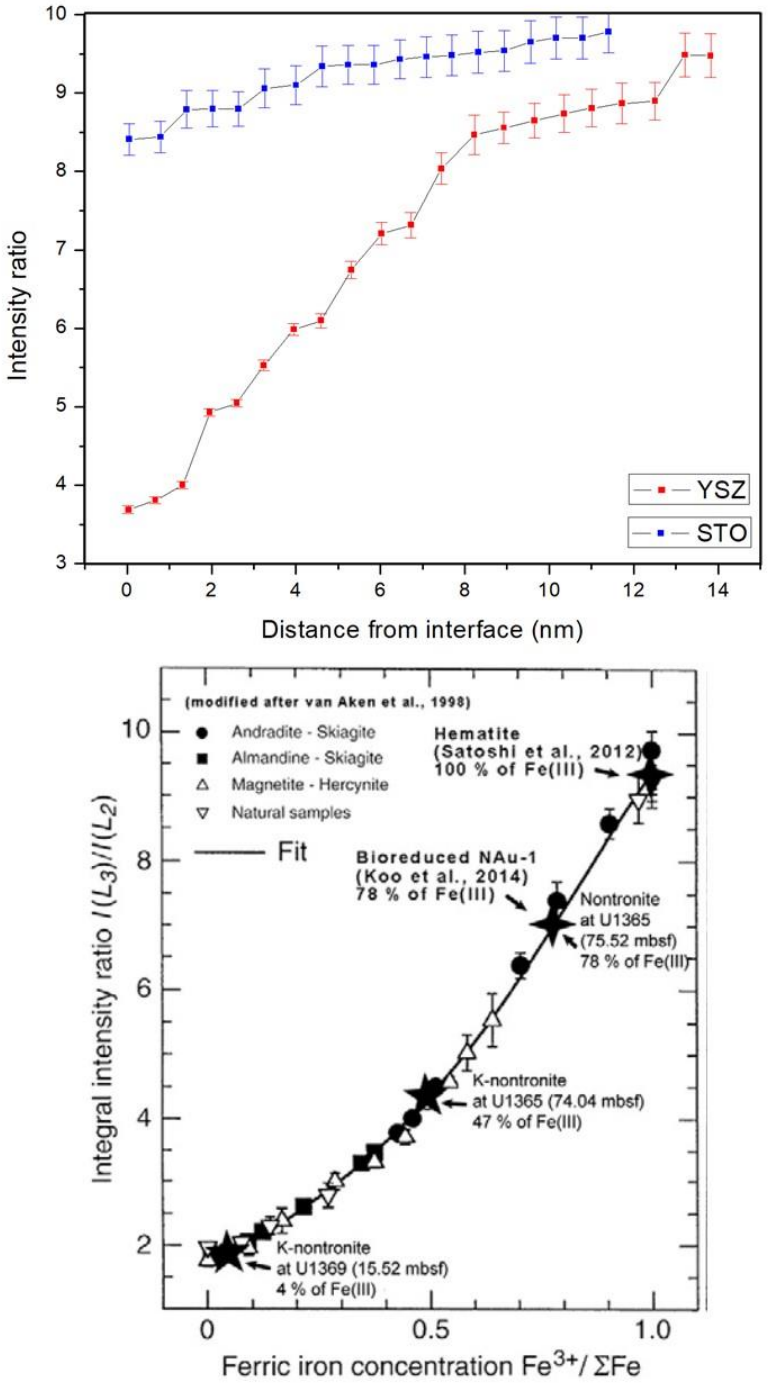

Fig. 4. 18. Top: graph showing the intensity ratio of L_{23} edge as function of distance from the interface for YSZ and STO substrates. Bottom: universal curve of Ferric ion concentration, Republished with permission from Yang et al, 2016.

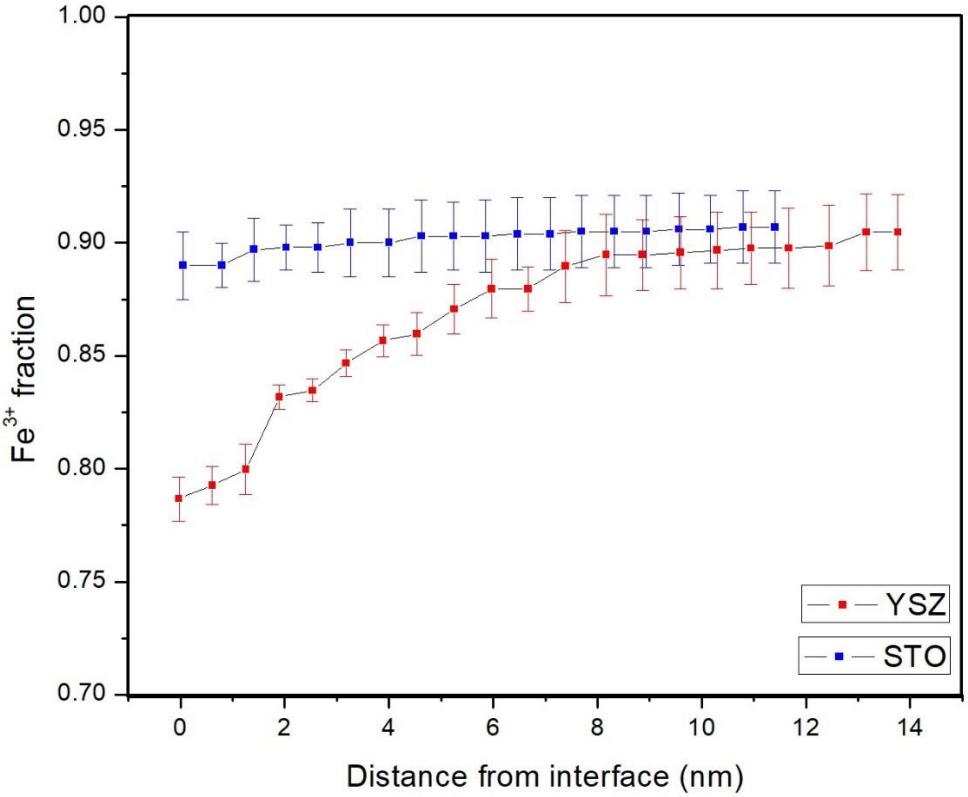

Fig. 4. 19. Graph of the Fe^{3+} concentration (branching ratio) as function of the distance from the interface.

In addition to the determination of the valence state of the sample, the d-electron distribution represented by the L_{23} ionization edge in the EELS spectrum provides information to that is relevant to understand the magnetic behavior of the system. The total magnetic moment of a specific element or compound is given by the number of unpaired electrons localized in partially occupied shells. In the case of iron, its four unpaired electrons from the 3d shell give a total magnetic moment of $4\mu_B$. However, the final magnetic moment is extremely dependent on the chemical bonding and crystal conditions when iron is attached to oxygen generating different values of final magnetic moments for its distinct polymorphs. The universal value for Fe^{3+} ions has been settled as $5\mu_B$, but calculated values have been reported to be between 4.55 and 4.69 μ_B for octahedral coordinated ions and 4.29 μ_B for tetrahedral symmetry (Goss, 1988). However, the

reduction in the branching ratio as the distance from the interface is reduced, is believed to influence the macroscopic magnetic behavior of the film. In addition, the distribution of d electrons has been proven to influence both covalency and local magnetic moment, Morrison et al (1985) stablished the correlation between the number of holes on $d_{5/2}$ and $3_{d/s}$ subshells, following a linear relationship for a reduction in the L_3/L_2 intensity ratio inducing a reduction in the local magnetic moment (Eq. 4. 3).

$$\frac{h(d_{5/2})}{h(d_{3/2})} = \frac{1}{6}\left[\frac{5}{2}\frac{L_3}{L_2}\frac{E_{L2}}{E_{L3}} - 1\right] \tag{4.3}$$

Where L_2, L_3 are the intensities of the white lines and E_{L2}, E_{L3} are the energies (eV) of the maximum of each transition. The calculated values for the number of d-state available holes in epsilon ferrite deposited on both YSZ and STO substrates are plotted in Fig. 4. 20, showing a that values are relatively uniform in the bulk part of the film but, within a distance of 8 nm from the interface, a linear decrease is noticed being concomitant with the Fe^{3+} ion concentration displayed in Fig. 4. 19. A direct comparison between the branching ratio and the local magnetic moment has been carried out in Fe_xGe_{1-x} alloys where the decrease in iron magnetic moment is accompanied by the decrease in the branching ratio, in analogous manner it was found that the branching ratio of $Fe_{30}Y_{70}$ compounds is lower than in pure Fe followed by a decreased net magnetic moment. Moreover, high and low spin states can be identified, according to Pease et al (2001), high-spin Cr-Au alloys possess a bigger branching ratio that pure Cr. In the case of iron oxides, Colliex reported in 1991 an increase from 1.5 (in FeO) to 2.4 (in γ-Fe_2O_3) connected to an enhanced local magnetic moment from low to high spin state. Finally, various iron-based compounds have been tested resulting in a smaller branching ratio for a low-spin FeS_2 in comparison with high-spin Fe, Fe_3O_4 and Fe_2O_3 (Thole and ven der Laan, 1991). However, since the white-line intensity ratio is extremely dependent in the used integration method, the final values might differ among distinct references. The calculated band occupancy displayed in Fig. 4.20 has been related to an enhancement in the magnetic moment of Fe. This being said and using the ion distribution displayed in Fig. 4. 17, the contribution to the total magnetic moment of the specimen in terms of Bohr magnetons can be approximate by the calculated

branching ratios across the film/substrate interface. As shown in Fig. 4.20, in the bulk part of the film deposited on YSZ, a considerable increase in the density of holes from the interface towards the bulk part of the film is noticed. Within 8 nm from the interface, a reduced value of the density of available holes can be related to a decrease in the magnetic moment. While for the bulk part of the film, a relatively homogeneous valence state distribution, therefore a consistent density of holes is directly related to an enhancement of the magnetic moment. In the case of the STO substrate, the branching ratio as well as the oxidation state remain almost homogeneous throughout the film, generating a smaller knee, i.e. less decoupling in the magnetic hysteresis curve. Furthermore, changes in the coordination environment such as octahedral and tetrahedral symmetries have been pointed out to play an important role in the measured values of magnetization and coercivity (Goss, 1988).

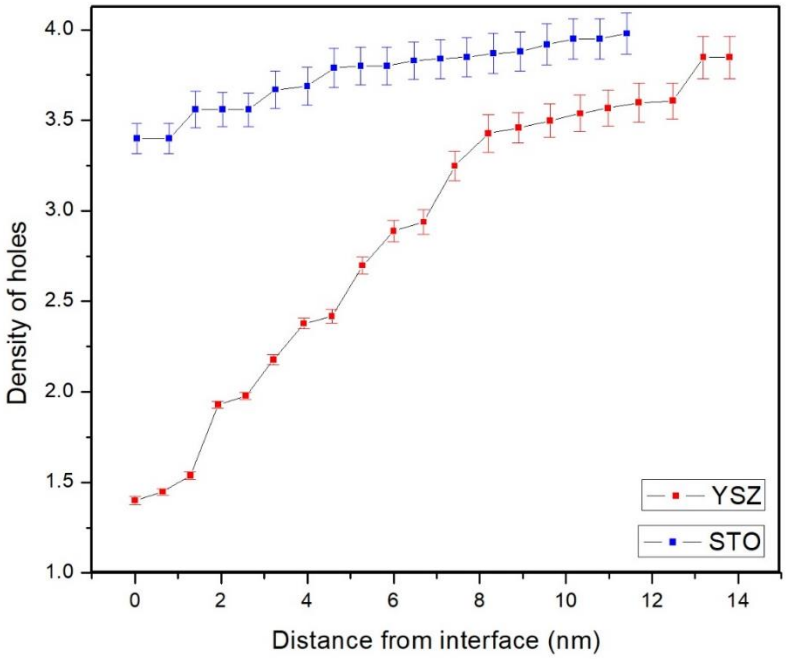

Fig. 4. 20. Graph of the ratio of holes in the d subshells as function of the distance from the interface for samples deposited in STO and YSZ substrates, calculated according to Eq. 4.3.

Due to the soft-magnet nature of the magnetite localized in the epsilon ferrite/YSZ substrate, the observed "knee" in the hysteresis curve is attributed to the exchange decoupling interaction between this mentioned phase and the hard-magnet epsilon ferrite. Moreover, the magnetic exchange length, the space below which the magnetization reversal occurs almost uniformly (no jump in hysteresis curve) has been calculated to be around 5 nm for magnetite. The variation in magnetite layer thickness, from 5 to 8 nm along the interface generates an exchange decoupling directly proportional to the increase in the presence of the magnetite phase. Previous studies showed that the increment of soft-magnet phase thickness in multilayer systems induces a bigger decoupling in the measured hysteresis curves (Rodríguez Rodríguez et al., 2015).

4.3.4 Oxygen K-edge

The oxygen spectrum is normally divided in two regions; the first is attributed to the dominant presence of oxygen 2p hybridized states with transition metal 3d bands, while the second region, 5-10 eV above threshold, is dominated by the p-oxygen hybridization with 4s and 4p metal states (Fisher & Manghnani, 1971). (Grunes, Leapman, Wilker, Hoffmann, & Kunz, 1982) discussed the features in the O K-edge for some 3d TM oxides using a single-electron transition model from the 1s core level to the unoccupied 2p orbitals hybridized, the single-electron model works well for the first two molecular orbitals however for a higher number of electrons this model seems to be too simplistic (Mitterbauer et al., 2003). Transition metal oxides can present multiple crystal field effects resulting in the splitting of the generated d-states making the new molecular orbitals available for transitions listed in decreasing order of energies as follows (Fig. 4. 21):

- $4t_{1u}$ (4p, 2p π)
- $3a_{1g}$ (4s, 2p σ)
- $3e_g$ (3d, 2p σ)
- $2t_{2g}$ (3d ,2p π)

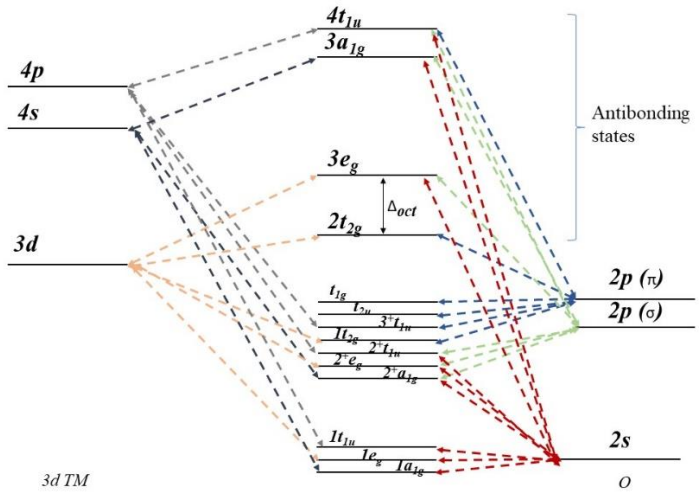

Fig. 4. 21. Molecular orbital diagram for transition metal oxides. The superindex + indicates bonding state while – stands for antibonding conditions. Adapted from Grunes et al, 1982.

We gained insight from the bonding environment of interface and film through analysis of the oxygen K-edge. As it can be seen from the different acquired spectra (Fig. 4. 22), from spectrum 1 (within the bulk of the film) to 8 (2 nm from the interface) similar features are observed with minimum changes between them. There is a prepeak at approximately 530 eV followed by a dominant broad edge around 540 eV that extends as a broad feature varying its position and finally there are broad modulations around 560-565 eV. In general, iron bonding conditions for cation sites are determined by local symmetry and according to various authors (Chen et al 2009), the intensity and position of prepeaks in O K-edge are mainly determined by the degree of hybridization between 3d states from a transition metal and the 2p states from the oxygen. Due to the difference in cation sites from particular valence states in iron oxides, the partially tetrahedral and full octahedral symmetries as well as the exchange splitting, the shape and intensities of the edges for ε-Fe_2O_3 and Fe_3O_4 have more in common than other +3 valence oxides.

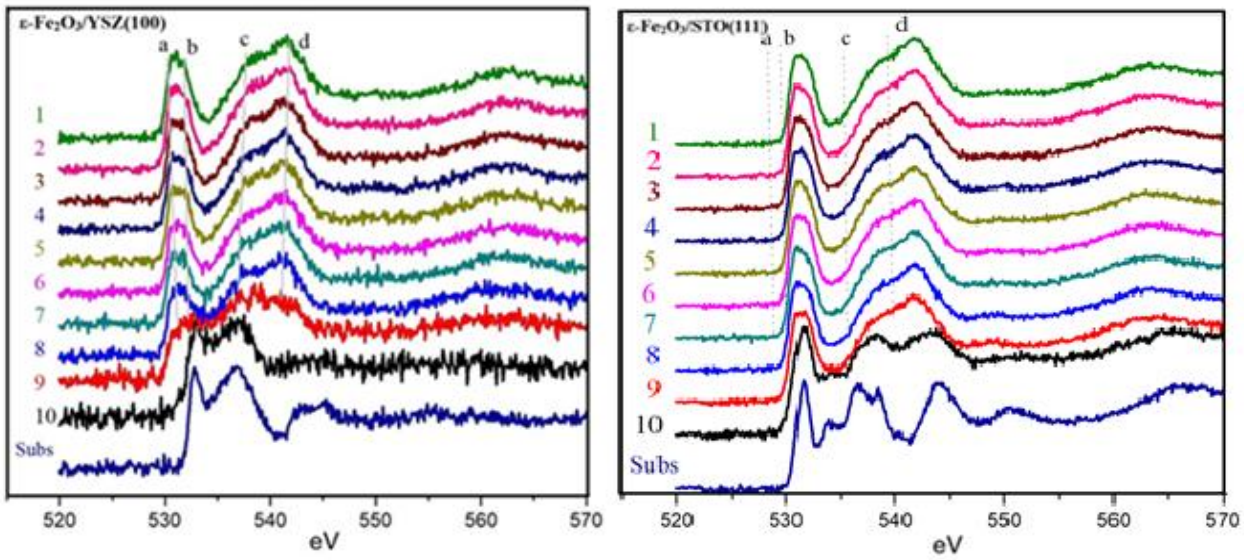

Fig. 4. 22. Corresponding O K-edge for the EELS spectra for samples deposited on YSZ (left) and STO (right). Using the same color code than Figure 4. 6D plus the addition of the O K-edge from the substrates (dashed line at the bottom).

In Figure 4. 23, the oxygen K-edge spectra for specific regions at the interface are plotted, where the edge for the zone labeled as 3 (spinel-like structure) and zone 2 (dark region) present a similar shape for the acquired edge from the bulk part of the film with a certain decrease in the relative intensity of the prepeak attributed to a reduction of orbital hybridization while the edge from the bright cluster exhibits almost no prepeak suggesting a low or no presence of hybridization.

Changes in the prepeak can be interpreted as a decrease in intensity of O 2p – Fe 3d band relative to O 2p – Fe 4sp band, dominated by the decrease of unoccupied 3d states available for hybridization. A substantial lower intensity of the 3d band for 5d and 6d oxides can be explained by the decreased hybridization due to a shrinking of the orbitals in the late-transition oxides. Covalency reduces the number of filed states with O 2p (Pedio et al., 1989).

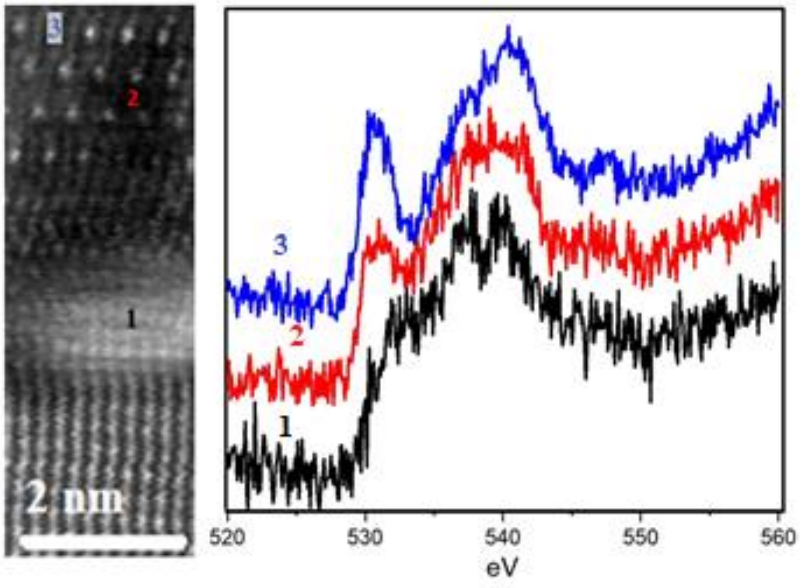

Fig. 4. 23. Oxygen K-edge spectra acquired form the bright and dark zones, as well as the spinel-like structure.

Following the idea of a single electron model, the oxygen K-edge interpretation relies in the 1s to Np excitations. As an important result, 2p oxygen states overlapping with 3d iron orbitals generate a crystal-field splitting phenomenon present resulting in non-degenerate t_{2g} and e_g levels known as ligand-field splitting. Colliex et al 1991, mentioned the $2t_{2g}$ to $3e_g$ difference is 1.7 for ferrous and 2.2 eV for ferric ions while the spin-orbit splitting is about 2.9 and 2.7 respectively. The constant prepeak in the oxygen K-edge, situated around 530 eV has been reported to be dependent of the transitions from the ground state 1s to the 2p unoccupied states, which are also known to present certain degree of hybridization with the 3d states from iron (De Groot et al., 1989). The prepeak feature can be identified as the t_{2g} and e_g symmetry bands separated by ligand-field splitting effects. In 3d compounds only t_{2g} are filled, from 5d compounds the e_g filled states increase the lattice parameter which generates a decrease of hybridization. In spectra 1-8 for the YSZ substrate, a gradual reduction in prepeak intensity relative to the broader edge can be observed while it is extremely noticeable in spectrum 9 (Fig. 4. 22 left) and also occurs in spectra 2 and 3 in Fig. 4. 23. This reduction is linearly related to the decrease of hole population in the 3d band, number of electrons in the ground state, compared with the 4sp band, vanishing of

features in the observed in the prepeak features for spectra (1-3) are attributed to the decrease in hybridization of Fe 3d – O 2p orbitals; which reflects the apparent environment for the distorted octahedral sublattice (Gazquez et al 2016). Moreover, a split in this feature is also described to be dependent on ligand effects; in case of +3 valence state, the prepeak shows a separation of approximately 1.2 eV between its features, meanwhile a separation of 0.8-0.9 eV is present in the other compounds. However, according to previous studies reported by Groot et al (1989), the similar behavior observed in the O K-edge for both types of oxides leads to the idea of a higher dependence in the type of symmetry rather than the crystal-split theory. Moreover, the extreme reduction of prepeak intensity observer for spectrum 9 (Fig. 4. 22) and in spectrum 1 (Fig. 4. 23) is also attributed to a decrease in the oxygen concentration, suggesting a high concentration of iron ions in the bright spots.

The shape of the O K-edge displayed in spectrum 10 for both samples, shows certain similarities with the substrate (dashed line) O K-edge. Combined, with the fact that there is a strong Fe signal in the exact same location, this suggest that we have a structure similar to YSZ and STO in terms of the O sublattice where, however the Fe atoms substitute Zr and Sr atoms in their cubic coordination environments. This being said, now we can see that the iron coordination is in polyhedra within a cubic system and no longer in octahedral or tetrahedral sties, this also generating a change in the magnetic exchange interaction induced by the change in the bonding length and angles exhibited now in pseudocubic conditions. The presence of this peculiar coordination can explain the behavior observed for the hole density of the STO sample for which, despite of the lack of secondary phases, a small segregation of iron towards the substrate generates a decrease in the total magnetic moment of the sample. For the YSZ sample, this segregation is additional to the cation distribution previously described. Reports of cation diffusion from the film towards the free surface has been pointed out either as a way of strain relaxation or as a consequence of high temperature annealing process, that could come from the film growth process. Moreover, due to the presence of compressive in-plane strain and out-of-plane tensile strain, as showed by the GPA results, Jan-Teller effect could be promoted by changes in the lattice parameters, generating depressed magnetic response from the cation diffused layer (Estradé

et al., 2007). However, a noticeable change in the valence state and later cation distribution is only seen in the YSZ as a possible consequence of the *hard epitaxy* mechanism that takes place in the growth of these films, according to previous reports (Zur & Mcgill, 1984), despite two materials having lattice matching this does not warrant that the film will grow epitaxially because the chemistry conditions of the surface still have significant importance in controlling the epitaxial growth mechanisms.

4.4 Conclusions

A combined STEM-EELS studied has allowed us to the obtain important information regarding the microstructure and chemical state of ε-Fe_2O_3 grown on YSZ (100) and STO (111) miscut substrates. Several factors have been pointed out as contributing to the reported anomalies in the magnetic properties of this material and their discrepancies with the properties obtained by simulations, nanoparticles or nanorod synthesis methods. It was shown that multiple strain relaxation mechanism can take place in the analyzed system through: the presence of plastic deformation through dislocations (i. e. misfit dislocations) at the interface of the film/STO or through the generation of a secondary phase (YSZ substrate). The EELS measurements have also been supported by evidence that strain-induced defects strongly affect the chemical state of the sample by inducing distortions in the bonding conditions that can be seen in changes in the O K and Fe L edges. It has been pointed out as well that the ultimate goal of epitaxial thin films production is to achieve high-quality thin films with extraordinary magnetic properties. However, due to the complexity of the epitaxial process several secondary effects such as misfit and edge dislocations, in-plane twin growth, lattice distortion and changes in the valence state, mostly caused by cation segregation, have been identified as the main problems to achieve the expected magnetic response of epsilon ferrite by inducing distortions in the magnetic moment interactions. These effects govern the overall macroscopic magnetic behavior being reflected in the anomalous (i.e. low magnetization values and pinched shape) hysteresis curves reported in the literature by our collaborators. Nanoscale characterization has been proven to be an extremely powerful technique to gain insight in the research and development of novel materials for potential further real-world applications.

5 Final conclusions and perspectives.

The great advantages of analytical electron microscopy techniques applied to the characterization of epitaxially grown epsilon ferrite (ε-Fe_2O_3), grown on miscut perovskite substrates (STO and YSZ), have helped to obtained detailed information regarding the microstructure and chemical properties of the film/substrate interface. Through this work we have established a correlation between the structural information and the reported magnetic properties previously reported by our collaborators. The presence of a wide set of defects such as misfit dislocations, out-of-phase boundaries and changes in the valence state of iron cations have been detected and pointed as factors that play a determinant role in the macroscopic behavior of the produced films. Therefore, a good understanding of the nature of these defects is key in the improvement and optimization of a future large-scale production of iron oxide thin films and its further integration into technological devices.

A first characterization using atomic resolution STEM images helped to visualize the presence of 5° miscut from the selected substrates which generates a tilted growth of the same degree along the film. Moreover, a sharp interface is generated between the epsilon ferrite and the STO (111) substrate while in the interface with YSZ (100) the presence of a buffer layer within 5-8 nm from the interface, consisting of a peculiar atomic arrangement (further identified as magnetite) containing dark regions and bright clusters in alternating positions was noticed. Further electron diffraction analysis confirmed the growth of distinct in-plane domain variants for both STO (111) and YSZ (100) substrates. The usage of a miscut substrate helped to reduce the presence of this polycrystalline growth (as referenced before in the text). However, residual in-plane domains possess their easy magnetic axis pointing towards oppositemutipl directions, generating a decrease in the expected coercive field. The presence of out-of-phase boundaries, seen as a misregistry of the periodicity of the atomic rows by a fraction of the unit cell, was also detected by a qualitative interpretation of the obtained HAADF images. This type of translational defect generates a change in the cation bonding conditions which has a considerable impact in the overall magnetic nature of the film.

In addition to the interpretation of micrographs and electron diffraction patterns, the implementation of geometrical phase analysis was used to quantify the amount of strain present in the film. For both substrates, the presence of compressive in-plane strain varying from 2.35% for STO (111) and 2.42-2.63 % for YSZ (100) was measured corresponding to a reduced a-lattice parameter while the out-of-plane strain measurements suggest a relaxed c-lattice constant. Moreover, through the observation of both in-plane and out-of-plane strain maps, it was possible to identify the presence of plastic deformation (misfit dislocations) at the interface of the film/STO substrate as well as edge dislocation between the in-plane domains. In the case of the epsilon ferrite deposited on YSZ, edge dislocations also appear to be present at grain boundaries of the misoriented in-plane domains. In addition, the observed buffer layer present at the interface exhibits alternating zones of high compressive strain and tensile strain, concomitant with the presence of bright and dark regions respectively. The presence of these defects has been identified as a mechanism of partial strain relaxation namely the presence of misfit dislocations and the appearance of an interfacial buffer layer.

Advances in direct electron detection allowed the realization of improved energy resolution EELS measurements allowing us to display both oxygen K and iron L-edges required to analyze the epsilon ferrite/perovskite interfaces and observe possible cation segregation. Analysis of the Fe L-edge revealed no changes of the valence state of Fe for the sample deposited on STO (111). However, for YSZ (100) a gradual reduction in the valence state of iron from the bulk towards the interface of the film represented by a shift to lower energies and a spliting in the L_3 edge, concomitant with a reduction of the L_3/L_2 intensity ratios, demonstrate the presence of Fe^{3+} ions at the bulk part of the film, followed by a mixed valence state (Fe^{3+} and Fe^{2+}) attributed to the presence of magnetite near the interface. Taking advantage of the high spatial resolution of the acquired EELS maps, it was possible to obtain information about the dark and bright regions in the interfacial buffer layer identified in the STEM images, suggesting the localized presence of Fe^{2+} ions.

In addition to the oxidation state, EELS analysis was used to investigate the bonding environment of the iron cations. This effect was observed through changes in the O K-edge

that show a reduction in the hybridization of Fe 3d and O 2p orbitals as well as a small diffusion of iron ions into the substrate lattice generating a change in the ion coordination from polyhedral (octahedral or tetrahedral) to cubic. Quantification of the white-lines of the EELS Fe L-edge was used to obtain more information about the magnetic response of the sample showing a linear relationship between the oxidation state and the local magnetic moment. A secondary phase observed in the ferrite/YSZ sample and a change in the ion coordination observed in both YSZ and STO substrate are pointed out as factors that generate a decrease in the magnetic moment of the sample. This observation has a direct impact in the magnetization and coercivity of the sample.

The stabilization of the epsilon ferrite as thin films deposited on miscut substrates is achieved through a complex epitaxial process that generates either plastic deformation (dislocations) and the formation of secondary phases, in addition to lattice distortions are responsible of changes in the bonding conditions generating a magnetic response of the sample that differs from the exotic observed behavior in other nanocompounds. It is worth to mention the key role played by the implemented nanoscale characterization techniques which allowed the study of localized phenomena (dislocations, buffer layer and cation rearrangement) within less than 10 nm near the interface. In order to improve the production of high-quality epitaxial thin films, the identification and understanding of low-dimensional defects is vital in order to obtain smaller and more powerful devices. Future studies can include the use of atomic resolution EELS maps and comparison with simulated spectra to obtain more information about the bonding conditions and spin state at atomic resolution. In addition, the ability to obtain electron diffraction patterns at each pixel over large areas showed the potential to provide strain information analysis of the thin film interfaces. Further work could be obtained in more systematic studies correlating the very localized strain with very local EELS measurements.

6 References

1. Abbate, M., De Groot, F. M. F., Fuggle, J. C., Fujimori, A., Strebel, O., Lopez, M. F., … Uchida, S. (1992). Controlled-valence properties of La1-xSrxFeO3 and La1-xSrxMnO3 studied by soft-x-ray absorption spectroscopy. *Physical Review B*, *46*(8), 4511–4519. https://doi.org/10.1103/PhysRevB.46.4511
2. Agrawal, P., Guo, J., Yu, P., Hébert, C., Passerone, D., Erni, R., & Rossell, M. D. (2016). Strain-driven oxygen deficiency in multiferroic SrMnO3 thin films. *Physical Review B*, *94*(10), 1–9. https://doi.org/10.1103/PhysRevB.94.104101
3. Anderson, P. W. (1966). Theory of localized magnetic states in metals. *Journal of Applied Physics*, *37*(3), 1194. https://doi.org/10.1063/1.1708389
4. Askeland, D. R., Fulay, P. P., & Wright, W. J. (2011). The science and engineering of materials. *Stamford, CT : Cengage Learning, C2011*, 944. https://doi.org/10.2172/15009526
5. Auerhammer, J. M., & Rez, P. (1989). Dipole-forbidden excitations in electron-energy-loss spectroscopy. *Physical Review B*, *40*(4), 2024–2030. https://doi.org/10.1103/PhysRevB.40.2024
6. Biswas, A., & Jeong, Y. H. (2017). Growth and engineering of perovskite SrIrO 3 thin films. *Current Applied Physics*, *17*(5), 605–614. https://doi.org/10.1016/j.cap.2016.09.020
7. Browning, N., Arslan, I., & Erni, R. (2011). Low-Loss EELS in the STEM. In Scanning Transmission Electron Microscopy. In S. J. Pennycook & P. D. Nellist (Eds.), *Scanning Transmission Electron Microscopy*. New York, USA: Springer. https://doi.org/10.1007/978-1-4419-7200-2
8. Brundle, C. R., Chuang, T. J., & Wandelt, K. (1977). Core and valence level photoemission studies of iron oxide surfaces and the oxidation of iron. *Surface Science*, *68*(C), 459–468. https://doi.org/10.1016/0039-6028(77)90239-4
9. Brydson, R., Sauer, H., Engel, W., Thomas, J. M., & Zeitler, E. (1989). Co-ordination fingerprints in electron loss near-edge structures: Determination of the local site symmetry of aluminium and beryllium in ultrafine minerals. *Journal of the Chemical Society, Chemical Communications*, (15), 1010–1012. https://doi.org/10.1039/C39890001010
10. Buffat, B., & Tuilier, M. H. (1987). X-Ray Absorption Edges of Iron and Cobalt with Six-Fold Coordination in Oxides: Influence of Site Distortion and Oxidation State, *64*(4), 401–406.
11. Cao, G. (2004). *Nanostructures & Nanomaterials Synthesis, Properties & Applications*. London: Imperial College Press.
12. Cao, J., & Wu, J. (2011). Strain effects in low-dimensional transition metal oxides. *Materials Science and Engineering R: Reports*, *71*(2–4), 35–52. https://doi.org/10.1016/j.mser.2010.08.001
13. Carraro, G., Barreca, D., MacCato, C., Bontempi, E., Depero, L. E., De Juli??n Fern??ndez, C., & Caneschi, A. (2013). Supported ?? and ?? iron oxide nanomaterials by chemical vapor deposition: Structure, morphology and magnetic properties. *CrystEngComm*, *15*(6), 1039–1042. https://doi.org/10.1039/c2ce26821c

14. Chen, S.-Y., Gloter, A., Zobelli, A., Wang, L., Chen, C.-H., & Colliex, C. (2009). Electron energy loss spectroscopy and *ab initio* investigation of iron oxide nanomaterials grown by a hydrothermal process. *Physical Review B, 79*(10), 104103. https://doi.org/10.1103/PhysRevB.79.104103
15. Chu, Y. H., Martin, L. W., Holcomb, M. B., Gajek, M., Han, S. J., He, Q., … Ramesh, R. (2008). Electric-field control of local ferromagnetism using a magnetoelectric multiferroic. *Nature Materials*, *7*(6), 478–482. https://doi.org/10.1038/nmat2184
16. Coey, J. M. D. (2009). *Magnetism and Magnetic Materials*. *Journal of Magnetism and Magnetic Materials*. Cambridge, UK: Cambridge University Press. https://doi.org/10.1016/0304-8853(84)90352-4
17. Coey, J. M. D. (2012). Permanent magnets: Plugging the gap. *Scripta Materialia*, *67*(6), 524–529. https://doi.org/10.1016/j.scriptamat.2012.04.036
18. Colliex, C., Manoubi, T., & Ortiz, C. (1991). Electron-energy-loss-spectroscopy near-edge fine structures in the iron-oxygen system. *Physical Review B, 44*(20), 11402–11411. https://doi.org/10.1103/PhysRevB.44.11402
19. Corbellini, L. (2017). Growth and Characterization of Epitaxial Thin Films of Epsilon Ferrite (ε-Fe2O3). PhD. Thesis. Retrieved from http://espace.inrs.ca/6927/1/Corbellini%2C%20Luca.pdf.
20. Corbellini, L., Lacroix, C., Harnagea, C., Korinek, A., Botton, G. A., Ménard, D., & Pignolet, A. (2017). Epitaxially stabilized thin films of ϵ-Fe2O3 (001) grown on YSZ (100). *Scientific Reports*, *7*(1). https://doi.org/10.1038/s41598-017-02742-9
21. Corbellini, L., Lacroix, C., Ménard, D., & Pignolet, A. (2017). The effect of Al substitution on the structural and magnetic properties of epitaxial thin films of epsilon ferrite. *Scripta Materialia*, *140*, 63–66. https://doi.org/10.1016/j.scriptamat.2017.07.005
22. Crocombette, J. P., Pollak, M., Jollet, F., Thromat, N., & Gautier-Soyer, M. (1995). X-ray-absorption spectroscopy at the Fe L2,3 threshold in iron oxides. *Physical Review B, 52*(5), 3143–3150. https://doi.org/10.1103/PhysRevB.52.3143
23. De Groot, F. M. F., Grioni, M., Fuggle, J. C., Ghijsen, J., Sawatzky, G. A., & Petersen, H. (1989). Oxygen 1s X-ray-absorption edges of transition-metal oxides. *Physical Review B, 40*(8), 5715–5723. https://doi.org/10.1103/PhysRevB.40.5715
24. Dvorak, J., Idzerda, Y. U., Ogale, S. B., Shinde, S., Wu, T., Venkatesan, T., … Ramesh, R. (2005). Are strain-induced effects truly strain induced? A comprehensive study of strained LCMO thin films. *Journal of Applied Physics, 97*(10), 1–4. https://doi.org/10.1063/1.1845974
25. Egerton, R. F. (2011). *Electron Energy-Loss Spectroscopy in the Electron Microscope*. *Reports on Progress in Physics* (Vol. 72). https://doi.org/10.1007/978-1-4419-9583-4
26. Estradé, S., Arbiol, J., Peiró, F., Abad, L., Laukhin, V., Balcells, L., & Martínez, B. (2007). Cationic diffusion in La23 Ca13 Mn O3 thin films grown on LaAl O3 (001) substrates. *Applied Physics Letters*, *91*(25), 2–4. https://doi.org/10.1063/1.2799740
27. Estradé, S., Arbiol, J., Peiró, F., Infante, I. C., Sánchez, F., Fontcuberta, J., …

Colliex, C. (2008). Cationic and charge segregation in La2/3Ca1/3MnO3thin films grown on (001) and (110) SrTiO3. *Applied Physics Letters*, *93*(11), 2006–2009. https://doi.org/10.1063/1.2981574

28. Fabbri, E., Pergolesi, D., & Traversa, E. (2010). Ionic conductivity in oxide heterostructures: The role of interfaces. *Science and Technology of Advanced Materials*, *11*(5). https://doi.org/10.1088/1468-6996/11/5/054503
29. Fisher, E. S., & Manghnani, M. H. (1971). Effects of changes in volume and c/a ratio on the pressure derivatives of the elastic moduli of H.C.P. Ti and Zr. *Journal of Physics and Chemistry of Solids*, *32*(3), 657–667. https://doi.org/10.1016/S0022-3697(71)80406-7
30. Garvie, L. A. J., Craven, A. J., & Brydson, R. (1994). Use of electron-energy loss near-edge fine structure in the study of minerals. *American Mineralogist*, *79*(5–6), 411–425.
31. Gázquez, J., Sánchez-santolino, G., Bi, N., Roldán, M. A., Cabero, M., Pennycook, S. J., & Varela, M. (2016). Materials Science in Semiconductor Processing Applications of STEM-EELS to complex oxides.
32. Gázquez, J., Sánchez-Santolino, G., Biškup, N., Roldán, M. A., Cabero, M., Pennycook, S. J., & Varela, M. (2017). Applications of STEM-EELS to complex oxides. *Materials Science in Semiconductor Processing*, *65*, 49–63. https://doi.org/10.1016/j.mssp.2016.06.005
33. Giannuzzi, L. A., & Stevie, F. A. (1999). A review of focused ion beam milling techniques for TEM specimen preparation, *30*, 197–204.
34. Giannuzzi, L. A., & Stevie, F. A. (2005). *Introduction fo Focused Ion Beams*. New York: Springer.
35. Gich, M., Fina, I., Morelli, A., Sánchez, F., Alexe, M., Gàzquez, J., … Roig, A. (2014). Multiferroic iron oxide thin films at room temperature. *Advanced Materials*, *26*(27), 4645–4652. https://doi.org/10.1002/adma.201400990
36. Gich, M., Frontera, C., Roig, A., Taboada, E., Molins, E., Rechenberg, H. R., … Nogués, J. (2006). High- and low-temperature crystal and magnetic structures of ε-Fe 2O3 and their correlation to its magnetic properties. *Chemistry of Materials*, *18*(16), 3889–3897. https://doi.org/10.1021/cm060993l
37. Gich, M., Gazquez, J., Roig, A., Crespi, A., Fontcuberta, J., Idrobo, J. C., … Varela, M. (2010). Epitaxial stabilization of ε-Fe2O3 (00l) thin films on SrTiO3 (111). *Applied Physics Letters*, *96*(11), 112508. https://doi.org/10.1063/1.3360217
38. Gilks, D., Nedelkoski, Z., Lari, L., Kuerbanjiang, B., Matsuzaki, K., Susaki, T., … Lazarov, V. K. (2016). Atomic and electronic structure of twin growth defects in magnetite. *Scientific Reports*, *6*(September 2015), 1–8. https://doi.org/10.1038/srep20943
39. Goss, C. J. (1988). Saturation magnetisation, coercivity and lattice parameter changes in the system Fe3O4-γFe2O3, and their relationship to structure. *Physics and Chemistry of Minerals*, *16*(2), 164–171. https://doi.org/10.1007/BF00203200
40. Griesche, J., Enderlein, L., & Schikora, D. (1988). Orientation and Strain in Heteroepitaxial Growth, *11*, 11–38.
41. Grunes, L. A. (1983). Study of the K edges of 3d transition metals in pure and

oxide form by X-ray-absorption spectroscopy. *Physical Review B*, *27*(4), 2111–2131. https://doi.org/10.1103/PhysRevB.27.2111

42. Grunes, L. A., Leapman, R. D., Wilker, C. N., Hoffmann, R., & Kunz, A. B. (1982). Oxygen K near-edge fine structure: An electron-energy-loss investigation with comparisons to new theory for selected 3d transition-metal oxides. *Physical Review B*, *25*(12), 7157–7173. https://doi.org/10.1103/PhysRevB.25.7157
43. Hibma, T., Voogt, F. C., Niesen, L., van der Heijden, P. A. A., de Jonge, W. J. M., Donkers, J. J. T. M., & van der Zaag, P. J. (1999). Anti-phase domains and magnetism in epitaxial magnetite layers. *Journal of Applied Physics*, *85*(8), 5291–5293. https://doi.org/10.1063/1.369857
44. Hytch, M., Snoeck, E., & Kilaas, R. (1998). Quantitative measurement of displacement and strain fields from HREM micrographs, *74*, 131–146.
45. Ikuhara, Y. (2001). Grain Boundary and Interface Structures in Ceramics. *Journal of the Ceramic Society of Japan*, *109*(7), S110–S120. https://doi.org/http://doi.org/10.2109/jcersj.109.1271_S110
46. Ikuhara, Y., & Shibata, N. (2011). Application to Ceramic Interfaces. In S. J. Pennycook & P. D. Nellist (Eds.), *Scanning Transmission Electron Microscopy*. New York, USA: Spriger. https://doi.org/10.1007/978-1-4419-7200-2
47. Jang, J. H., Mishra, R., Kim, Y., He, Q., Lee, J., Yoon, M., & Pantelides, S. T. (2015). Phase Transformations and Surface / Interface Properties in Functional Perovskites with Aberration-Corrected STEM / EELS, *21*(1213), 2429–2430. https://doi.org/10.1017/S1431927615012921
48. Jin, J., Ohkoshi, S. I., & Hashimoto, K. (2004). Giant Coercive Field of Nanometer-Sized Iron Oxide. *Advanced Materials*, *16*(1), 48–51. https://doi.org/10.1002/adma.200305297
49. Jun, S., Kim, Y. S., Lee, J., & Kim, Y. W. (2001). Dielectric properties of strained (Ba,Sr)TiO3 thin films epitaxially grown on Si with thin yttria-stabilized zirconia buffer layer. *Applied Physics Letters*, *78*(17), 2542–2544. https://doi.org/10.1063/1.1367309
50. Kiguchi, T., Aoyagi, K., Ehara, Y., Funakubo, H., Yamada, T., Usami, N., & Konno, T. J. (2011). Configuration and local elastic interaction of ferroelectric domains and misfit dislocation in PbTiO3/SrTiO3epitaxial thin films. *Science and Technology of Advanced Materials*, *12*(3), 1–9. https://doi.org/10.1088/1468-6996/12/3/034413
51. Kociak, M., Stéphan, O., Walls, M., Tencé, M., & Colliex, C. (2011). Spatially Resolved EELS: The Spectrum-Imaging Technique and Its Applications. In S. J. Pennycook & P. D. Nellist (Eds.), *Scanning Transmission Electron Microscopy2*. New York, USA. https://doi.org/10.1007/978-1-4419-7200-2
52. Koshino, M., Kurata, H., Isoda, S., & Kobayashi, T. (2000). Branching Ratio and L 2 + L 3 Intensities of 3d-Transition Met- als in Phthalocyanines and the Amine Complexes, *7*, 6–7.
53. Leapman, R. D., Grunes, L. A., & Fejes, P. L. (1982). Study of the L23 edges in the 3d transition metals and their oxides by electron-energy-loss spectroscopy with comparisons to theory. *Physical Review B*, *26*(2), 614–635.

https://doi.org/10.1103/PhysRevB.26.614
54. Li, C., Wang, L., Wang, Z., Yang, Y., Ren, W., & Yang, G. (2016). Atomic Resolution Interfacial Structure of Lead-free Ferroelectric K0.5Na0.5NbO3 Thin films Deposited on SrTiO3. *Scientific Reports*, *6*(1), 37788. https://doi.org/10.1038/srep37788
55. Longo, P. (2018). Advantages of Direct Detection and Electron Counting for Electron Energy Loss Spectroscopy Data Acquisition and the Quest of Extremely High-Energy Edges Using Eels. *Microscopy and Microanalysis*, *24*(S1), 60–61. https://doi.org/10.1017/S1431927617000988
56. Lowndes, D. H., Geohegan, D. B., Puretzky, a a, & Norton, D. P. (2012). Synthesis Thin-Film Materials by Pulsed Deposition Laser. *Science*, *273*(5277), 898–903.
57. Ma, C., Liu, M., Chen, C., Lin, Y., Li, Y., Horwitz, J. S., … Zhang, Q. (2013). The origin of local strain in highly epitaxial oxide thin films. *Scientific Reports*, *3*, 1–5. https://doi.org/10.1038/srep03092
58. MacLaren, I., & Ramasse, Q. M. (2014). Aberration-corrected scanning transmission electron microscopy for atomic-resolution studies of functional oxides. *International Materials Reviews*, *59*(3), 115–131. https://doi.org/10.1179/1743280413Y.0000000026
59. Mahan, G. D. (1975). Collective excitations in x-ray spectra of metals* G. *P Hysica L Review B*, *11*(12), 592–609. https://doi.org/10.1103/PhysRevB.11.4814
60. Markov, I. V. (2003). *Crystal Growth for Beginners*. Singapore: World Scientific Publishing Co. Pte. Lt.d. https://doi.org/10.15713/ins.mmj.3
61. Mchale, A. J. M., Auroux, A., Perrotta, A. J., Navrotsky, A., Mchale, J. M., Auroux, A., … Navrotsky, A. (2018). Surface Energies and Thermodynamic Phase Stability in Nanocrystalline Aluminas Published by : American Association for the Advancement of Science Stable URL : http://www.jstor.org/stable/2893119 All use subject to http://about.jstor.org/terms I ~ REPORTS , *277*(5327), 788–791.
62. Metev, S., & Meteva, K. (1989). Nucleation and growth of laser-plasma deposited thin films. *Applied Surface Science*, *43*(1–4), 402–408. https://doi.org/10.1016/0169-4332(89)90247-X
63. Mitterbauer, C., Kothleitner, G., Grogger, W., Zandbergen, H., Freitag, B., Tiemeijer, P., & Hofer, F. (2003). Electron energy-loss near-edge structures of 3d transition metal oxides recorded at high-energy resolution. *Ultramicroscopy*, *96*(3–4), 469–480. https://doi.org/10.1016/S0304-3991(03)00109-8
64. Momma, K., & Izumi, F. (2011). VESTA 3 for three-dimensional visualization of crystal, volumetric and morphology data. *Journal of Applied Crystallography*, *44*(6), 1272–1276. https://doi.org/10.1107/S0021889811038970
65. Morrison, T. I., Brodsky, M. B., Zaluzec, N. J., & Sill, L. R. (1985). Iron d-band occupancy in amorphous FexGe1-x. *Physical Review B*, *32*(5), 3107–3111. https://doi.org/10.1103/PhysRevB.32.3107
66. Muller, D. A. (1999). Why changes in bond lengths and cohesion lead to core-level shifts in metals, and consequences for the spatial difference method.

Ultramicroscopy, *78*(1–4), 163–174. https://doi.org/10.1016/S0304-3991(99)00029-7

67. Mundy, J. A., Brooks, C. M., Holtz, M. E., Moyer, J. A., Das, H., Rébola, A. F., … Schlom, D. G. (2016). Atomically engineered ferroic layers yield a room-temperature magnetoelectric multiferroic. *Nature*, *537*(7621), 523–527. https://doi.org/10.1038/nature19343
68. Narayan, J., & Larson, B. C. (2003). Domain epitaxy: A unified paradigm for thin film growth. *Journal of Applied Physics*, *93*(1), 278–285. https://doi.org/10.1063/1.1528301
69. Nedelkoski, Z., Kepaptsoglou, D., Lari, L., Wen, T., Booth, R. A., Oberdick, S. D., … Lazarov, V. K. (2017). Origin of reduced magnetization and domain formation in small magnetite nanoparticles. *Scientific Reports*, *7*, 1–8. https://doi.org/10.1038/srep45997
70. Ohkoshi, S. I., & Tokoro, H. (2013). Hard magnetic ferrite: ε-Fe2O3. *Bulletin of the Chemical Society of Japan*, *86*(8), 897–907. https://doi.org/10.1246/bcsj.20130120
71. Ohring, M. (1995). *Engineering Materials Science*. https://doi.org/10.1017/CBO9781107415324.004
72. Ohtomo, A., & Hwang, H. Y. (2004). A high-mobility electron gas at the LAO/STO heterointerface. *Nature*, *427*(6973), 423–426. https://doi.org/10.1038/nature04773
73. Oka, D., & Fukumura, T. (2017). Crystal engineering for novel functionalities with oxide thin film epitaxy. *CrystEngComm*, *19*(16), 2144–2162. https://doi.org/10.1039/c7ce00322f
74. Olson, G. B., & Cohen, M. (1979). Interphase-boundary dislocations and the concept of coherency. *Acta Metallurgica*, *27*(12), 1907–1918. https://doi.org/10.1016/0001-6160(79)90081-6
75. Overwijk, M. H. F., Heuvel, F. C. Van Den, & Lieuwma, C. W. T. B. (2001). Novel scheme for the preparation of transmission electron microscopy specimens with a focused ion beam Novel scheme for the preparation of transmission electron microscopy specimens with a focused ion beam, *2021*(1993). https://doi.org/10.1116/1.586537
76. Pantelides, S. T. (1975). Electronic excitation energies and the soft-x-ray absorption spectra of alkali halides. *Physical Review B*, *11*(6), 2391–2411. https://doi.org/10.1103/PhysRevB.11.2391
77. Pearson, D. H., Fultz, B., & Ahn, C. C. (1988). Measurements of 3d state occupancy in transition metals using electron energy loss spectrometry. *Applied Physics Letters*, *53*(15), 1405–1407. https://doi.org/10.1063/1.100457
78. Pedio, M., Fuggle, J. C., Somers, J., Umbach, E., Haase, J., Lindner, T., … Robinson, A. (1989). Covalency in oxygen chemisorption as probed by x-ray absorption. *Physical Review B*, *40*(11), 7924–7927. https://doi.org/10.1103/PhysRevB.40.7924
79. Pennycook, S. J., & Nellist, P. (2011). *Scanning Transmission Electron Microscopy Image and Analysis*. (S. J. Pennycook & P. D. Nellist, Eds.). New

York: Spriger. https://doi.org/10.15713/ins.mmj.3
80. Pennycook, S. J., Zhou, H., Chisholm, M. F., Borisevich, A. Y., Varela, M., Gazquez, J., … Narayan, J. (2013). Misfit accommodation in oxide thin film heterostructures. *Acta Materialia*, *61*(8), 2725–2733. https://doi.org/10.1016/j.actamat.2012.09.069
81. Popova, E., Deb, M., Bocher, L., Gloter, A., Stéphan, O., Warot-Fonrose, B., … Keller, N. (2017). Interplay between epitaxial strain and low dimensionality effects in a ferrimagnetic oxide. *2017 IEEE International Magnetics Conference, INTERMAG 2017*. https://doi.org/10.1109/INTMAG.2017.8007822
82. Radtke, G., & Botton, G. A. (2011). Energy Loss Near-Edge Structures. In S. J. Pennycook & P. D. Nellist (Eds.), *Scanning Transmission Electron Microscopy*. New York, USA: Spriger. https://doi.org/10.1007/978-1-4419-7200-2
83. Rečnik, A., Nyir-Kósa, I., Dódony, I., & Pósfai, M. (2013). Growth defects and epitaxy in Fe3O4 and γ-Fe2O3 nanocrystals. *CrystEngComm*, *15*(37), 7539–7547. https://doi.org/10.1039/c3ce40873f
84. Rodríguez Rodríguez, C. I., Farías Mancilla, J. R., Vega Chavez, K. E., Espinosa Magaña, F., Olive Méndez, S. F., & Elizalde Galindo, J. T. (2015). Effect of Thickness on Magnetic Dipolar and Exchange Interactions in SmCo / FeCo / SmCo Thin Films. *Advances in Materials Physics and Chemistry*, *5*(September), 368–373. https://doi.org/10.4236/ampc.2015.59037
85. Sakurai, S., Namai, A., Hashimoto, K., & Ohkoshi, S. (2009). First Observation of Phase Transformation of All Four Fe 2O 3Phases (γ {\textrightarrow} ε {\textrightarrow} β {\textrightarrow} α-Phase). *Journal of the American Chemical Society*, *131*(51), 18299–18303. https://doi.org/10.1021/ja9046069
86. Sakurai, S., Shimoyama, J. ichi, Hashimoto, K., & Ohkoshi, S. ichi. (2008). Large coercive field in magnetic-field oriented ε-Fe2O3 nanorods. *Chemical Physics Letters*, *458*(4–6), 333–336. https://doi.org/10.1016/j.cplett.2008.04.121
87. Sandiumenge, F., Santiso, J., Balcells, L., Konstantinovic, Z., Roqueta, J., Pomar, A., … Martínez, B. (2013). Competing misfit relaxation mechanisms in epitaxial correlated oxides. *Physical Review Letters*, *110*(10), 1–5. https://doi.org/10.1103/PhysRevLett.110.107206
88. Schlom, D. G., Chen, L. Q., Fennie, C. J., Gopalan, V., Muller, D. A., Pan, X., … Uecker, R. (2014). Elastic strain engineering of ferroic oxides. *MRS Bulletin*, *39*(2), 118–130. https://doi.org/10.1557/mrs.2014.1
89. Schmid, H., Gilardi, E., Gregori, G., Longo, P., Maier, J., & van Aken, P. A. (2018). Structure and chemistry of interfaces between ceria and yttria-stabilized zirconia studied by analytical STEM. *Ultramicroscopy*, *188*, 90–100. https://doi.org/10.1016/j.ultramic.2018.01.014
90. Singh, R. K., & Narayan, J. (1990). Pulsed-laser evaporation technique for deposition of thin films: Physics and theoretical model. *Physical Review B*, *41*(13), 8843–8859. https://doi.org/10.1103/PhysRevB.41.8843
91. Song, K., Schmid, H., Srot, V., Gilardi, E., Gregori, G., Du, K., … Van Aken, P. A. (2014). Cerium reduction at the interface between ceria and yttria-stabilised zirconia and implications for interfacial oxygen non-stoichiometry. *Microscopy*

and Microanalysis, *20*(3), 420–421. https://doi.org/10.1017/S1431927614003821
92. Stadelmann, P. A. (1987). EMS - a software package for electron diffraction analysis and HREM image simulation in materials science. *Ultramicroscopy*, *21*(2), 131–145. https://doi.org/10.1016/0304-3991(87)90080-5
93. Tafto, J.; Krivanek, O. L. (1982). Site-Specific Valence Determination by Electron Energy-Loss Spectroscopy. *Physical Review Letters*, *48*(8), 560–563.
94. Tan, H., Verbeeck, J., Abakumov, A., & Van Tendeloo, G. (2012). Oxidation state and chemical shift investigation in transition metal oxides by EELS. *Ultramicroscopy*, *116*, 24–33. https://doi.org/10.1016/j.ultramic.2012.03.002
95. Teja, A. S., & Koh, P. Y. (2009). Synthesis, properties, and applications of magnetic iron oxide nanoparticles. *Progress in Crystal Growth and Characterization of Materials*, *55*(1–2), 22–45. https://doi.org/10.1016/j.pcrysgrow.2008.08.003
96. Thai, T. M. N., Nguyen, D. T., Lee, N.-S., Rhyee, J.-S., Song, J., & Kim, H.-J. (2016). Stabilization of metastable ε-Fe $_2$ O $_3$ thin films using a GaFeO $_3$ buffer. *Journal of Applied Physics*, *120*(18), 185304. https://doi.org/10.1063/1.4967393
97. Thole, B. T., van der Laan, G., & Butler, P. H. (1988). Spin-mixed ground state of Fe Phthalocyanine and the temperature-dependet branching ratio in X-Ray absorption spectroscopy. *Chemical Physics Letters*, *149*(3), 295–299.
98. Tronc, E., Chanéac, C., & Jolivet, J. P. (1998). Structural and Magnetic Characterization ofε-Fe2O3. *Journal of Solid State Chemistry*, *139*(1), 93–104. https://doi.org/10.1006/jssc.1998.7817
99. Tseng, Y. C., Souza-Neto, N. M., Haskel, D., Gich, M., Frontera, C., Roig, A., … Nogués, J. (2009). Nonzero orbital moment in high coercivity ε-Fe2O 3 and low-temperature collapse of the magnetocrystalline anisotropy. *Physical Review B - Condensed Matter and Materials Physics*, *79*(9), 1–6. https://doi.org/10.1103/PhysRevB.79.094404
100. Tuček, J., Zbořil, R., Namai, A., & Ohkoshi, S. I. (2010). ε-Fe2O3: An advanced nanomaterial exhibiting giant coercive field, millimeter-wave ferromagnetic resonance, and magnetoelectric coupling. *Chemistry of Materials*, *22*(24), 6483–6505. https://doi.org/10.1021/cm101967h
101. Turner, S., Lazar, S., Freitag, B., Egoavil, R., Verbeeck, J., Put, S., … Van Tendeloo, G. (2011). High resolution mapping of surface reduction in ceria nanoparticles. *Nanoscale*, *3*(8), 3385–3390. https://doi.org/10.1039/c1nr10510h
102. Van Aken, P. A., & Liebscher, B. (2002). Quantification of ferrous/ferric ratios in minerals: New evaluation schemes of Fe L23 electron energy-loss near-edge spectra. *Physics and Chemistry of Minerals*, *29*(3), 188–200. https://doi.org/10.1007/s00269-001-0222-6
103. van Aken, P. a., Liebscher, B., & Styrsa, V. J. (1998). Quantitative determination of iron oxidation states in minerals using Fe L 2,3 -edge electron energy-loss near-edge structure spectroscopy. *Physics and Chemistry of Minerals*, *25*(5), 323–327. https://doi.org/10.1007/s002690050122
104. van der Laan, G., & Thole, B. T. (1991). Strong magnetic x-ray dichroism in 2 p absorption spectra of 3 d transition-metal ions. *Physical Review B*, *43*(16),

13401–13411. https://doi.org/10.1103/PhysRevB.43.13401
105. Van Der Merwe, J. H. (1950). On the stresses and energies associated with inter-crystalline boundaries. *Proceedings of the Physical Society. Section A*, *63*(6), 616–637. https://doi.org/10.1088/0370-1298/63/6/310
106. Verbeeck, J., & Van Aert, S. (2004). Model based quantification of EELS spectra. *Ultramicroscopy*, *101*(2–4), 207–224. https://doi.org/10.1016/j.ultramic.2004.06.004
107. Wang, F., Egerton, R. F., & Malac, M. (2006). Interpretation of the postpeak in iron fluorides and oxides. *Ultramicroscopy*, *106*(10), 925–932. https://doi.org/10.1016/j.ultramic.2006.04.005
108. Williams, D. B., & Carter, C. B. (2009). *Transmission Electron Microscopy*. *Transmission Electron Microscopy*. https://doi.org/10.1007/978-0-387-76501-3_1
109. Yamada, H., Ogawa, Y., Ishii, Y., Sato, H., Kawasaki, M., Akoh, H., & Tokura, Y. (2004). Engineered interface of magnetic oxides. *Science*, *305*(5684), 646–648. https://doi.org/10.1126/science.1098867
110. Yang, K., Kim, J. W., Kogure, T., Dong, H., Baik, H., Hoppie, B., & Harris, R. (2016). Smectite, illite, and early diagenesis in South Pacific Gyre subseafloor sediment. *Applied Clay Science*, *134*, 34–43. https://doi.org/10.1016/j.clay.2016.03.041
111. Yao, G., Gao, M., Ji, Y., Liang, W., Gao, L., Zheng, S., … Lin, Y. (2016). Surface step terrace tuned microstructures and dielectric properties of highly epitaxial CaCu3Ti4Oi12thin films on vicinal LaAlO3substrates. *Scientific Reports*, *6*(December 2015), 1–11. https://doi.org/10.1038/srep34683
112. Zeches, R. J., Rossell, M. D., Zhang, J. X., Hatt, A. J., He, Q., Yang, C.-H., … Ramesh, R. (2009). A strain-driven morphotropic phase boundary in $BiFeO_3$. *Science*, *326*(5955), 977–980. https://doi.org/10.1126/science.1177046
113. Zhu, Y., Chen, A., Zhou, H., Zhang, W., Narayan, J., Macmanus-Driscoll, J. L., … Wang, H. (2013). Research updates: Epitaxial strain relaxation and associated interfacial reconstructions: The driving force for creating new structures with integrated functionality. *APL Materials*, *1*(5). https://doi.org/10.1063/1.4828936
114. Zuo, J. M., Gao, M., Tao, J., Li, B. Q., Twesten, R., & Petrov, I. (2004). Coherent nano-area electron diffraction. *Microscopy Research and Technique*, *64*(5–6), 347–355. https://doi.org/10.1002/jemt.20096
115. Zuo, J. M., & Spence, J. C. H. (2015). *Advanced Transmission Electron Microscopy*. https://doi.org/10.1007/978-3-319-15177-9
116. Zur, A., & Mcgill, T. C. (1984). Lattice match : An application to heteroepitaxy Lattice match : An application to heteroepitaxy, *378*(1984). https://doi.org/10.1063/1.333084